An integrated structural and geochemical study of auriferous sheeted quartz veins within the 2740 Ma Côté Gold deposit, Swayze Greenstone Belt, Ontario

by

Joycelyn Smith

A thesis submitted in the partial fulfillment

of the requirements for the degree of

Master of Science (MSc) in Geology

The Faculty of Graduate Studies

Laurentian University

Sudbury, Ontario, Canada

THESIS DEFENCE COMMITTEE/COMITÉ DE SOUTENANCE DE THÈSE
Laurentian Université/Université Laurentienne
Faculty of Graduate Studies/Faculté des études supérieures

Title of Thesis Titre de la thèse	An integrated structural and geochemical study of auriferous sheeted quartz veins within the 2740 Ma Côté Gold deposit, Swayze Greenstone Belt, Ontario
Name of Candidate Nom du candidat	Smith, Joycelyn
Degree Diplôme	Master of Science
Department/Program Département/Programme	Geology
Date of Defence Date de la soutenance	August 04, 2016

APPROVED/APPROUVÉ

Thesis Examiners/Examinateurs de thèse:

Dr. Bruno Lafrance
(Co-Supervisor/Co-Directeur(trice) de thèse)

Dr. Daniel Kontak
(Co-Supervisor/Co-directeur(trice) de thèse)

Dr. Györgyi Tuba
(Committee member/Membre du comité)

Dr. Murray Allan
(External Examiner/Examinateur externe)

Approved for the Faculty of Graduate Studies
Approuvé pour la Faculté des études supérieures
Dr. Shelley Watson
Madame Shelley Watson
Acting Dean, Faculty of Graduate Studies
Doyenne intérimaire, Faculté des études supérieures

ACCESSIBILITY CLAUSE AND PERMISSION TO USE

Abstract

The Archean Côté Gold deposit (8.3 M oz) is a low-grade, high-tonnage Au(-Cu) deposit located within the 2741 Ma Chester Intrusive Complex (CIC) on the southeast limb of the Swayze Greenstone Belt (SGB) in the Abitibi Subprovince of northern Ontario. Steeply-dipping, auriferous sheeted veins that form part of the mineralized setting can be interpreted as either orogenic in origin and associated with the formation of the proximal Ridout deformation zone or as older and intrusion-related. Structures that overprint CIC are similar to those of the RDZ and are interpreted to post-date the intrusion and mineralized veins. A geochemical study of an alteration profile related to a mineralized vein reveals elemental enrichment in K, Rb, Li, Cs, Ba, Na, F, S and LREEs with a Au-Cu-Te-Pb-Bi-S association. In situ SIMS analysis of $\delta^{34}S$ and $\delta^{18}O$ are consistent with a magmatic signature for the fluid with a minor component of seawater, and supports the previously proposed high-level, subaqueous setting for the deposit. The combination of temporal, spatial, and geochemical characteristics of the sheeted veins suggests an intrusion-related origin.

Keywords

Structural geology, intrusion-related gold deposit, alteration, sheeted veins

Acknowledgements

I owe my gratitude to the great many people involved in completing this study. Foremost I would like to thank my supervisors Dr. B. Lafrance and Dr. D.J. Kontak for their insights, guidance and continued support throughout this thesis. It is with their help in the field, lab and office that I have become a stronger scientist and better writer. I am truly fortunate to have had them as my mentors.

I would also like to thank M. Fayek for his contributions in the SIMS component of this study, Willard Desjardins for making all of my thin sections, and William Zhe for his assistance with the operation of SEM-EDS.

I thank IAMGOLD Corporation for their considerable contributions in funding and support that made this project possible. I also thank the staff of the IAMGOLD Côté Gold project for their aid and input. I thank Brandon Choquette for his assistance mapping and Andrew Shea for his help over the past several years. I would like to acknowledge and sincerely express my appreciation to Brian Tomczuk for his patience and assistance on site and Dr. Laura Katz for her intellectual guidance and for having suggested this project to me.

Lastly I would like to thank my family for their constant encouragement, understanding and council throughout the entirety of this process.

Table of Contents

List of Figures

List of Tables

List of Appendices

Appendix A

Preface

The thesis is on the origin of gold-bearing quartz veins at the Côté Gold deposit near Gogama in northern Ontario. The deposit is owned by IAMGOLD Corporation, who provided all the funding and logistical support for the project.

The thesis is written as a paper to be submitted to the journal of Economic Geology. I am the lead author with my supervisors, B. Lafrance and D.J. Kontak, and M. Fayek (University of Manitoba), as co-authors who read over several drafts of this work and made edits and intellectual contributions to the final product. Over the tenure of the project, results were presented at annual meetings with the company and more formally as poster and oral presentations at national geological conferences and symposiums, but these are not considered here as part of the final thesis product.

I did the field mapping, sampling and data collection as well as the construction of all the diagrams and maps in the thesis. I also characterized the veins and mineral chemistry of alteration minerals using the scanning electron microscope (SEM) housed in the Central Analytical Facility of Laurentian University. Mapping and interpretation of outcrops 53 and Skidder (in Appendices) were done in collaboration with Laura Katz who completed her Ph.D. thesis at Laurentian University which focused on the mineralization and alteration geochemistry of the Côté Gold deposit (Katz, 2016). The detailed analytical parts of the study, such as the lithogeochemical, Rietveld refinements and isotopic (O, S) data presented, were completed in co-operation with Activation Laboratories in Ancaster, Ontario, the Mineral Exploration Research Center (MERC) at Laurentian University, and the Secondary Ion Mass Spectrometry Laboratory

at the University of Manitoba. Although my supervisors provided advice and guidance, I am responsible for all the conclusions and interpretations presented in the thesis.

An integrated structural and geochemical study of auriferous quartz veins within the 2740 Ma Côté Gold deposit, Swayze Greenstone Belt, Ontario: Evidence for an intrusion-related origin

*Joycelyn C. Smith, *Bruno Lafrance, *Daniel J. Kontak

and **Mostafa Fayek

*Mineral Exploration Research Centre, Department of Earth Sciences, Laurentian University, Sudbury, Ontario P3E 2C6

**Department of Geological Sciences, University of Manitoba,

Winnipeg, Manitoba R3T 2N2

Abstract

The ca. 2740 Ma Côté Gold deposit (8.3 M oz Au) is a low-grade high-tonnage Au(-Cu) porphyry-type deposit located on the southeastern limb of the Archean Swayze Greenstone Belt (SGB) in the Abitibi Subprovince, Canada. The deposit is hosted by a magmatic-hydrothermal breccia body which is contemporaneous with tonalite and diorite of the 2740 ± 1 Ma Chester Intrusive Complex (CIC). Mineralization occurs within or peripheral to the breccia as disseminations, fracture fills and stockwork, and in association with steeply dipping east-west striking auriferous veins. The latter veins are present as quartz-sulphide lined fractures with a moderate to strong, typically 1-30 cm wide sericite alteration halo. Given that such auriferous sheeted veins could be interpreted either as orogenic, that is associated with the formation of the regional Ridout deformation zone (RDZ) in the area, or as older veins related to the CIC, thus intrusion-related, an integrated structural-lithogeochemical study was undertaken.

As part of the structural aspect, the style and kinematic significance of structures overprinting the CIC were compared to those of the RDZ based on four mapping transects through the RDZ. The observations indicate three dominant deformation events affected the CIC with a less significant early event (S_1). The first (regionally D_2) produced sinistral, north-side up, E-W trending shear

zones with a strong S_2 foliation. This is overprinted by the D_3 event, where S_2 was crenulated during reversal of slip along the shear zones, producing an S_3 crenulation cleavage. Subsequently, a D_4 dextral reactivation event produced a S_4 foliation oriented anticlockwise to the shear zone margins. These structures overprint the Côté Gold auriferous quartz veins and suggest, therefore, that the veins predate regional deformation. This conclusion is supported by cross-cutting relationships and Re-Os dating of molybdenite (i.e., ca. 2740 Ma) from one of these veins which indicates the veins formed shortly after the emplacement of the CIC, at least 50 Ma before subsequent deformation.

A sequential detailed study of the alteration profile marginal to a single auriferous vein reveals a signature of K (Rb, Li, Cs, Ba), Na, F, S and LREEs, which is similar to the alteration signature of the main deposit. Laser ablation inductively coupled plasma-mass spectrometry (LA ICP-MS) analysis of pyrites from the vein indicate a complex Au-Ag-Cu-Cd-In-Sn-Te-Bi-Pb-Sb- metal association, common of intrusion-related deposits, but also similar to some orogenic systems. Analysis of the $\delta^{34}S$ and $\delta^{18}O$ values of pyrite and quartz, respectively, in the vein and alteration halo indicate a strong magmatic influence but that mixing with another fluid of inferred seawater origin occurred. The latter is therefore consistent with the current deposit model of a subvolcanic, subaqueous setting.

The combination of temporal, spatial, and geochemical characteristics of the sheeted veins suggests they relate to an intrusion-related system and part of the mineralizing intrusive phases of the low-grade high-tonnage Côté gold porphyry-style deposit.

1. Introduction

Auriferous quartz veins are spatially associated with intrusions in some deposit settings. The latter act as competent physical host that accommodates hydrothermal fluid flow, the origin of which plays an important role in determining the type of deposit (e.g., Sillitoe and Thompson, 1998; Lang and Baker, 2001; Goldfarb et al. 2005; Hart et al. 2007). If the fluids are products of regional deformation and metamorphism, orogenic gold deposits may form along faults and shear zones intersecting or enclosing the intrusions; in such cases the intrusions are just passive participants. In contrast, if the fluids originate from the crystallization of a progenitor intrusion, then structurally similar vein type or disseminated gold deposits can form, but in this case they

are termed intrusion-related gold deposits (IRGD) and porphyry gold systems to reflect the source of the fluid. For the purpose of this study, these two systems are collectively termed igneous-related gold systems (IRGS) after Sillitoe and Thompson (1998), and associated veins are termed igneous-related veins. Orogenic- and igneous-related veins may share similar textures and mineralogy and, thus, it may be difficult to differentiate these two deposit types in the field (Groves et al., 2003). Both can occur as parallel sheeted vein systems, the orientation of which are controlled by tectonic regional stresses for orogenic veins and by combined magmatic-related and tectonic regional stresses for igneous-related veins (Thompson et al., 1999; Goldfarb et al., 2005; Gloaguen et al., 2014), and thus creates problems in regards to classifying the nature of the mineralization.

The similarity between the two vein systems is such that some gold systems initially interpreted as orogenic vein systems have been more recently reinterpreted as igneous-related vein systems. These include, but are not limited to, previously reported orogenic gold systems in the Lachlan fold belt in Victoria, Australia (Miller and Wilson, 2004), the Archean Wallaby deposit of the Yilgarn Craton, Australia (Walsh et al., 2003) and Phanerozoic Linglong deposit of Jiaodong, China (Wang et al., 1998; Goldfarb et al., 2005). In the Archean Abitibi greenstone belt (Canada), the Kirkland Lake and Malartic deposits are examples of two deposits which have been alternatively classified as orogenic- and igneous-related deposits. The Kirkland Lake deposit, located 2 km north of the Larder Lake-Cadillac deformation zone (LLCDZ; Fig. 1**)** consists of parallel quartz-carbonate veins along sericitic brittle-ductile faults cross cutting syenite intrusions (Thompson et al., 1950; Ispolatov et al., 2008). It had been classified as an orogenic gold deposit by Robert and Poulsen (1997) and Robert (2001), who noted its similarities in metal association (Au-Te-Mo), mineralogy and sulphur isotopes to syenite-hosted

deposits, but was subsequently reclassified as an intrusion-related deposit (Robert, 2003). The Canadian Malartic deposit is a low-grade, large tonnage, 18.5 M oz gold deposit hosted by felsic to intermediate porphyritic intrusives (De Souza et al., 2015). It is located 150 km east of Kirkland Lake immediately south of the LLCDZ. Helt et al. (2014) recently classified the deposit as an Archean oxidized porphyry deposit based on isotopic evidence of a magmatic fluid source, but one year later, De Souza et al. (2015) attributed the formation of the main gold-bearing veins to an orogenic event associated with the LLCDZ.

Distinguishing orogenic veins from igneous-related veins is therefore challenging but important for guiding exploration efforts. For targeting purposes, exploration for igneous-related veins should center on the host intrusions and their surrounding rocks, whereas exploration for orogenic veins should focus on the fault zones hosting the veins. Thus, useful criteria for differentiating orogenic veins from igneous-related veins are needed. Such criteria are discussed in this paper using the 2740 Ma intrusion-related Côté Gold deposit in the Swayze greenstone belt (SGB), Ontario, as an example. Below are integrated the results of two complementary studies, one, a structural analysis of mineralized veins which are compared to the regional deformation history in the area, and the second, a fluid chemical study of an alteration profile of one mineralized vein setting. The systematic approach employed here is shown to be effective in classifying the vein system and provides a template that can be applied to other gold deposit settings.

2. Regional Geology

The Archean SGB represents the southwestern extension of the metal-rich Abitibi Greenstone Belt (AGB) in the southern Superior Province. The Côté Gold deposit (8.3 M oz) is a recently discovered (Rogers et al., 2013) low-grade, high-tonnage Au(-Cu) deposit hosted by the ca. 2740 Ma, dioritic to tonalitic, Chester Intrusive Complex (CIC; Kontak et al., 2013; IAMGOLD, 2014; Katz, 2016). The CIC is bounded to the south by the ca. 2715 Ma to ca. 2636 Ma Ramsey-Algoma granitoid complex (van Breeman et al., 2006), and to the north by mafic to felsic metavolcanic rocks of the Chester Group (2734 ± 2 Ma and 2739 ± 2 Ma; Ayer et al. 2002), which is interleaved with younger metasedimentary rocks of the Ridout Group (2695 ± 2 Ma; van Breeman et al., 2006). These supracrustal rocks are in contact to the north with the younger Neville pluton (2682 ± 3 Ma; Heather, 1993), which constitutes the southern margin of the much larger, ca. 2682 Ma to ca. 2722 Ma, Kenogamissi Batholith (van Breeman et al., 2006).

All supracrustal rocks of the Chester and Ridout groups record greenschist and amphibolite facies metamorphism (Fig. 2). The Chester Group is equivalent to the Pacaud assemblage of Ayer et al. (2002) and is divided into two formations: the mafic Arbutus Formation and the younger, felsic to intermediate, Yeo Formation. The Arbutus Formation consists of variolitic and amygdaloidal, aphyric to pyroxene- and feldspar-phyric, tholeiitic pillow basalt, pillow breccia, and massive flow or sill. The Yeo Formation consists of massive felsic flows and domes, and bedded to massive ash tuff to tuff breccia with pumice and scoria clasts, interleaved with epiclastic interflow horizons, iron formation and chert (van Breeman et al., 2006). The 2731 Ma +7/-5 Ma, calc-alkaline, Yeo Formation is similar in age and geochemistry to the felsic intrusive rocks of the CIC (Heather et al., 1996; van Breeman et al., 2006;Berger, 2012), which is

interpreted as a synvolcanic sill or laccolith (Katz et al.,2015) underlying the metavolcanic rocks of the Chester Group. The Ridout Group consists of Timiskaming-like clastic sedimentary rocks in unconformable contact with the underlying metavolcanic rocks of the Chester Group (Heather, 1993). It comprises fluvial polymictic conglomerate sandstones interbedded with siltstone and argillite.

The Côté Gold deposit (herein as described by Katz, 2016) is hosted by a magmatic-hydrothermal breccia associated with the dioritic phase of the CIC. The magmatic breccia consists of a diorite magma which has brecciated tonalite and dioritic rocks and occurs predominantly in the central and southern parts of the deposit, whereas the hydrothermal breccia consists of a biotite ± sulphide ± magnetite ± carbonate -rich matrix and occurs mainly in the central and northern parts of the deposit. Although mineralization occurs in all major rock types, it is co-spatial with hydrothermal alteration. The hydrothermal breccia is the most consistently mineralized unit in the deposit with an average Au grade of 0.67 g/t.

Gold mineralization occurs as disseminations and fracture-fill stockworks within the breccias and surrounding tonalite and diorite phases and as quartz ± sulfide ± muscovite ± carbonate ± tourmaline veins cutting across both tonalite and diorite phases of the CIC. These veins are present up to 1200 m west and 3 km northeast of the deposit within the CIC.

The Chester vein system is located approximately 4 km east of the Cote deposit and consisted of narrow quartz-sulfide veins hosted within diorite. The mine was developed in 1986 and 1989 but only began commercial production in 2010 and 2011 with Trelawney Mining and Exploration. The mine recovered a total of 33,000 grams Au, however operations ceased in 2011 because the

veins were reported as being too discontinuous to be mined successfully (IAMGOLD unpubl. report).

2.1 Ridout Deformation Zone

The Ridout deformation zone (RDZ) is an east-trending, 500 m to 2 km wide, high-strain zone characterized by a strong, steeply north-dipping, contact-parallel foliation, along which lies a north-northeast-plunging (50°-80°) mineral stretching lineation. It extends from the Kapuskasing structural zone to the west, across the southern part of the SGB where it overprints rocks of the Chester Group, Ridout Group and Neville pluton, to the Shining Tree area to the east where it disappears under cover rocks of the Paleoproterozoic Huronian Supergroup. Zones of moderate to strong sericite, Fe-carbonate, silica and chlorite alteration are locally present along the RDZ (Heather, 2001).

The RDZ is interpreted as a zone of strong pure shear flattening overprinted by early sinistral and late dextral transcurrent shearing (Heather, 2001; Berger, 2011). Although it has also been interpreted as the westward extension of the LLCDZ (Heather, 2001; Bleeker and van Breemen, 2010; Beakhouse, 2011; Ayer et al., 2013), differences in its strain history (early flattening along the RDZ versus early thrusting along the LLCDZ), in its relative location with respect to Timiskaming-like sedimentary rocks (north for the RDZ versus south for the LLCDZ), and in its location 60 km south of the projected westward extension of the LLCDZ (Fig. 1; Berger, 2011; Atkinson, 2013), suggest that the LLCFZ may instead correlate with a high strain zone along the northern limb of the Brett Lake synform, north of the RDZ (Ayer et al., 2013; Atkinson, 2013).

3. Structural Geology

The Côté Gold deposit contains multiple sets of gold-bearing sheeted veins. The main vein sets are oriented roughly east-west within 30° of the contact between the Chester Intrusive Complex and overlying metavolcanic rocks. As the veins are generally deformed and close in orientation to the contact-parallel RDZ, they either formed as orogenic veins associated with the RDZ, or as igneous-related veins predating the RDZ. To test these two interpretations, structures along the RDZ were mapped and then compared to those associated with the sheeted veins in the CIC. Table 1 summarizes the deformation events and structures present within the RDZ and CIC.

3.1 Ridout Deformation Zone

From north to south, four transects were mapped across the RDZ along the Chester, Highway 144, London Derry and Nebaskwasi roads (Fig. 2). The transects begin in the Neville pluton to the north, continue across metavolcanic rocks of the Chester Group and conglomerate of the Ridout Group, and terminate in the CIC and Ramsey Algoma intrusive complex to the south.

The metavolcanic rocks along the London Derry Road are overprinted by a tight regional syncline (Fig. 3). The fold has an axial planar foliation defined by the flattening of clasts and a strong, coaxial, steeply-plunging (78° → 342°), stretching lineation defined by the elongation of the same clasts. The foliation strikes 270°-280° and dips 80° N to vertical, parallel to lithological contacts along the limbs of the fold. Although the fold does not overprint a foliation, an older cleavage (S_1) is present elsewhere in the belt (Heather, 2001), so the regional fold and associated foliation and lineation are termed F_2, S_2, and L_2, respectively. Younging indicators present in these rocks are visible outside of the RDZ and include the truncation of cross bedding within a

felsic to intermediate tuff of the Yeo Formation (Fig. 4a). The reversal in younging direction and the symmetrical repetition of units occurs on either limb of the fold.

The S_2 foliation and steeply-plunging L_2 stretching lineation becomes more pronounced within the RDZ. The latter has been mapped as a 500 m to 1 km wide high strain zone which straddles the contact between the ca. 2680 Ma Neville pluton and metavolcanic rocks of the Yeo and Arbutus formations along the Chester road and Highway 144. To the east, along the London Derry and Nebaskwasi roads, the high strain zone is completely enclosed within the latter metavolcanic rocks and conglomerate of the Ridout Group. The RDZ is characterized by high strain domains dominated by a strong, contact-parallel foliation, masking primary textures and structures in the rocks, alternating with lower strain domains with a weak S_2 foliation. Asymmetrical strain shadows around feldspar porphyroclasts **(**Fig. 4b**)** and S-shaped drag folds manifested by folded dikes and lithological contacts suggest north-side-up sinistral slip along the RDZ (Smith et al., 2014).

The S_2 foliation is overprinted by S-shaped F_3 folds with an axial planar, differentiated, S_3 crenulation cleavage. The folds typically strike 290°, dip 85°N to vertical, and plunge 40°-50° to the east (Fig. 4c). A steeply-plunging mineral lineation (L_3) defined by biotite, chlorite and amphibole is present along S_3. Along the Chester road, the S_3 foliation locally becomes the dominant fabric within the RDZ due to transposition of S_2 parallel to S_3, resulting in a composite S_2/S_3 foliation (Fig. 4d, e, f).

The S_2 and S_3 foliations are overprinted by Z-shaped F_4 folds plunging 80° to the east. The folds have an axial planar S_4 crenulation cleavage, striking roughly 240°-250° and dipping 80°NW to vertical (Figs. 4g, 5a). These Z-shaped F_4 folds are spatially associated with dextral shear bands

and back-rotated quartz boudins, suggesting that the RDZ was reactivated as dextral transcurrent shear zone during a D_4 event.

A late, shallowly-plunging, crinkle lineation is locally observed along well-developed S_2 and S_3 foliation planes (Fig. 5b). Although the relationship between this lineation and D_4 structures is not observed, it is likely younger than the latter, as observed elsewhere in the Superior craton in the Beardmore-Geraldton Belt (Devaney and Williams, 1989; Lafrance et al., 2004) and along the Cadillac-Larder Lake deformation zone (Lafrance, 2015).

3.2 Chester Intrusive Complex

Four stripped outcrops of the CIC showing overprinting relationships between the veins, shear zones and foliations were selected for detailed structural mapping (Fig. 6). Lithological base maps of the North Breccia and Chipmunk outcrops were provided by Katz (2016). Georeferenced meter-scale grids were laid down on the South Breccia and Candy Cane outcrops and used for the detailed mapping of these outcrops.

The South Breccia outcrop (Fig. 7a) consists of tonalite with dioritic enclaves, intruded by a magmatic breccia with a dioritic matrix. These rocks were deformed within a 1 to 5 meter wide shear zone, striking 258° and dipping 76°N, which is overprinted by a late diabase dike. Quartz-carbonate ± sulfides ± tourmaline veins, varying in thickness from a few mm to <30 cm, are straight and undeformed outside of the shear zone but are strongly folded within it, suggesting a pre-shearing emplacement of the veins (Fig. 7c). The shear zone has a strong sericitic and chloritic foliation, striking 280° and varying in dip from 80°N to 85°S. The foliation is oriented clockwise to the shear zone margin on horizontal section and 5-10° anticlockwise to the shear

zone margin on west-facing vertical section, suggesting north-side-up sinistral movement parallel to the shear zone margin. The foliation is crenulated and a crenulation cleavage, striking 307° and dipping 49°NE, formed parallel to the axial plane of the crenulations. The crenulation cleavage is oriented clockwise to the shear zone margin and it dips more shallowly to the north than the shear zone. It formed during microfolding of the early foliation, which was in the shortening field of the deformation strain ellipse during south-side-up slip reversal along the shear zone (Fig.7b, d).

The North Breccia outcrop (Fig. 8) is located approximately 250 m north of the South Breccia outcrop. It consists of tonalite and diorite intruded by hornblende-bearing pegmatite (i.e., evolved phase of the diorite) and hydrothermal breccia, and cut by lamprophyre and mafic dikes. A foliation, striking 265° and dipping 75°-80°N, is present throughout the outcrop and is more pronounced within a steep shear zone at the south end of the outcrop (Fig. 9a). The shear zone strikes 250°-260° and dips 80°N to vertical parallel to boudinaged quartz-sulfide (± molybdenite ± visible gold) veins occupying the centre of the shear zone (Fig. 9b**)**. The foliation is deflected in anticlockwise manner on both horizontal and west-facing vertical sections as it passes from the margin to the centre of the shear zone. Thus, the foliation is oriented clockwise to the veins and shear zone on horizontal section and it dips more shallowly to the north than the veins and shear zone on vertical section. Its orientation and deflection together with the presence of sinistral shear bands on horizontal section suggest north-side-down sinistral movement along the shear zone.

Although the veins are spatially associated with the shear zones, they could have formed either before or during the shearing event. The chronology of the shear zone and veins is revealed by

overprinting relationships. North of the shear zone, a lamprophyre dike cuts across auriferous quartz-sulphide veins that are identical and parallel to those in the shear zone **(**Fig. 9c, d). The dike is itself offset along the shear zone (Fig. 9e), thus it was emplaced after the formation of the veins but before shearing. Because the veins predate the dike, then they must also have formed before the shear zone. These relationships suggest that the shearing is superimposed on the veins and that the weak sericitic alteration halo surrounding the veins localized the formation and propagation of the shear zone. Another interesting overprinting relationship is observed north of the shear zone, where an amphibole vein is dextrally offset along a crosscutting, narrow recessive shear zone but underwent anticlockwise (sinistral) rotation or dragging along the margin of the shear zone (Fig. 9f). These contradictory strike-slip shear sense indicators may be explained by apparent horizontal dextral offset of the amphibole vein along a mainly dip-slip sinistral shear zone, or by dextral reactivation of a sinistral shear zone.

The Chipmunk outcrop (Fig. 10) is located 230 m east of the North Breccia outcrop. It consists of tonalite with various size, stoped, angular blocks of diorite. A sub-vertical foliation, striking 100°-110°, is oriented clockwise to the long axis of the diorite blocks. The foliation is cut by an east-striking, subvertical shear zone. The latter has an internal foliation oriented anticlockwise to the shear zone boundary. The presence of this foliation and dextral offset of a dike by 1 m along the shear zone suggest that dextral shearing occurred after the development of the sub-vertical foliation in the diorite blocks (Fig. 10a, b).

The Candy Cane outcrop (Fig. 11) is located outside the ore envelope of the deposit and 1600 m NE of the Chipmunk outcrop. This outcrop, which consists exclusively of tonalite, is transected by numerous, sheeted sulfide ± quartz filled fractures. The main set of fractures typically strikes

300°, dips 50°-55°NE, and has an average spacing of 30 cm to 150 cm. A second set of fractures strikes 325° and dips 40°-45°NE (Figs. 11, 12a). The sheeted fractures are surrounded by 1 to 10 cm wide sericite ± pyrite alteration haloes that are bounded by 1-3 millimeter wide dark green chlorite-rich selvedges which form a sharp boundary with the less altered host tonalite. The haloes have a bleached appearance and are typically rust stained due to the oxidation of the pyrite, which results in the very pronounced visual striping after which the outcrop is named. A foliation, striking 290° and dipping 60°N, is present within the alteration halo of both groups of fractures and is more pronounced in the western part of the outcrop where the rock is more deformed. It undergoes a clockwise change in orientation within the alteration halo of fractures of the main set, suggesting dextral shear. One of these fractures is associated with a conjugate sinistral shear fracture suggesting an overall shortening direction of 005°.However, in most cases, the foliation remains straight and overprints the alteration halo of both sets of fracture (Fig. 12b).

3.3 Assessing Gold Distribution in Quartz Vein Systems

From the four outcrops described above, 66 samples were collected for Au assay to test if they are enriched within the shear zones. Samples were submitted to Accurassay in Timmins, Ontario for analysis using the pulp metallic method in which samples are pulverized to ~90% combined with a 150 mesh sieve. The method has a lower detection limit of 0.001-0.005 g/t.

At the South Breccia outcrop, 12 samples were collected along a section extending across the shear zone and into its undeformed wallrocks. The results, which are displayed in Figure 7, range from 1.35-0.136 g/t with no increase in the gold grade within the shear zone. Furthermore the results are within the range of values for the entire outcrop (n=198, avg. 1.3 g/t Au; IAMGOLD

unpubl. report), which indicates there was no upgrading of gold in the outcrop due to the subsequent deformation event. At the North Breccia outcrop, 4 samples of the quartz ± sulfide veins were collected both inside and outside the shear zone. These results yielded gold values of 0.044 to 4.8 g/t (Fig. 8). The highest gold grade is for a vein having visible gold and molybdenite taken within the shear zone (Fig. 9b). The remaining samples, which come from veins both inside and outside the shear zone, are equally mineralized.

Sampling at the Candy Cane outcrop was done to assess the relationship between gold grade, sheeted veins and deformation. The sample locations are shown in Figure 11 and results are presented in Table 2. Four channels were taken perpendicular to the veining direction that divides the vein + phyllic alteration halo (21) from the less altered tonalite (19). Ten additional samples, which included 5 strongly deformed and 5 relatively undeformed veins with alteration haloes, were collected to compare the relationship between deformation and gold grade. The samples that included the vein and alteration haloes yielded higher grades (0.009-2.11 g/t) than the tonalite host rock (<0.001-0.049 g/t), and the less deformed samples (0.018-0.276 g/t) returned higher grades than the more deformed samples (<0.005-0.063 g/t).

The results from all three outcrops sampled as part of this study indicate that there is no significant correlation between deformation and gold content.

4. Lithogeochemistry

4.1 Geochemistry of Alteration Profile

Detailed mineralogical and geochemical profiles were done across a vein and its alteration halo from the Candy Cane outcrop to characterize changes in the host rocks due to hydrothermal alteration. The alteration halo is 4.5 cm wide and is symmetrically disposed about a hairline fracture in part lined with quartz and pyrite. The alteration halo from only one side of the vein is described. It is subdivided into 6 domains stretching from the most altered domain (A), which is 4.5 cm wide and located adjacent to the vein, to progressively less altered domains (B to F), which are 6 cm wide each (Fig. 13a).

4.1.1 Petrography and SEM-EDS Imaging

Thin sections from domains A to F were examined using an optical microscope and an Oxford S-Sight energy dispersive spectrometer (EDS) detector mounted on the JEOL 6400 scanning electron microscope (SEM) at the Central Analytical Facility of Laurentian University. Mineral chemical analyses were done at a working distance of 15mm, 20 kV accelerating voltage, and 1.005 nA beam current. X-ray maps, displayed as false color images, were collected using an acquisition count time of 20 minutes.

Progressive changes in the mineralogy of the host tonalite in domains A to F are summarized in table format in Figure 14a. Tonalite of the CIC is typically medium-grained and consists of quartz, subhedral plagioclase and accessory muscovite, chlorite, biotite, epidote, oxides, apatite, and zircon. In the least altered domain F to more altered domain B, along with the other alteration samples, there are several aspects of the mineralogy and its chemistry that are noted:

(i) primary igneous plagioclase progressively changes in composition from An_{30} to An_0 and thus becomes more albitic towards the vein; (ii) accompanying formation of albitic plagioclase, fine-grained muscovite and epidote appear within plagioclase (i.e., saussuritization), with higher concentrations more distal from the vein; (iii) in samples closer to the vein, epidote ($\leq$ 250 μm; 7% of sample), which is much coarser-grained than that in the plagioclase, occurs more commonly in the matrix of the tonalite; (iv) chlorite increases in abundance, can be up to 10% of the mode for samples from just outside the intensely sericitized zone; (v) rare-earth element (REE) bearing phases, bastnaesite, allanite and monazite, occur in trace amounts associated with chlorite, epidote and apatite throughout the matrix and next to the vein (Fig. 13d, e); (vi) within the transect chlorite is often associated with sulfides, as well as minor ilmenite, and trace amounts of magnetite and rutile (Fig. 13f); and (vii) epidote close to the vein is commonly cored by allanite (Fig. 13g).

In the most altered domain (A) next to the vein, only relic albitic plagioclase remains and most of the rock consists of quartz and muscovite with minor pyrite, chlorite and coarse-grained epidote. The core of the zoned alteration profile is occupied by fine-grained quartz or a vein-free central fracture. The mineralogy of this zone includes minor to moderate amounts of fine-grained sulfides in the form of pyrite, pyrrhotite and minor chalcopyrite. An Fe-rich chlorite is also commonly found at the center of the veins and fractures with associated titanium-bearing phases. In addition, unusual phases of monazite, bastnaesite and fluorite exist in association with apatite and coarse-grained epidote at the margin of the veins.

The vein itself consists of fine-grained quartz ± calcite, chlorite, pyrite, pyrrhotite, chalcopyrite, ilmenite, rutile and titanite. In other samples, it is expressed as a fracture that is filled with pyrite

± chlorite, pyrrhotite, chalcopyrite, ilmenite, rutile and titanite; note that in parts the vein fill may be partly recrystallized (e.g., quartz). Both quartz-filled veins and quartz-free fractures contain trace amounts of visible gold.

Textural and mineralogical changes from domain F to domain A are best illustrated using X-ray maps (Fig. 14**).** In domain E (Fig. 14d), the primary texture of the host tonalite remains, although partial resorption of quartz is observed. Larger quartz grains lack muscovite inclusions in addition to neomorphic quartz intergrown with hydrothermal muscovite. Plagioclase is partially replaced by metamorphic epidote and muscovite. In domains closer to the vein **(**Fig. 14c), there is a decrease in both metamorphic muscovite and epidote and an increase in albite, which become replaced by muscovite in domain A (Fig. 14b) adjacent to the vein. There is also a notable increase in quartz and change in its texture in domain A.

4.1.2 Rietveld Modal Mineralogy

The modal mineralogy of domains A to F was determined by means of the Rietveld method, which uses X-ray diffraction. The data was acquired and processed in the Central Analytical Facilities at Laurentian University following the procedure described by Lafrance et al. (2008). Results of the analysis are presented in Figure 15**.**

The mineralogy of the alteration profile shows a uniform mineral assemblage for the least altered samples, which are dominated by quartz (32%) and plagioclase (50%). In the latter case, there is also a mixture of sodic and calcic plagioclase. The former was produced during saussuritization but also as part of the alteration halo, as discussed in more detail below, whereas the latter is remnant primary plagioclase. Muscovite increases in abundance (from 4% to 7%) at the expense

of plagioclase from least altered domain F to more altered domain B, whereas other minerals, such as chlorite (~7%), epidote (~5%) and iron carbonate (~1%) remain roughly constant in abundance. The anorthite end member slightly increases in abundance (up to 7%) and then completely disappears in domain B. A major change occurs in domain A as muscovite (32%) along with quartz (58%) increase in abundance at the expense of the sodic plagioclase, which almost completely disappears. Other minerals, such as chlorite (3%) and epidote (3%), also decrease in abundance. In summary, this profile reflects a marked change in the mineralogy of samples as a result of the tonalitic rock interacting with a fluid which resulted in the addition of substantial muscovite (i.e., gain of K_2O) and removal of plagioclase (i.e., loss of Ca) and Na_2O), which is further explored below with the use of lithogeochemistry for the same sample suite.

4.2 Whole Rock Geochemistry and Mass Balance

Lithium metaborate/tetraborate fused samples from domains A to F were analyzed for their whole rock major element (ICP) and trace element composition (ICP-MS) at Activation Laboratories in Ancaster, Ontario, Canada. The data are presented in Table 3**.** Gold concentration was determined by fire assay ICP-MS to a detection limit of 1 ppb. The FeO contents were determined through titration using cold acid digestion to a detection limit of 0.1%. Sulphur and CO_2 were analyzed by a combustion infrared method to a detection limit of 0.01%. Due to their low concentration, Bi, As, In, Co, Cu, Ag, Cr, Mo, and Ni were reanalyzed through total digestion ICP-MS to detection limits in ppm of 0.02 for Bi, 0.1 for As, 0.2 for In, 0.5 for Co and Cu, 1 for Ag, Cr, Ni and Mo, and 2 for Pb.

Changes in the whole rock major and select trace element geochemistry across domains A to F are summarized in Figure 16**.** Some components, such as Al_2O_3, TiO_2, P_2O_5 and MgO, show little

to no variation in their concentration and are thus relatively immobile (note exception for domain A). In contrast, CaO and Na_2O become progressively more depleted towards the vein, which is not matched by the other major, minor and select trace elements shown. Most other elements have roughly uniform concentrations from domains F to C and then increase in concentration towards the most altered samples proximal to the vein (e.g., K_2O, Li, Rb, Ba, Cs, LOI (as H), Cu, Au, S, F). Both FeO and Fe_2O_3 show similar patterns with overall increase in concentration towards the vein, but Fe_2O_3 increases proximal the vein whereas FeO slightly decreases. For the REE, a significant difference is noted in the chondrite normalized patterns for the altered samples compared to the least altered (domain F), the latter of which is similar to data for the tonalite at the deposit area (inset Fig. 16f). Across the alteration profile there is a systematic decrease in the ΣHREE values (i.e., 82 ppm for sample F to 60 ppm for sample A), whereas for the LREE the behaviour is more erratic with samples similar to or enriched compared to the least altered sample. In all samples the magnitude of the Eu anomaly (i.e., Eu^*/Eu_N), which in all cases is negative, remains similar.

Elemental gains and losses during alteration have been assessed across the alteration profile with mass balance using Grant's (1986) isocon method (Fig. 17) following a similar approach used in other studies of alteration profiles (e.g., Mountain and Williams-Jones, 1989; Halter et al., 1996). The chemical data were corrected for mass change using Al_2O_3 as the conserved element to calculate the mass factors, but it is noted that SiO_2, Ti, and Zr also fall on or close to these isocons (Fig. 17). As seen in the plots, there is elemental loss that reflects the mineralogy of the profile with an initial loss of CaO, which is followed by K_2O, Li, Ba, Rb, through domains E to C; these same samples also show constant mass. In contrast, with development of the most intense alteration, there are significant gains (+100 to +200%) of Fe, K_2O, Li, Ba, Rb, S, F, Cu

and LOI in the last two domains, B and A, where the alteration is most intense. Lastly, the contrast in the behaviour of the REEs is shown for two examples, one for least altered, D versus E, and most altered, B versus A; note that in these plots the isocons shown are inherited from the earlier plots for the same samples. In the first case there is an apparent enrichment of the REEs in sample D whereas for the latter there is a separation of the REEs such that the LREEs are enriched and the HREEs are conserved. The implications of the elemental gains and losses across the profile are discussed in more detail below.

4.3 Elemental Mapping of Pyrite (LA ICP-MS)

Elemental maps of two pyrite grains from the core of the alteration zones at the Candy Cane outcrop were generated using in-situ laser ablation (LA) inductively coupled plasma mass spectrometry (ICP-MS) in the Chemical Fingerprinting laboratory at Laurentian University to measure the enrichment and relative paragenesis of various elements of interest. This was carried out using an Ar plasma quadrupole Thermo X Series II ICP-MS in combination with ArF excimer laser with a wavelength of 193 nm and pulse duration of 20ns using a two-volume sample cell.

The results are shown graphically in Figures 18 and 19 and we note the remarkable similarity of the apparent elemental paragenesis and distribution between the two samples. In general, sample 1 (2 mm x 1.2 mm; Fig. 18), which is a composite grain, shows overall elemental enrichment and patterns that fall into 4 groupings: (i) grain wide enrichment of Se-Co-As-Ni; (ii) a core of Sn-Zn-Cd-In-Pd-Cu; (iii) patchy distribution of Pb-Bi-Te-Sb-Au-Ag where Au-Ag-Sb are coincident; and (iv) a later -stage of W-Mo enrichment within the matrix. Sample 2 actually represents a group of small grains (0.5 mm to 2 mm size; Fig. 19), which generally all show the

same patterns as grain 1. It is noted however that in grain 2 Cu shows a pattern more like group 3 elements than group 2. The elemental maps have also been used to construct an elemental paragenesis (Fig. 20) tracking the temporal relationship between elements during crystallization; the established paragenesis demonstrates well the relationship of the different element groups (1 to 4) noted above.

In order to further examine elemental associations, the data collected for the first grain (sample 1) were broken into time domain slices of about 0.35 seconds each, this being the time used to produce a single analysis for each area ablated by the laser (e.g., 30 μm). For the representative plots of Figure 21, data from about 8,000 point analyses produced from grain 1 were used to quantitatively evaluate the elemental associations noted above. These plots show that for elements such as (i) Co and Ni, (ii) Cd, In, and Zn, (iii) Ag, Au and Te, and (iv) Mo and W there are apparent positive correlations which reflects their spatial coincidence in the pyrite grains analyzed (Fig. 18). In contrast, for other plots, such as As and Co and Se versus As and Ni, correlations are lacking, or as for Bi versus Te and Au they are weak. The plots also illustrate anomalously high values for Au, Te and Cu, which may relate to micro-inclusions of phases containing the respective elements.

For those elements distributed throughout pyrite, the plots for Co, Ni, Se, and As show a continuum with elemental concentrations from 1 to 10,000 ppm for Co, Ni and As, but is more limited for Se (5-100 ppm). Whereas Co and Ni show the typical covariation expected of these elements (Fig. 20), such a relationship is not evident for As with some areas of pyrite enriched in As and depleted in Co and Ni. Lastly, Se is uniform at 10-100 ppm with no apparent variation in terms of Co and Ni (Fig. 21). For those elements (Zn-Cd-In-Sn-Pd; also Ge but not plotted) with

well-defined but localized elemental enrichment, strong positive correlations are noted (e.g., Cd and In versus Zn in Fig. 21**).** Similar good correlations are defined for Cu-Pb-Bi-Te and these appear to mimic the distribution of the precious metals (Ag, Au). Thus, for Bi (<100 ppm) versus Te (<12,0000 ppm) a broad correlation is defined, but a small subset of the data appear to indicate the presence of Te-rich phase with lower Bi contents. This latter phase is also seen in the plot of Te versus Ag where most data fall around a Te:Ag ratio of 10:1, but there are also data at higher ratios and Te concentrations which may indicate the presence of micro-inclusions of a Te-rich phase such as hessite (Ag_2Te).

The precious metals show a similar spatial distribution in pyrite, thus it is not surprizing they define a positive correlation (Fig. 21). Furthermore the latter indicates an Au:Ag ratio of about 1:1 to 1:10 for most of the data. The most Ag-rich data are however attributed to the Ag-Te - rich micro- inclusions already noted. The apparent overlap of the precious metals with Cu-Te-Bi-Pb-Sb does not translate into a good correlation of these elements, the Au-Cu, Bi-Au, Te-Au plots being used to illustrate this (Fig. 21**).** In the case of Cu-Au, the high Cu values may be related to micro-inclusions of a Cu-rich phase, likely chalcopyrite (e.g., Large et al., 2007), or Cu as solid solution (Reich et al., 2013), whereas for the Te-Au plot the spikes of Te are likely due to the micro-inclusions already discussed.

Given that the As-Au association is often discussed in gold systems (see review in Deditius et al., 2015), this relationship is also examined in Figure 21. The Au-As plot indicates two groupings of data with Au enrichment in areas of both low (ca. 100 ppm) and high (>1000 ppm) As contents. Also shown in the plot is the Au saturation surface, an important control on gold enrichment in arsenian pyrite (Reich et al., 2005). Of relevance here is that the Au values of >1 to 100 ppm

occur at the inflection point of the Au saturation which indicates the presence of gold nanoparticles in the analysed pyrite. These particles may also be responsible for the elevated Au:Ag ratio observed which indicates that the 1:1 to 1:10 Au:Ag ratio is more typical of these elements in solid solution in the pyrite.

4.4 Stable (S, O) Isotopes

In situ isotopic analyses for both sulfur and oxygen were carried out on pyrite and quartz grains, respectively, occurring in the most altered, central part of the alteration profile (domain A) to gain a better understanding of the constraints on the nature of the mineralizing fluids and ore-forming processes. Two polished thin sections (samples JS13-20A and JS13-29) were analysed by means of secondary ion mass spectrometry (SIMS) at the University of Manitoba, Winnipeg, Manitoba, following the protocols described in Mathieu et al. (2014) for $\delta^{18}O$ and in Tang et al. (2014) for $\delta^{34}S$. The data are reported in standard per mil (‰) format referenced to VSMOW and VCDT, respectively; duplicate analyses of standard materials indicate an error is ±0.4‰ for each isotope. In addition, whole rock $\delta^{18}O$ data were obtained from representative samples of alteration domains (domains, A, B, D and F) at the Queen's Stable Isotope laboratory, Kingston, Ontario, using standard bromine pentafluoride dissolution (Clayton and Mayeda, 1963) followed by mass spectrometric analysis as described in Kontak and Kyser (2011). Data are reported in per mil (‰) referenced to VSMOW and the error is estimated at ±0.1‰.

4.4.1 Results for $\delta^{34}S$ data

Results for 21 analyses of $\delta^{34}S$ in pyrite from quartz vein and alteration halo are summarized in Table 3 and displayed in Figure 22. The data range from -3.7 to -0.7‰ and there is no apparent

difference regardless of the setting of the pyrite in its host. There is also smaller variation and uniform values within most of the domains of grains, such as for the 3 areas in sample JS13-20A (Fig. 22e to f), which indicates the observed variation of about 3‰ is real.

The only other $\delta^{34}S$ data are those reported by Kontak et al. (2013) for pyrite (n=3), molybdenite (n=3) and chalcopyrite (n=5) for the deposit area in addition to chalcopyrite (n=3) from the old Chester 1 vein type deposit. These results were uniform and fell in the narrow range of -1.5 to +1.0‰ with averages of 0‰ for the deposit and -0.5‰ for the Chester vein samples, thus showing slightly heavier $\delta^{34}S$ values than the present study

4.4.2 Results for $\delta^{18}O$ data

The $\delta^{18}O$ analysis was carried out both on rock-forming quartz in the altered tonalite adjacent the vein and for vein quartz itself (Table 3, Fig. 23). The $\delta^{18}O$ for rock-forming quartz in domain A, that is altered tonalite, ranges from +6.4 to +14.4‰ with an average of +11.0 ± 3.2‰ and a median of 10.5‰. If the two highest and lowest values (i.e., 14.4 and 6.4‰) are excluded from the data, as its seems improbable that such a large variation can occur for a magmatic phase, then the remaining 10 samples fall in the range +9.1 to +12.9‰ with an average of +11.2 ± 1.8‰. This latter value is typical of quartz from granitoid rocks in general (Taylor, 1974). Given that the spread of data reported here would be considered large for quartz in igneous rocks based on compilations (e.g. Taylor, 1974), the second averaged quartz value of +11.2‰ is considered to be more representative of the tonalite and provides further reason to exclude the extreme values. In contrast, the $\delta^{18}O$ values for the vein quartz have a smaller range from +7.1 to +12.3‰ with an average of +10.2 ± 0.8‰. The reason for a single sample with a much lower value of +7.1‰ is discussed later.

Oxygen isotope data of mineralized veins from both the current deposit area and the historical Chester 1 deposit were reported by Kontak et al. (2013). In their study, vein material of 13 samples taken from the deposit area yielded values from +9.7 to +11.1‰ and averaged 10.6 ± 0.6‰, comparable to the 10.4 4 ± 0.1‰ average that 3 vein samples from Chester 1 exhibited. These isotope values are very similar to the +10.2 ± 0.8‰ average for vein quartz of the present study.

The whole rock $\delta^{18}O$ data provide a sampling across the alteration profile with results given in Table 3**.** The data range from +6.7‰ for the least altered sample, +8.7‰ for an intermediary sample (domain D), and +7.3‰ for the most altered samples (domain A). These values correspond to the low end of the range for whole rock $\delta^{18}O$ values for unaltered granitoid rocks in general which have values of +7 to +11‰ (Taylor, 1974). In comparison, for Archean tonalites specifically, values of +7.1 to 8.2‰ have been reported for samples from various locations within the Superior Province (Valley et al., 1994; Whalen et al., 2002) for which the least altered sample of +6.7‰ compares.

5. Discussion

No single feature can be used to classify gold deposits because the same features can be shared by different deposit types, and structural and metamorphic overprinting can mask original features of the deposits (Sillitoe and Thompson, 1998; Lang and Baker, 2001; Goldfarb et al., 2005; Hart and Goldfarb, 2014). For example, in early compilations and studies of IRGD, Sillitoe and Thompson (1998) noted four common criteria for differentiating veins associated with these deposits from those of orogenic type: (i) a spatial and temporal connection, (ii) a

geochemical association (e.g., As-Bi-Te) metal zonation, (iii) established absolute age relationship, and (iv) a certain fluid composition. They noted, however, that these characteristics were vague and insufficient to distinguish between the two deposit types. Similar conclusions were subsequently reached by Groves et al., (2003) and Goldfarb et al., (2005) in their discussions of these two deposit types. In the most recent review of this subject, Goldfarb and Groves (2015) arrived at a similar conclusion.

The most recent defining features for differentiating between the reduced intrusion-related gold (RIRG) deposits, a subset of the IRGS settings, and other deposits, based on well-studied igneous-related deposits globally, include a combination of multiple mineralization styles, presence of sheeted veins, contemporaneity of mineralization and causative pluton, a reduced oxidation state of the intrusion, the established Au-Bi-Te-As metal association, concentric metal zoning around a plutonic center, and features (e.g., evidence for fractionation and fluid exsolution) that indicate the presence of hydrothermal and mineralizing fluids originating from a causative intrusion (Lang and Baker, 2001; Hart and Goldfarb, 2014). Since the Côté Gold deposit is considered an oxidized porphyry-style deposit (Katz, 2016), these features do not directly apply, but they are considered here because the sheeted veins at the Côté Gold deposit (i.e., Candy Cane outcrop) resemble those associated with igneous-related gold deposits (parallel orientation, single-stage, extensional, intrusion-hosted, Au correlative Bi-Te association).

The following discussion examines the origin of the vein type mineralization in the ore envelope and immediately surrounding area of the Côté Gold deposit in light of the new structural observations and geochemical data presented in previous sections. The structural data will be further used to constrain the original geometry and attitude of the veins.

5.1 Structural timing of the sheeted veins at the Côté Gold deposit

The RDZ is characterized by a strong S_2 foliation, which is axial planar to the regional folds lying outside of the deformation zone. Early movement along the RDZ is dominated by north-side-up movement parallel to a steeply-plunging stretching lineation (L_2). Subsequent, S-shaped folding of the S_2 foliation, presumably due to sinistral shearing along the RDZ, locally transposed S_2 parallel to a S_3 crenulation cleavage. The RDZ then underwent late dextral reactivation as indicated by the presence of Z-shaped drag folds with an axial planar S4 cleavage, dextral shear bands, and back-rotated boudinaged quartz veins.

Similar structures are observed within the deposit area, as observed in several outcrops studied in detail. An early north-side-up, east-trending shear zone at the South Breccia outcrop was reactivated as a south-side-up shear zone with a sinistral strike-slip component. Reversal of shearing crenulated the early S_2 shear zone foliation and produced a new S_3 crenulation cleavage. The latter cleavage is expressed on the North Breccia and Chipmunk outcrops as a penetrative foliation which becomes more pronounced in a south-side-up, sinistral shear zone at the North Breccia outcrop. A narrow dextral shear zone overprints the foliation at the Chipmunk outcrop, and dextral shearing reactivated a narrow shear zone with both sinistral and dextral shear sense indicators at the North Breccia outcrop. Thus, the deformation history of these outcrops parallel that of the RDZ, that is, an early north-side-up shearing and the formation of an S_2 foliation is followed by sinistral shearing and the formation of new S_3 foliation, which is in turn overprinted by structures that formed during a late dextral reactivation event. These observations together suggest that the CIC and the Côté Deposit area were subjected to the same deformation events as the RDZ.

The chronology of the veins with respect to deformation events is readily apparent at the North Breccia outcrop where veins outside of the east-trending shear zone are cut by a lamprophyre dike which is sheared and offset along the same shear zone. As the foliation within the shear zone strikes 265°and is oriented 10° clockwise of the trend of the shear zone, the shortening direction required to produce the foliation and to cause sinistral strike-slip shear along the shear zone must lie in the quadrant containing the normal to the foliation (Fig. 24). At the Candy Cane outcrop, the foliation within the alteration halo of the veins strikes 290° and is oriented 10° anticlockwise of the trend of the veins. The foliation typically undergoes a clockwise deflection, suggesting dextral shear. The quadrant containing the shortening direction required to produce the foliation and induce dextral shear is shown in Figure 24. Superposition of the two quadrants from North Breccia and Candy Cane provides a range in the orientation of the shortening direction that could induce dextral shearing along the Candy Cane veins and sinistral shearing along the North Breccia veins. It ranges from 340° to 030° with an average orientation of 005°, which is similar to the shortening direction deduced from the set of conjugate shears at the Candy Cane outcrop. Elsewhere on this outcrop, the foliation overprints the alteration halo of two main vein sets without deflection, further suggesting that the veins and the phyllic alteration haloes pre-date formation of the foliation.

The emplacement of the veins prior to regional deformation of the CIC suggests that the veins and their weak alteration haloes acted as structural anisotropies that focused and localized the formation of the foliation and shearing, which either had a dextral or sinistral strike-slip component depending on the orientation of the vein with respect to the shortening direction. The alteration halo of the veins is rich in sericite, thus a strong foliation could have developed in such cases, whereas elsewhere on these outcrops no or only a weak foliation could form because of

the more massive and rheologically competent nature of the relatively unaltered diorite and tonalite.

5.2 Geochronological Controls on Timing of Deformation and Mineralization

The RDZ straddles the contact between metavolcanic rocks of the ca. 2740 Ma Chester Group and the 2682 ± 1 Ma Neville pluton (van Breemen et al., 2006), thus providing a maximum age of ca. 2682 Ma for the formation of the RDZ and the deformation of the CIC and veins. A Re-Os age of 2746.8 ± 11.4 Ma on molybdenite (Katz et al., 2015, 2016) from a gold-bearing vein in the shear zone at the North Breccia outcrop (Fig. 9b) further suggests that the emplacement of the sheeted veins predates regional deformation. Several other Re-Os molybdenite ages for gold-bearing and gold barren vein samples from the deposit (Kontak et al., 2013; Katz et al., 2015) are also centred on 2740 Ma and pool to provide a best age of 2740.2 ± 5.6 Ma (Katz, 2016). This age also overlaps with the ca. 2740 Ma age of CIC magmatism (Kontak et al., 2013; Katz et al., 2015, 2016). This overlap in age between mineralizing and magmatic events is characteristic of igneous-related sheeted veins (Hart and Goldfarb, 2014) and represents a gap of at least 60 Ma between the timing of vein mineralization and that of the regional deformation overprinting the CIC.

5.3 Relationship between Gold Grade and Deformation

Samples collected at the South Breccia and Candy Cane outcrops were used to constrain the upgrading or downgrading effects of deformation on pre-existing gold concentrations. Samples taken across the shear zone at the South Breccia outcrop show little to no variation in grade (Fig. 7) with samples collected from within the shear zone yielding gold grades of 1.014 g/t (n = 7)

and samples collected from the less deformed wall rocks yielding average gold grades of 0.775 g/t (n = 4). At the Candy Cane outcrop, samples of foliated phyllic alteration haloes returned lower average grades (0.029, n = 5) than unfoliated phyllic alteration haloes (0.219, n = 5) **(**Fig. 11, Table 2**)**. These data suggest that deformation had no upgrading effect on the gold mineralization and may even have had a downgrading effect on the mineralization associated with the veins. The most important aspect regarding the detailed sampling of veins and alteration zones in the two outcrop areas is that there appears to be a general lack of correlation between gold grades and deformation. This observation suggests that gold was not introduced during the development of structures overprinting the pre-existing veins and CIC and provides further independent evidence and additional support for the above suggestion that the gold mineralization pre-dated the deformation event.

5.4 Implications of Mineralogical, Geochemical and Isotopic Studies of the Zoned Alteration Profile

The mineralogical, geochemical and stable isotope study of the veins and alteration halo was carried out to constrain the nature of the hydrothermal fluids and the origin of the veins. This approach follows that of others (e.g., Mountain and Williams-Jones, 1996; Halter et al., 1996) who showed the validity of using sequential sampling methods to assess the nature of alteration attending mineralized systems. The results of each component of the study are discussed below, starting with the mineralogical changes in the host tonalite during hydrothermal alteration, followed by the mass balance of the alteration profile, elemental associations mapped within pyrite, and the isotope analysis of whole rock and quartz ($\delta^{18}O$) and pyrite ($\delta^{34}S$) within the veins and surrounding tonalite.

5.4.1 Petrographic, SEM-EDS and Rietveld data

The alteration profile enveloping the veins can be divided into three dominant alteration zones characterized by saussuritization (domains F to D), albitization (domains D to B), and sericitization (domain A), as based on the detailed petrographic observations integrated with Rietveld analysis. The primary mineralogy of the host tonalite consists of 40-50% quartz and 50-60% plagioclase (An_{30}). Its alteration results from reactions with hydrothermal fluids focused along a fracture, now represented by the central quartz vein (Fig. 13**),** which sealed the system and terminated influx of the hydrothermal fluids. The width of the alteration halo is not dictated by the width of the vein, which is consistent with the vein representing the latest stages or expression of the hydrothermal system. The ubiquitous chlorite across the alteration halo represents alteration of an earlier, secondary hydrothermal biotite, which formed during the first alteration stage of the deposit area (see discussion in Kontak et al. (2013) and Katz (2016)) and observed around the Candy Cane outcrop. Importantly this biotite hosts LREE-rich phases elsewhere in the deposit area, such as bastnaesite and allanite (Kontak et al., 2013; Katz, 2016), and their presence here along with titanium-bearing minerals ilmenite, titanite and rutile (Fig. 13e), is therefore consistent with the alteration of biotite to chlorite. Chlorite is typically concentrated at the tip of the fractures, at the boundary interface between the sericite and albite alteration zones, and as ripidolitic chlorite found in Fe-rich zones in the core of the profile. In the sections below the origin of the mineralogy of each of these zones is addressed.

Saussurite zone: This zone is the most distal from the central fracture and vein. It is characterized by saussuritized plagioclase and quartz. The host rock retains a primary magmatic texture that was slightly modified during deformation, as indicated by the presence of elongate

quartz. During saussuritization, primary plagioclase was partially replaced by albite, sericite and epidote due to the liberation of Ca and K (Plümper and Putnis, 2009). Minor calcite is present and represents a weak distal expression of the saussurite alteration. The causative fluid related to this alteration is considered however to be metamorphic in origin because of the widespread occurrence of this style of alteration across the CIC and is independent of mineralization (Kontak et al., 2013). The presence of albite alteration, next described, would preclude saussuritization to have occurred since such rocks would have been depleted in calcium.

Albite zone: This zone, closer to the central vein and fracture, is characterized by albitization of plagioclase and the formation of coarse-grained epidote. Rare grains of saussuritized plagioclase are present and are interpreted as earlier plagioclase grains that were incompletely albitized by the hydrothermal event, thus containing sufficient calcium to react with metamorphic fluids to form epidote (see Fig. 14). The primary igneous texture of this rock is not preserved, as the primary quartz grain boundaries are modified through coupled dissolution and reprecipitation processes attending the hydrothermal alteration event (Putnis 2002, 2010). This alteration is symmetrically distributed about the central vein and fracture and therefore is related to the formation of the vein and fracture. It is also important to note that albization is commonly seen bordering quartz veins in the main deposits area (Kontak et al., 2013; Katz, 2016).

Sericite zone: This zone, immediately adjacent the central vein, is characterized by the addition of quartz and by intense sericitization producing the prominent striping observed on the outcrop (Fig. 12A). The amount of quartz present in the rock increases due to plagioclase being altered to sericite with this reaction liberating silica which immediately saturated to form the new quartz **(**Figs. 14b, 15). The sericite alteration zone is therefore akin to the development of phyllic

alteration in porphyry deposits (Sillitoe, 2010; Seedorff et al., 2005). This zone reflects the area of highest fluid:rock ratio and best indicates the nature of the altering fluid, which is characterized below with the use of mass balance.

5.4.2 Whole Rock Geochemistry and Mass Balance

The geochemistry of domains F to A reflects an increase in the fluid to rock ratio of the alteration profile towards the vein as the rock equilibrates with the incoming fluid composition. Elemental trends and mass balance provide insight into the extent of fluid infiltration within a specific alteration zone, where completely mobile elements in a progressive alteration would have a linear trend (Mountain and Williams-Jones, 1995). The mass balance therefore provides a geochemical signature of the altering fluid as noted by those elements that record net gains.

Using first the major elements, SiO_2 shows little absolute variation across the chemical profile until the last stage where there is a dramatic increase, as reflected in both the abundance and texture of quartz in the Rietveld diagram noted above (Fig. 14b, 15). This increase in silica is only apparent, however, as the mass balance shows no gain of silica (i.e., it is conserved) and instead reflects the net loss of sodium at the expense of sodic plagioclase (domain B (-25%), A (-80%); Fig. 17). As for CaO, its apparent retention in altered domains D and C reflects epidote stability whereas its depletion in the phyllic zone (-50% for domain B, A; Fig. 17) reflects its breakdown in this zone. The low but consistent presence of K_2O, along with H_2O, in the outer alteration zone is due to sericite after plagioclase, with the sudden increase in the core zone due to net addition of K_2O (to +150%, domains B, A; Fig. 17) and formation of sericite at the expense of albite and commensurate loss of Na_2O. The overall ferric to ferrous ratio in the host tonalite is low (~0.3) and remains consistent across the profile, but the increase in $Fe_2O_3^+$

towards the vein can be attributed to the addition of coarser grained epidote and also the presence of a Fe-rich chlorite noted in the core of the alteration profile. Also of note is that CO_2 is only present in the outer-most zone, this due to the presence of carbonate as part of the regional metamorphic event.

For the trace elements, the parallel trends seen for Li, Rb, Ba and Cs reflect the formation of sericite in the saussuritization zone and the earlier formation of the phyllic alteration zone, as noted previously. Whereas these elements are conserved in the former zone, they show absolute gains in the latter (+100 to +150%; Fig. 17) and mimic the trend of K_2O.

The abundance of the REEs and their chondritic profiles depart from that of the least altered tonalite for all the samples with notable LREE enrichment and a more fractionated pattern, the latter reflected by higher $(La/Lu)_N$ than in the typical tonalite at the deposit. This LREE enrichment is considered to be part of the biotite alteration assemblage within the Côté Gold deposit (Kontak et al., 2013; Katz et al., 2015) and to reflect the pre-existing distribution of LREE phases, such as bastnaesite and allanite seen in biotite, before formation of the phyllic alteration. Thus although REEs are commonly noted to be conserved elements (i.e., immobile) in alteration profiles and mass balance calculations, their erratic distribution precludes using them in this study. Associated with the variable LREE enrichment is the behaviour of F, which likely reflects the present of bastnaesite.

The geochemical signature of the alteration fluids reflects the addition of LILE (K, Li, Rb, Cs, Ba), Fe, and elements related to mineralization (S, Cu, Au). This signature is comparable to the phyllic alteration that occurs throughout the Côté Gold deposit (Katz, 2016) and might therefore be considered to indicate a magmatic signature. In this context, however, it is noted that the

addition of S, H_2O, CO_2 and enrichment of elements such as K_2O, Na_2O, Rb, Sr, Li, Cs, Tl and Ba are is also cited as typical of some orogenic gold deposits (Goldfarb et al., 2005). Hence, the noted chemical signal of the fluid, although consistent with a magmatic origin, is in isolation not necessarily diagnostic of such an origin.

5.4.3 Elemental Mapping of Pyrite (LA ICP-MS)

The elemental maps for pyrite (Figs. 18, 19) within the mineralized veins at the Candy Cane outcrop are generally characterized by homogenous distribution of some elements and a patchy to erratic distribution of others. Examination of the spatial distribution of elements indicates four element groups and, when integrated with quantification of elemental contents (see below), provides the following insight: (i) Co (to 10,000 ppm), Ni (to 8,000 ppm), As (to 10,000 ppm), and Se (to 100 ppm) share a common spatial distribution but different homogenous abundances in the pyrite and reflect the growth history of their host, as is common for these elements in hydrothermal pyrite (e.g., Large et al., 2009; Lawley et al., 2015; Gao et al., 2015). The distribution and concentrations of these elements are considered to reflect crystallographic controls, (ii) Elements with a more isolated enrichment in the core areas include Zn (to 10,000 ppm), Cd (to 100 ppm), In (to 100 ppm), Sn (to 20 ppm) and Pd (to 0.5 ppm). Again, a crystallographic control to these elements is indicated from their sharp and coincident distribution, (iii) Elements with a less well-defined pattern but which are concentrated in the central parts of pyrite and in part overlap with group 2 elements. This group includes Cu (to 20,000 ppm), Te (to 10,000 ppm), Pb (to 200 ppm), Bi (to 100 ppm), Sb (to 10 ppm) and Pd (to 0.5 ppm), in addition to the precious metals Au (to 10,000 ppm) and Ag (to 10,000 ppm). It is noted that of this group, Au-Ag-Sb share a common spatial pattern with a diffuse outer zone, (iv)

A late-stage assemblage of W and Mo which post-date pyrite and are present in the matrix material.

Using element distribution maps, a relative elemental paragenesis can be inferred (Fig. 21), the importance of which is that this reflects the changing element budget of the fluid with time. For the two areas mapped, it is apparent that the precious metals (Au-Ag) appear to overlap the earlier stage of pyrite but do not extend through its entire growth history like, for example, the assemblage Ni-Co-As-Se does. In fact, the same can be said for element groups 2 (Zn-Cd-In-Sn-Pd) and 3 (Cu-Te-Pb-Bi-Sb). Furthermore, whereas group 2 elements show sharp change in their concentrations and suggest an abrupt change in the chemistry of the fluid, the diffuse outlines for the Au-Ag-Sb of group 3 elements suggest that there may have been some modification of their original concentration. Although more detailed study is required, the textures are suggestive of a coupled dissolution and precipitation process (Putnis, 2002; Putnis and John, 2010). In contrast to all the other elements, Mo and W in fact post-date pyrite as these elements are seen to occur in the matrix of the samples.

The last element group noted is the pairing of W and Mo. As noted above, these elements post-date pyrite growth and all other elements. There is an overall broad positive correlation of these two elements seen in Figure 21 with both having similar levels of enrichment. As detailed high resolution microscopy has not been done, the actual nature of this elemental enrichment is not known. Of relevance to the W values is the recent suggestion of Cave et al., (2015) that W may be mobilized out of some oxide phases, such as rutile, when altered or converted to another phase (e.g., titanite) during greenschist facies metamorphism. Thus, the late-stage enrichment of

W in the system may relate to alteration of the diorite unit of the CIC complex which contains a variety of Ti-bearing oxide phases (e.g., ilmenite, magnetite, titanite, rutile).

Based on the above it is possible to establish an elemental association for the gold event for the samples from Candy Cane (Fig. 20). The data indicate that coincident with enrichment of Au in the mineralizing fluids there was also Cu, Te, Pb, Bi and S, but of these Cu and Te were the most enriched. In addition, the data indicate an Au:Ag ratio of 1:1 to 1:10 for this system. Since the elemental maps show group 1 elements were present during pyrite growth, they are not considered a discriminatory part of the geochemical signature of the gold system. The Au-Cu-Te-Pb-Bi-S association is not characteristic of a distinct deposit type, but do however shares similarities with reduced intrusion-related gold (RIRG) deposits (Au-As-Bi-Sb) (Sillitoe and Thompson, 1998), the syenite clan (Au-Cu-Bi-Te ± Mo) (Poulsen et al., 2000) and some orogenic systems (Au-Ag-As-W-Bi-Sb-Te-Mo and slightly anomalous Cu, Pb and Zn) (Poulsen et al., 2000; Dubé and Gosselin, 2007) and is therefore not discriminatory. We do note however of the unusual presence of Pd in one of the studied samples and that such enrichment is usually associated with alkaline porphyry systems (ex. Eliopoulos and Economou-Eliopoulos, 1991; Werle et al., 1983). This singular sample is therefore cautiously interpreted to indicate a magmatic signature to the fluid system which the elevated In (Sinclair et al., 2007; Andersen et al., 2016) and, in one grain, Pd (e.g., Sinclair and Jonasson, 2014) may support. Also relevant is suggestion of Deditius et al. (2015) that the presence of gold particles (Fig. 21) is more typical of porphyry and epithermal systems where thermal fluctuations occur versus metamorphic related settings where thermal pulsation is more unlikely. The findings here contrast in one very important way with the results of Gao et al. (2015b) who provided elemental maps for pyrite from the main deposit area, including material from the magmatic-hydrothermal breccia body. In

their study they noted that Au post-dated pyrite growth whereas other elements (Ni, Ag, Te, Sb, Bi) were enriched in pyrite. The reason for the different results of these two studies must reflect either one or both of the timing of elemental enrichment in the fluid and also the precipitation mechanism, and will be an obvious area for future studies. Since the Côté Gold deposit is considered analogous to an oxidized porphyry setting (Katz, 2016), the similarities made to the RIRG deposits are not directly valid. However, similarities exist in oxidized syenite settings in the Abitibi which have associations of Au-Ag-Te-W-Mo-Bi-Sb-Pb with early Co-Ni-As, such as in the Macassa mine in Kirkland Lake and Western Timmins camp (Ispolatov et al., 2008; Campbell, 2014), and sheeted veins with an Au-Bi-Te ± W ± Mo ± As association related to the Fort Knox intrusion-related porphyry-type system in Alaska (Bakke, 1995).

5.4.4 Stable (S, O) Isotopes

The stable isotopes of S and O provide insight into the nature and origin of fluids in hydrothermal ore systems and have, therefore, formed an important part of such studies (e.g., Taylor, 1979; Ohmoto and Rye, 1979). In terms of gold systems, there have been compilations for these isotopes, in particular for Archean settings (Kerrich, 1987; McCuaig and Kerrich, 1994; Beaudoin, 2011), which provide a basis for comparison. In the most recent discussion of such data in relation to gold deposits, Goldfarb and Groves (2015) note that most of these data are equivocal in the context of genetic models, thus confirming earlier reviews of such data (e.g., Goldfarb et al. 2005). The results of the in situ SIMS analysis for $\delta^{34}S$ and $\delta^{18}O$ are discussed below in the context therefore of ore systems in general and gold deposits specifically with the idea of providing some constraints on the nature of the mineralizing fluids and ore-forming processes.

5.4.4.1 Results of $\delta^{34}S$ data

The data presented and discussed above indicate there is both uniformity of the $\delta^{34}S$ pyrite data within each of the two samples analysed and a small overall range from -3.7 to +0.7‰ for the 21 analyses. Importantly, these results are also comparable to analyses of sulphides, including pyrite, chalcopyrite and molybdenite, for the main Côté Gold deposit which are centred on 0‰ (Kontak et al., 2013). The similarity of these results, including data for the Chester 1 vein deposit as noted above, are permissive with a similar sulphur reservoir and redox state for the mineralizing fluids. The narrow range for the $\delta^{34}S$ data also has a few important implications, namely that there was a uniform and well mixed sulphur reservoir and that fluid system likely remained below the SO_2/H_2S redox boundary such that there would have been insensitive to redox changes (Ohmoto and Rye, 1979), as noted in many other studies (Kerrich 1987). The $\delta^{34}S$ values are also well within the overall spread noted for Archean gold deposits in general, which can vary from about -15 to +8‰ (e.g., McCuaig and Kerrich, 1994; Beaudoin, 2011).

The small fractionation between sulphides and $\delta^{34}S_{H2S}$ at temperatures of 300º-400ºC (Ohmoto and Rye, 1979) infer that $\delta^{34}S_{H2S}$ was close to 0‰ and, for the mineral assemblage present, that and $\delta^{34}S_{H2S} \approx \delta^{34}S_{fluid}$, but note this aspect is further discussed below. This $\delta^{34}S_{fluid}$ value of about 0‰ could be derived either directly from a magmatic source or indirectly by dissolution and /or desulfidation of pre-existing magmatic sulphide minerals with a similar value. Although it has already been noted that the data compare in general to compilations of $\delta^{34}S$ for Archean gold deposits, very few of the latter fall below 0‰ and thus have negative values. Where negative values have been noted they are attributed to oxidized nature of the mineralizing fluid and this can occur in both orogenic and intrusion related gold settings. For example , $\delta^{34}S$ values to -10‰

at the Archean Kalgoorlie orogenic gold deposit have been attributed to significant oxidation of the fluids related to extensive wall rock alteration (Evans et al., 2006). In contrast, similarly low $\delta^{34}S$ values for Archean intrusion-related systems in Kirkland Lake, Ontario (Kerrich, 1987; Kontak et al., 2011) and the St. Ives district, Australia (Neumayr et al., 2008) have been attributed to the oxidized nature of the magmatic sourced fluids.

The presence of minor ilmenite and Fe-rich chlorite in the cores of the alteration profiles, along with pyrite as the dominant sulphide, at Candy Cane are consistent with the fO_2 of the system approaching the pyrite-magnetite buffer. In such a scenario the $\delta^{34}S_{H2S}$ signature of the fluid, which may contain both reduced (H_2S) and oxidized (SO_4) sulphur in such cases, is depleted in ^{34}S relative to the bulk $\delta^{34}S$ signature of the fluid with the amount dependent on the fO_2 (Ohmoto and Rye, 1979). Thus, the slightly negative $\delta^{34}S$ values of the analysed sulphides would be consistent with a slightly oxidized fluid. Furthermore, the uniform values in areas but slight variations between areas for $\delta^{34}S$ are also consistent with small local variations in SO_2/H_2S ratios of the fluid. Thus the slightly depleted $\delta^{34}S$values reported here may arise from fluid:rock interaction and commensurate with the oxidation of the fluid in the same manner as that proposed to explain the low $\delta^{34}S$ values observed at Kalgoorlie. In the latter case however the much lower $\delta^{34}S$ values for pyrite (i.e., to -10‰) reflected the presence hematite replacing magnetite in the core of the alteration profile.

In summary, the $\delta^{34}S$ data at Candy Cane are consistent with an original fluid having a $\delta^{34}S_{fluid}$ value of about 0‰, as seen for the vein sulphides in the main deposit area, having been modified due to fluid:rock interaction. The latter may have altered the redox state of the fluid so fraction occurred which would result in the $\delta^{34}S_{H2S}$ of the fluid becoming slightly negative thereby

accounting for the measured $\delta^{34}S_{pyrite}$ values of -3.7 to +0.7‰. The data are also consistent with the sulphur being sourced from a homogeneous reservoir having a magmatic signature.

5.4.4.2 Results for $\delta^{18}O$ data

The $\delta^{18}O$ data are interpreted first for the vein quartz analysis followed by the tonalite quartz and whole rock data. First, in the case of the quartz $\delta^{18}O$ values, the observed range of +7.1 to +12.4‰ compares to the range of +10 to +16‰ for Archean gold deposits, both orogenic and intrusion related, in the AGB (McCuaig and Kerrich, 1994; Beaudoin, 2011). Of particular note in this context is that 3 analysis fall below +10‰ which might suggest fluid mixing, a process documented to have occurred in some of these deposits (Beaudoin and Pitre, 2005; Beaudoin and Chiaradia, 2016). As noted above, additional data for vein quartz from both the Côté Gold deposit proper and the Chester vein system centre on about +10‰, thus at the low end of the range for the AGB. Thus, for both the Candy Cane samples and the deposit in general, the $\delta^{18}O$ values fall at the extreme end of the spectrum. The reason for this apparent difference can be addressed using the calculated $\delta^{18}O_{H2O}$ values for the vein forming fluids. Using for example the fractionation equation of Matsuhisa et al. (1979) at 400°C (i.e., $\Delta_{quartz\text{-}H2O}$ = 4.1‰), this equates to $\delta^{18}O_{H2O}$ values of between +3 and +8.3‰ (Table 3) with an average of +6.1‰. These values lie below the low end of the range for both magmatic (+6 to +10‰) metamorphic (+5 to +20‰) waters (Sheppard, 1986) and indicate therefore fluid mixing must have occurred to account or the low $\delta^{18}O_{H2O}$ values. Furthermore, given that $\Delta_{quartz\text{-}H2O}$ = 6.9‰ (Matsuhisa et al. 1979) at 300°C, which thus provides a more realistic temperature range for vein formation, this equates to lowering the calculated $\delta^{18}O_{H2O}$ values to between +0.2 and 5.5‰ and an average of +3.3‰. Thus the vein $\delta^{18}O$ quartz data clearly indicate vein formation involved mixing of a primary

fluid having a minimum $\delta^{18}O_{H2O}$ value of +8.3‰, assuming a maximum temperature of 400°C and using the heaviest $\delta^{18}O_{quartz}$ value, and a ^{18}O depleted fluid. The origin of the latter fluid is inferred to be heated down-welling seawater based on the current working model for the deposit, this being a subvolcanic porphyry-typesetting setting (Katz et al., 2015, 2016). In order to confirm the above conclusion, the $\delta^{18}O$ whole rock data for the sample from domain A (+7.3‰) and the average $\delta^{18}O_{quartz}$ SIMS value (+11.2‰) are used to indirectly calculate the $\delta^{18}O_{H2O}$ value for the fluid which altered this rock. In this case, the modal mineralogy (i.e., quartz (60%) and muscovite (40%)) and mass balance were used to calculate a $\delta^{18}O$ value of 1.5‰ for the muscovite. Using this latter value and the $\Delta_{muscovite-H2O}$ fractionation values at 400°C (+1.5‰, O'Neil and Taylor 1969; 0‰, Zheng 1993), then a $\delta^{18}O_{H2O}$ value of between +1.5 and +0‰ are inferred. Although this calculation has some challenges (e.g., variation in $\delta^{18}O_{quartz}$ SIMS values), the calculated $\delta^{18}O_{H2O}$ value approximates the lower end of the inferred range for $\delta^{18}O_{H2O}$ based on the vein quartz values analyzed by two methods in independent studies.

Whole rock $\delta^{18}O$ data can also be used to evaluate water:rock interaction in hydrothermal systems based on some simple assumptions (Taylor, 1977), as has been successfully demonstrated in a variety studies (e.g., Cathles, 1993; Mercier-Langevin et al., 2014; Dostal et al., 2015). In the above discussion the most altered sample from the alteration profile was used to estimate the $\delta^{18}O$ value of the reacting fluid, whereas here we use data for both the more distal and less altered sample and the same most altered sample to address the water:rock ratio and temperature of interaction. Discussing first the least altered sample with $\delta^{18}O$ = +6.7‰, if the average $\delta^{18}O$ quartz SIMS value of +11.2‰ is used along with its modal mineralogy and mass balance constraints, then the $\delta^{18}O$ value of the non-quartz component of the sample (i.e., plagioclase) is calculated to be +4.5‰. The latter value contrasts with an inferred original (i.e.,

magmatic) $\delta^{18}O$ value of about 9.5‰ assuming equilibrium fractionation at magmatic conditions (Bottinga and Javoy, 1973) and using the measured SIMS $\delta^{18}O$ quartz value. Even taking into account the variables for the SIMS $\delta^{18}O$ data (i.e., error and variation), the inferred $\delta^{18}O$ value for plagioclase in the least altered rock is still very low and indicates exchange at some point with a low $\delta^{18}O$ fluid (e.g., Criss and Taylor, 1986). We assume in this discussion that this alteration was early and involved the mineralizing fluid. Thus, using the appropriate fractionation factor for feldspar-H_2O it is seen in Figure 25a that a reacting fluid with $\delta^{18}O$ = 0‰, as would be the case for down-welling seawater, will generate the appropriate $\delta^{18}O$ value of +4.5‰ at 300° to 500°C at a water:rock ratio of about 3-10. Using the same approach for the most altered sample adjacent the quartz vein (Fig. 25b), a similar conclusion is inferred with the reacting fluid having to be between 300º and 500°C but with slightly higher water:rock ratios. These findings compare favourably to the similar conclusions of Mercier-Langevin (2014) who also modeled water:rock exchange using whole rock $\delta^{18}O$ data for alteration in an Archean VMS setting that involved interaction with heated seawater.

5.5 Origin of the veins

The combination of features related to the parallel auriferous quartz veins of the CIC discussed thus far include the following: 1) a similar age to the CIC magmatism with a late regional structural overprint; 2) the absence of a positive correlation between gold grade and later deformation fabrics or structures, 3) association of K-rich alteration with enrichment of Rb, Li, Cs, Na, F, and S; 4) LREE enrichment; 5) isotopic evidence for a magmatic input in addition to the influx or mixing with a low $\delta^{18}O$ fluid likely of seawater origin; ; and 6) a Au-Cu-Te-Pb-Bi-S metal association. These features together equate to the defining characteristics of Lang and

Baker (2001) and Hart and Goldfarb (2014) that are considered to be diagnostic for IRGD. Again these latter features which coincide with the observation made at the Côté deposit include vein emplacement prior to regional deformation, a spatial and temporal relationship of veins and a causative intrusion, an Au-Ag-Te-Bi-W-Sb association, and a similar alteration and geochemical signature.

The presence of miarolitic cavities, albeit of local extent, found within the intrusive phases (Katz, 2016), the fine- to medium-grained texture of the tonalite phases of the CIC (Katz, 2016; Berger, 2011), and an inferred coeval relationship for the eastern part of the CIC with the overlying volcanic rocks of the Yeo Formation (Berger, 2012; Katz et al., 2016) suggest the Côté Gold deposit represents a high-level setting. Bedded sequences of felsic tuff and presence of pillowed basalts within the overlying stratigraphy support a subaqueous setting, which is consistent with a suggested seawater component to the mineralizing fluids based on the $\delta^{18}O$ data. These factors collectively suggest that the mineralized vein system is not only intrusion-related, but that the CIC itself is a tilted subaqueous synvolcanic intrusive system, as discussed by Katz et al., (2016). The orientation and distribution of the veins throughout the CIC can prove valuable in the latter context as they provide insight into the stress field present at the time of fracturing.

Sheeted vein systems are characteristic of IRGS and occur most commonly within the pluton's cupola as single-stage, low-sulfide (<5% volume) quartz veins (Hart and Goldfarb, 2014). The geometry of pluton emplacement and the resulting intrusion-related fracture/vein systems are controlled by the interaction between pre-existing structures and anisotropies, and the combination of regional and local plutonic stress fields affecting the cracked thermal aureole

(Tosdal and Richards, 2001; Gloageun et al., 2012). Veins in IRGS are focused in the hydrothermal cracking zone related to cooling and contraction of a magma body during the magmatic to hydrothermal transition of an intrusion (Lang and Baker, 2001; Ioannou and Spooner, 2007). In contrast, orogenic vein systems are controlled by much large-scale regional stress fields and generally result in minimal dimensionality over greater distances.

Where stresses related to a central intrusion dominate the local stress field, then radial and/or concentric vein orientations are localized around the pluton in the plane perpendicular to σ_3 that contains σ_1 and σ_2 (Tosdal and Richards, 2001). The combined factors affecting pluton emplacement and fracture propagation can result in very complex systems. For example, in the case of a tabular pluton, sub-horizontal fractures will propagate laterally away from expanding tips. A shallow magmatic stock will displace the crust upwards and thereby create zones of dilation which may result in a concentric fracture system, as well as steep fracture networks within the overlying volcanic carapace (Tosdal and Richards, 2001). The Wonga gold lode of the Victorian gold fields in Australia and the IRGS of the Tombstone gold belt, Canada, are both examples of how IRGS can have a limited variability in vein orientation due to the local stress at the time of magmatic-related fluid overpressure (Miller and Wilson, 2004; Stephens et al., 2004). The Brués deposit in northwestern Spain is an example of a system that shows an intermediate regional control based on a combined influence of the cracking thermal aureole and moderate surrounding stress field. In this case the irregular pluton dynamics resulted in only parts of the intrusion being mineralized due to zones of localized strain that increased permeability for fluids (Gloaguen et al., 2014).

In the case of the sheeted system within the CIC, the vein geometry is tilted approximately 90° towards the north which would mean that the surficial map represents a near-vertical cross section of its original orientation, where the veins would be dipping between 45° to horizontal. Although the veins appear to be similarly oriented, their timing of emplacement suggests that the stress field would be dominated by local plutonic stresses. These shallow veins could most likely be ascribed to concentric fracturing patterns with a minor radial component controlled by a stress field centered within the deposit area, where σ_3 would be perpendicular to veining direction. However, since the original lateral geometry and full extent of these veins, as well as the location of the center of the mineralizing pluton(s) is unknown, it is difficult to make conclusions about a model representative of the system. Additionally, trace element chalcopyrite abundances, isotopic data and regional mapping suggest that the Chester vein system is genetically related to the IRGS rather than of later orogenic origin as previously thought (Katz, 2016; Kontak, et al 2016). Exploration for gold associated with these IRGS veins should therefore focus within the intrusive complex as opposed to regionally associated with the Ridout deformation zone.

6. Conclusions

The results from this study are used to gain a better understanding of the timing of auriferous vein formation in the 2740 Ma porphyry-type Côté Gold deposit and surrounding area and the nature and origin of the vein-forming fluids. Such information is critical to evaluation the genetic model for this deposit, and other intrusion associated and related mineralized centres, as it impacts the type of exploration in these areas for further discoveries.

Evidence gathered from an integrated detailed mapping and structural analysis of the different vein systems within and surrounding the deposit envelope and regional traverses indicate most importantly that the regional structures related to the younger ca. 2680 Ma RDZ overprint the all the earlier veins of the 2740 Ma Côté Gold deposit. Thus the structural relationships suggest a time gap of at least 50 Ma between vein emplacement and subsequent deformation. In addition, these timing relationships are constrained by a Re-Os age (Katz, 2016) for molybdenite from a well-characterized early auriferous vein in the heart of the deposit.

The fluids responsible for vein formation and related phyllic-like alteration are characterized by a distinct association of K with LILE character (Rb, Li, Cs, Ba, Na, F) in addition to S. The latter alteration overprints an earlier biotite alteration with a LREE rich signature that is similar to the earliest biotite alteration in the mineralized breccia of the main deposit area. Integration of LA ICP-MS mapping of select pyrite grains from these earlier auriferous veins reveal a complex multi-element of Au with Cu-Te-Pb-Bi-S which is permissible with a magmatic source for the fluid. Integration of use of $\delta^{34}S$ and $\delta^{18}O$ isotopes indicate the latter fluid reflects different reservoirs that include a primary magmatic derived fluid that mixed with heated down-welling seawater.

This study demonstrates therefore that although sheeted auriferous veins of orogenic and intrusion-related deposit types can share similar field characteristics, in some cases they can originate from very different processes. The detailed work in this study has clearly shown that despite having features similar to orogenic types vein, the auriferous veins of the Côté Gold deposit pre-date the regional deformation in the area and instead relate to the mineralizing fluid

released from a causative dioritic intrusive phase of the 2740 Ma CIC which was responsible for generating the low-grade high-tonnage porphyry-type Côté Gold deposit.

References

Andersen, J., C.O., Stickland, R.J., Rollinson, G.K., and Shail, R.K., 2016, Indium mineralisation in SW England: Host parageneses and mineralogical relations. Ore Geology Reviews, v. 78, p. 213-238.

Atkinson, B.T., 2013, The Westward Extension of the Larder-Cadillac Fault Through the Kenogamissi Batholith, Abitibi Subprovince, *in* Summary of Field Work and Other Activities 2013. Ontario Geological Survey, Open File Report 6290, p.42-1 to 42-12.

Ayer, J., Amelin, Y. Corfu, F., Kamo, S., Ketchum, J., Kwok, K., and Trowell, N., 2002, Evolution of the southern Abitibi greenstone belt based on U-Pb geochronology: autochthonous volcanic construction followed by plutonism, regional deformation and sedimentation. Precambrian Research, v. 115, p.63-95

Ayer, J.A., Barrett, T.J., Creaser, R.A., Hamilton, M.A., Lafrance, B., and Stott, G.M., 2013, Section 1: Shining Tree and Gowganda Archean gold study and northern Cobalt Embayment Proterozoic vein study. *In:* Results from the Shining Tree, Chester Township and Matachewan Gold Projects and the Northern Cobalt Embayment Polymetallic Vein Project: Ontario Geological Survey, Miscellaneous Release – Data 294.

Ayer, J.A., and Chartrand, J.E., 2011, Geological compilation of the Abitibi greenstone belt. Ontario Geological Survey, Miscellaneous Release Data 282.

Bakke, A.A., 1995, The Fort Knox "porphyry" gold deposit – Structurally controlled stockwork and shear quartz vein, sulphide-poor mineralization hosted by Late Cretaceous pluton, east-

central Alaska. *In:* Porphyry Deposits of Northwestern Cordillera of North America. Canadian Institute of Mining and Metallurgy, Special v. 46, p. 795-802.

Barton, M.D., Stavast, W.J.A., and Maher, D.J., 2008, Root zones of porphyry systems: Extending the porphyry model to depth. Economic Geology, v. 103, p. 939-956.

Beakhouse, G.P., 2011, The Abitibi Subprovince plutonic record: Tectonic and metallogenic implications. Ontario Geological Survey, Open File Report 6268, 161 p.

Beaudoin, G., 2011, The stable isotope geochemistry of orogenic gold deposits. *In:* Barra, F., Reich, M., Campos, E., Tornos, F., eds., Proceedings of the Eleventh Biennial SGA Meeting. Antogfagasta, Chile, p. 556–558.

Beaudoin, G. and Pitre, D., 2005, Stable isotope geochemistry of the Archean Val-d'Or (Canada) orogenic gold vein field. Mineral. Deposita, v. 40, p. 59–75.

Beaudoin, G. and Chiaradia, M., 2016, Fluid mixing in orogenic gold deposits: Evidence from the H-O-Sr isotope composition of the Val-d'Or vein field (Abitibi, Canada). Chemical Geology, v. 437, p. 7-18.

Berger, B.R., 2011, Geological investigations south of Gogama, *in* Summary of Field Work and Other Activities 2011: Ontario Geological Survey, Open File Report 6270, p. 3-1 – 3-7.

Berger, B.R., 2012, Interpretation of geochemistry in the south of Gogama area, *In*: Summary of Field Work and Other Activities 2011. Ontario Geological Survey, Open File Report 6280, p. 3-1 – 3-14.

Bleeker, W., and van Breeman, O., 2010, The fundamental architecture of the south-central Abitibi greenstone belt, Superior craton, Canada, and localization of world-class Au deposits. Abstract *in* Fifth International Archean Symposium, Abstracts, Geological Survey of Western Australia, Record 2010/18, p.153-154.

Bottinga, Y. and Javoy, M. 1973, Comments on oxygen isotope geothermometry: Earth and Planetary Science Letters, v. 20, 250–265.

Campbell, R., 2014, Controls on syenite-hosted gold mineralization in the western Timmins camp. M.Sc. thesis, University of Western, London, Ontario, 159 p.

Cathles, L.M., 1993, Oxygen Isotope Alteration in the Noranda Mining District, Abitibi Greenstone Belt, Quebec. Economic Geology, v. 8, p. 1483-1511.

Cave, B.J, Stepanov, A.S., Craw, D., Large, R.R., Halpin, J.A and Thompson, J., 2015, Release of trace elements through sub-greenschist facies breakdown of detrital rutile to metamorphic titanite in the Otago Schist, New Zealand. Canadian Mineralogist, v. 53, p. 379-400.

Clayton, R. N., and Mayeda, T. K., 1963, The use of bromine pentafluoride in the extraction of oxygen from oxides and silicates for isotopic analysis. Geochim, Cosmochim, Acta, v. 27, p. 43-52.

Criss, R.E., and Taylor, Jr., H.P., 1986, Meteoric-hydrothermal systems.*in* Valley, J.W., Taylor, H.P., Jr., O'Neil, J.R., eds., Stable Isotopes, High Temperature Geological Processes. Reviews in Mineralogy, v. 16, p. 373–424.

Deditius, A. P., 2015, Book Reviews: arsenic-environmental geochemistry, mineralogy and microbiology. Reviews in Mineralogy and Geochemistry, Economic Geology, v. 79, p. 1905-1910.

De Souza, S., Dubé, B., McNicoll, V.J., Dupuis, C., Mercier-Langevin, P., Creaser, R.A., and Kjarsgaard, I.M., 2015, Geology, hydrothermal alteration, and genesis of the world-class Canadian Malartic stockwork-disseminated Archean gold deposit, Abitibi, Quebec. *In:* Targeted Geoscience Initiative 4: Contributions to the Understanding of Precambrian Lode Gold Deposits and Implications for Exploration, (ed.) B. Dubé and P. Mercier-Langevin. Geological Survey of Canada, Open File 7852, p. 113-126.

Devaney, J.R. and Williams, H.R., 1989, Evolution of an Archean Subprovince boundary: a sedimentological and structural study of part of the Wabigoon-Quetico boundary in northern, Ontario. Canadian Journal of Earth Sciences, v. 26, p. 1013-1026.

Dostal, J., Kontak, D.J., Gerel, O., Shellnut, G., and Fayek, M., 2015, Origin of Cretaceous ongonites (topaz-bearing albite-rich micro-leucogranites) from Ongon Khairkhan, Central Mongolia. Lithos, v. 236-237, p. 173-189.

Dubé, B., and Gosselin, P., 2007, Greenstone-hosted quartz-carbonate vein deposits, *In*: Goodfellow, W.D., ed., Mineral Deposits of Canada: A Synthesis of Major Deposit-Types, District Metallogeny, the Evolution of Geological Provinces, and Exploration Methods. Geological Association of Canada, Mineral Deposits division, Special Publication No. 5, p. 49-73.

Eliopoulos, D.G., and Economou-Eliopoulos, M., 1991, Platinum-group element and gold contents in the Skouries porphyry-copper deposit, Chalkidiki Peninsula, northern Greece. Economic Geology, v. 86, p. 740-749.

Evans K.A., Phillips G.N., Powell R., 2006, Rock-buffering of auriferous fluids in altered rocks associated with the Golden Mile-style mineralization, Kalgoorlie gold field, Western Australia. Economic Geology and the Bulletin of the Society of Economic Geologists, v. 101, p. 805–817.

Gao, J-F., Jackson, S.E., Dubé, B., Kontak, D.J., and De Souza, S., 2015, Genesis of the Canadian Malartic, Côté Gold, and Musselwhite gold deposits: Insights from LA-ICP-MS element mapping of pyrite. *In:* Dubé, B. and Mercier-Langevin, P., eds., Targeted Geoscience Initiative 4: Contributions to the Understanding of Precambrian Lode Gold Deposits and Implications for Exploration, Geological Survey of Canada, Open File 7852, p.157-175.

Gloageun, E., Branquet, Y., Chauvet, A., Bouchot, V., Barbanson, L., and Vigneresse, J.L., 2004, Tracing the magmatic/hydrothermal transition in regional low-strain zones: the role of magma dynamics in strain localization at pluton roof, implications for intrusion-related gold deposits. Journal of Structural Geology, v. 58, p. 108-121.

Gloaguen, E., Branquet, Y., Chauvet, A., Bouchot, V., Barbanson, L., and Vigneresse, J.L., 2014, Tracing the magmatic/hydrothermal transition in regional low-strain zones: the role of magma dynamics in strain localization at pluton roof, implications for intrusion-related gold deposits. Journal of Structural Geology, v. 58, p. 108-121.

Goldfarb, R.J., Baker, T., Dubé, B., Groves, D.I., Hart, C.J.R., and Gosselin, P., 2005, Distribution, character, and genesis of gold deposits in metamorphic terranes. Economic Geology, v. 100, p. 407-450.

Goldfarb, R.J., and Groves, D.I., 2015, Orogenic gold: Common or evolving fluid and metal sources through time. Lithos, v. 223, p. 2-26.

Grant, J.A., 1986, The isocon diagram – a simple solution to Gresens' equation for metasomatic alteration. Economic Geology, v. 81, p. 1976-1982

Groves, D.I., Goldfarb, R.J., Robert, F., and Hart, C.J.R., 2003, Gold deposits in metamorphic belts: overview of current understanding, outstanding problems, future research, and exploration significance. Economic Geology, v. 98, p. 1-29.

Halter, W.E., and Williams-Jones, A.E., 1996, The role of greisenization in cassiterite precipitation at the East Kemptville tin deposit, Nova Scotia. Economic Geology, v. 91, p. 368-385.

Hart, C.J.R., 2007, Reduced intrusion-related gold systems; Mineral Deposits of Canada: A synthesis of major deposit types, district metallogeny, the evolution of geological provinces, and exploration methods. *In:* Goodfellow, W., ed., Geological Association of Canada, Mineral Deposits Division, Special Publication, v. 5, p. 95-112.

Hart, C.J.R., Goldfarb, R.J., Lewis, L.L., and Mair, J.L., 2004, The Northern Cordillera Mid-Cretaceous Plutonic Province: Ilmenite/Magnetite-Series Granitoids and Intrusion-Related

Mineralization. A Special Issue of Granites and Metallogeny: the Ishihara Volume, Resource Geology, v. 5(3), p. 253-280.

Hart, C.J.R., and Goldfarb, R.J., 2014, Distinguishing intrusion-related from orogenic gold systems. United States Geological Survey, Denver, Colorado, p. 125-133.

Heather, K.B., 1993, Regional geology, structure, and mineral deposits of the Archean Swayze greenstone belt, southern Superior Province, Ontario. *In:* Current Research, Part C; Geological Survey of Canada, Paper 93-1C, p. 295-305.

Heather, K. B., 2001, The geological evolution of the Archean Swayze Greenstone Belt, Superior Province, Canada, Ph. D. Thesis, University of Keele, Keele, England, 370 p.

Heather, K.B., Shore, G.T., and van Breemen, O., 1996, Geological investigations in the Swayze greenstone belt, southern Superior Province, Ontario: a final field update. *In:* Current Research 1996-C; Geological Survey of Canada, p. 125-136

Helt, K.M., Williams-Jones, A.E., Clark, J.R., Wings, B.A., and Wares, R.P., 2014, Constraints on the genesis of the Archean oxidized, intrusion-related Canadian Malartic gold deposit, Quebec, Canada. Economic Geology, v. 100, p. 713-735.

IAMGOLD Corporation, 2014, IAMGOLD reports 2014 reserves of 86 million ounces and measured and indicated resources of 21.4 million ounces: IMG press release, February 18, 2015.

Ioannou, S.E., and Spooner, E.T.C., 2007, Fracture analysis of a volcanogenic massive sulfide-related hydrothermal cracking zone, Upper Bell River complex, Matagami, Quebec: Application of permeability tensor theory. Economic Geology, v. 102, p. 667-690.

Ispolatov, V., Lafrance, B., Dubé, B., Creaser, R., and Hamilton, M., 2008, Geologic and structural setting of gold mineralization in the Kirkland Lake-Larder Lake gold belt, Ontario. Economic Geology, v. 103, p. 1309-1340.

Katz, L.R., Kontak, D.J., Dubé, B., and McNicoll, V., 2015, The Archean Côté Gold intrusion-related Au(-Cu) deposit, Ontario: a large tonnage, low-grade deposit centred on a magmatic-hydrothermal breccia. *In:* Dubé, B. and Mercier-Langevin, P., eds., Targeted Geoscience Initiative 4: Contributions to the understanding of Precambrian lode gold deposits and implications for exploration, Geological Survey of Canada, Open File 7852, p. 139-155.

Katz, L.R., 2016, Geology of the Archean Côté Gold Au(-Cu) intrusion-related deposit, Swayze greenstone belt, Ontario: Ph.D. thesis, Laurentian University, Sudbury, Ontario, 370 p.

Katz, L.R., Kontak, D.J., Dubé, B., and McNicoll, 2016, The geology, petrology and geochronology of the Archean Cote Gold large-tonnage, low-grade intrusion-related Au(-Cu) deposit, Swayze greenstone belt, Ontario Canada. Canadian Journal of Earth Sciences. DOI: 10.1139/cjes-2016-0007.

Kerrich, R., 1987, The stable isotope geochemistry of Au-Ag vein deposits in metamorphic rocks: *in* Kyser, T.K., ed., Stable isotope geochemistry of low temperature fluids. Mineralogical Association of Canada Short Course, v. 13, p. 287-336.

Kontak, D.J. and K. Kyser, 2011, A fluid inclusion and isotopic study of an intrusion-related gold deposit (IRGD) setting in the 380 Ma South Mountain Batholith, Nova Scotia, Canada: evidence for multiple fluid reservoirs: Mineralium Deposita, v. 46, p.337-363.

Kontak, D.J., Creaser, R.A., and Hamilton, M.A., 2013, Section 2: Geological and geochemical studies of the Côté Lake Au(-Cu) deposit area, Chester Township, Northern Ontario, *In*: Results from the Shining Tree, Chester Township and Matachewan Gold Projects and the Northern Cobalt Embayment Polymetallic Vein Project. Ontario Geological Survey, Miscellaneous Release – Data 294.

Lafrance, B., De Wolfe, J., and Stott, G.M., 2004, A structural reappraisal of the Beardmore-Geraldton Belt at the southern boundary of the Wabigoon Subprovince, Ontario, and implication for gold mineralization. Canadian Journal of Earth Sciences, v. 41, p. 217-235.

Lafrance, B., 2008, The formation of the Sudbury breccia in the North Range of the Sudbury impact structure. Precambrian Research, v. 165, p. 101-119.

Lafrance, B., 2015, Geology of the orogenic Cheminis gold deposit along the Larder Lake-Cadillac deformation zone, Ontario. Canadian Journal of Earth Sciences, v. 12, p. 1093-1108.

Lang, J.R., and Baker, T., 2001, Intrusion-related gold systems: the present level of understanding. Mineralium Deposita, v. 35, p. 447-489.

Large, R.R., Maslennikov V.V., Robert F., Danyushevsky L. and Chang Z., 2007, Multistage sedimentary and metamorphic origin of pyrite and gold in the giant Sukhoi Log deposit, Lena gold province, Russia. Economic Geology. v. 102, p. 1233-1267.

Large, R.R., Danyushevsky, L., Hollit, C., Maslennikov, V., Meffre, S., Gilbert, S., Bull, S., Scott, R., Emsbo, P., Thomas, H., Singh, B., and Foster, J., 2009, Gold and trace element zonation in pyrite using a laser imaging technique: Implications for the timing of gold in orogenic and Carlin-style sediment-hosted deposits. Economic Geology, v. 104, p. 635–668.

Lawley, C.J.M., Creaser, R.A., Jackson, S., Yang, Z., Davis, B., Pehrsson, S., Dubé, B., Mercier-Langevin, P., and Vaillancourt, D., 2015, Unravelling the Western Churchill Province Paleoproterozoic gold metallotect: constraints from Re-Os arsenopyrite and U-Pb xenotime geochronology and LA-ICP-MS arsenopyrite trace element chemistry at the BIF-hosted Meliadine Gold District, Nunavut, Canada. Economic Geology, v. 110, p. 1425-1454.

Mathieu, L., 2016, Quantifying hydrothermal alteration with normative minerals and other chemical tools at the Beattie Syenite, Abitibi greenstone belt, Canada. Geochemistry, Exploration, Environment, Analysis, v. 16.

Matsuhisa, Y., Goldsmith, J.R., and Clayton, R.N., 1979, Oxygen isotopic fractionation in the system quartz-albite-anorthite-water. Geochimica et Cosmochimica Acta, v. 43, p. 1131-1140.

McCuaig, T.C. and Kerrich, R., 1994, P-T-t-deformation-fluid characteristics of lode gold deposits: Evidence from alteration systematics. *In:* Lentz, D.R., ed., Alteratin and Alteration Processes Associated with Ore-Forming Systems, Geological Association of Canada Short Course Notes, v. 11, p. 339-379.

Mercier-Langevin, P., Lafrance, B., Bécu, V., Dubé, B., Kjarsgaard I., and Guha, J., 2014, The Lemoine Auriferous Volcanogenic Massive Sulfide Deposit, Chibougamau Camp, Abitibi Greenstone Belt, Quebec, Canada. Geology and Genesis. Ecnomic Geology, v. 109, p. 231-269.

Miller, J., and Wilson, C.J.L., 2004, Stress controls on intrusion-related gold lodes: Wonga Gold Mine, Stawel, western Lachlan fold belt, southeastern Australia. Economic Geology, vol. 99, p. 941-963.

Mountain, B.W. and Williams-Jones, E., 1995, Mass transfer and the path of metasomatic reactions in mesothermal gold deposits: an example from Flambeau Lake, Ontario. Economic Geology, v. 91, p. 302-321.

Neumayr, P., Walshe, J., Hagemann, S., Petersen, K., Roache, A., Frikken, P., Horn, L., and Halley, S., 2008, Oxidized and reduced mineral assemblages in greenstone belt rocks of the St. Ives gold camp, Western Australia: vectors to high-grade ore bodies in Archean gold deposits. Mineralium Deposita, v. 43, p. 363-371.

Ohmoto, H, Rye, R.O., 1979, Isotopes of Sulphur and Carbon. *In:* Barnes, H.L, ed., Geochemistry of Hydrothermal Ore Deposits. J Wiley and Sons, New York, p. 509-567.

O'Neil, J.R., and Taylor, H.P. Jr., 1969, Oxygen isotope equilibrium between muscovite and water: Journal of Geophysical Research, v. 74, p. 6012-6022.

Plümper, O., and Putnis, A., 2009, The complex hydrothermal history of granitic rocks: multiple feldspar replacement reactions under subsolidus conditions: Journal of Petrology, v. 50, p. 967-987.

Poulsen, K.H., Robert, F., and Dubé, B., 2000, Geological classification of Canadian gold deposits: Geological Survey of Canada, Bulletin 540, 106 p.

Putnis, A., 2002, Mineral replacement reactions: from macroscopic observations to microscopic mechanisms: Mineralogical Magazine, v. 66, p. 689-708.

Putnis, A. and John, T., 2010, Replacement processes in the Earth's crust. Elements, v. 6, p. 159-164.

Reich M., Kesler S.E., Utsunomiya S., Palenik C S., Chryssoulis S L. and Ewing R. C., 2005, Solubility of gold in arsenian pyrite. Geochimica et Cosmochimica Acta, v. 69, p. 2781–2796.

Reich, M., Deditius, A., Chryssoulis, S., Li, J.W., Ma., C.Q., Parada, M.A., Barra, F., and Mittermayr, F., 2013., Pyrite as a record of hydrothermal fluid evolution in a porphyry copper system: A SIMS/EMPA trace element study. Geochimica et Cosmochimica Acta, v. 104, p. 42-62.

Robert, F., 2001, Syenite-associated disseminated gold deposits in the Abitibi greenstone belt, Canada: Mineralium Deposita, v.36, p. 503-516.

Robert, F., and Poulsen, K.H., 1997, World-class Archean gold deposits in Canada: an overview. Australian Journal of Earth Sciences, v.44, p. 329-351.

Rogers, J.R., Beilhartz, D., Kontak, D.J., Katz, L., Dubé, B., and McNicoll, V., 2013, The Cote Gold deposit: discovery of a new generation low-grade, multi-million ounce gold resource in the Archean Superior Province of Canada [ext. abs.]. NewGenGold Conference, Perth, Australia, 2013, Extended Abstracts, p. 159-174.

Seedorff, E., Barton, M.D., Stavast, W.J.A., and Maher, D.J., 2008, Root zones of porphyry systems: Extending the porphyry model to depth. Economic Geology, v. 103, p. 939-956.

Sheppard, S.M.F., 1986, Characterization and isotopic variations in natural waters. *In:* Valley, J.W., Taylor, H.P., Jr., O'Neil, J.R., eds., Stable Isotopes, High Temperature Geological Processes. Reviews in Mineralogy, v. 16, p.165-183.

Sillitoe, R.H., 2010, Porphyry copper systems. Economic Geology, v. 105, p. 3-41.

Sillitoe, R.H., and Thompson, J.F.H., 1998, Intrusion-related vein gold deposits: types, tectono-magmatic settings and difficulties of distinction from orogenic gold deposits. Resource Geology, v. 48, no. 2, p.237-250.

Sinclair, W.D., Kooiman, G.J. A., Martin, D.A., and Kjarsgaard, I.M., 2007, Geology, geochemistry and mineralogy of indium resources at Mount Pleasant, New Brunswick, Canada. Ore Geology Reviews, v. 28, p. 123-145.

Sinclair, W.D. and Jonasson, R., 2014, Highly siderophile elements (Re, Au, PGE) in porphyry deposits and their mantle origins. Acta Geologica Sinica, v. 88, p. 616-618.

Stephens, J.R., Mair, J.L., Oliver, N.H.S., Hart, C.J.R., and Baker, T., 2004, Structural and mechanical controls on intrusion-related deposits of the Tombstone Gold Belt, Yukon, Canada, with comparisons to other vein-hosted ore-deposit types. Journal of Structural Geology, v. 26, p 1225-1241.

Smith, J., Lafrance, B., and Kontak, D., 2014, A comparative study of the deformation history of auriferous quartz veins in the Archean Côté Gold deposit and the structural evolution of the spatially related Ridout Deformation Zone, Swayze Greenstone Belt, northern Ontario. Abstracts for the Geological Association of Canada-Mineralogical Association of Canada joint annual meeting, Fredericton, New Brunswick, vol. 37, p. 257-258.

Tang, YY, Bi, XW, Fayek, M., Hu, RZ, Wu, LY, Zou, ZC, Feng, CX, Wang, XS, 2014, Microscale sulfur isotopic compositions of sulfide minerals from the Jingding Zn-Pb deposit, Yunnan Province, Southwest China. Gondwana Research, v. 26, p. 594-607.

Taylor, Jr., H.P., 1977, Water/rock interactions and the origin of H_2O in granitic batholiths. Journal of the Geological Society, London, v. 133, p. 509–558

Taylor, H.P., Jr., 1979, Oxygen and hydrogen isotope relationships in hydrothermal mineral deposits. *In:* Geochemistry of Hydrothermal Ore Deposits, 2nd ed., H.L. Barnes, ed., John Wiley and Sons, New York, p. 236-277.

Taylor, H.P. Jr., 1978, Oxygen and hydrogen isotope studies of plutonic granitic rocks. *In:* Trace Elements in Igneous Petrology – A Volume in Memory of Paul W. Gast, Earth and Planetary Science Letters, v. 38, p. 177-210.

Thompson, J.H.F., Sillitoe, R.H., Baker, T., Lang, J.R., and Mortensen, J.K., 1999, Intrusion-related gold deposits associated with tungsten-tin provinces. Mineralium Deposita, v. 34, p. 323-334.

Thomson, J.E., Charlewood, G.H., Griffin, K., Hawley, J.E., Hopkins, H., MacIntosh, C.G., Ogryzlo, S.P., Perry, O.S., and Ward, W., 1950, Geology of the main ore zone at Kirkland Lake. Ontario Department of Mines Annual Report, v. 57, p. 54-188.

Tosdal, R.M., and J.P. Richards, 2001, Magmatic and structural controls on the development of porphyry Cu±Mo±Au deposits. Reviews in Economic Geology, v.14, p.157-181.

Valley, J.W., Chiarenzelli, J.R., and McLellan, J.M., 1994, Oxygen isotope geochemistry of zircon. Earth and Planetary Science Letters, v. 126, p. 187-206.

van Breeman, O., Heather, K.B., and Ayer, J.A., 2006, U-Pb geochronology of the Neoarchean Swayze sector of the southern Abitibi greenstone belt. Geological Survey of Canada, Current Research 2006-Fl, 32 p.

Walshe, J.L., Halley, S.W., Hall, G.A., and Kitto, P., 2003, Contrasting fluid systems, chemical gradients and controls on large-tonnage high-grade Au deposits, Eastern Goldfields province, Yilgarn craton, Western Australia. *In:* Eliopoulos D.G., et al., eds, Mineral exploration and sustainable development: Rotterdam, Millpress, p. 827-830.

Wang, L.G., Qui, Y.M., McNaughton, N.J., Groves, D.I., Luo, Z.K. Huang, J.Z. Miao, L.C., and Liu, Y.K., 1998, Constraints on crustal evolution and gold metallogeny in the Northwestern Jiaodong Peninsula, China, from SHRIMP U-Pb zircon studies of granitoids. Ore Geology Reviews vol. 13, p. 275-292.

Werle, J.L., Ikramuddin, M., and Mutschler, F.E., 1983, Allard stock, La Plata Mountains, Colorado – an alkaline rock-hosted porphyry copper – precious metal deposit. Canadian Journal of Earth Science, v. 21, p. 630-641.

Whalen, J.B., Percival, J.A., McNicoll, V.J., and Longstaffe, F.J., 2002, A mainly crustal origin for tonalitic granitoid rocks, Superior Province, Canada. Journal of Petrology, v.43, p. 1551-1570.

Zheng, Y.F., 1993, Calculation of oxygen isotope fractionation in anhydrous silicate minerals. Geochimica et Cosmochimica Acta, v. 57, p. 1079-1091.

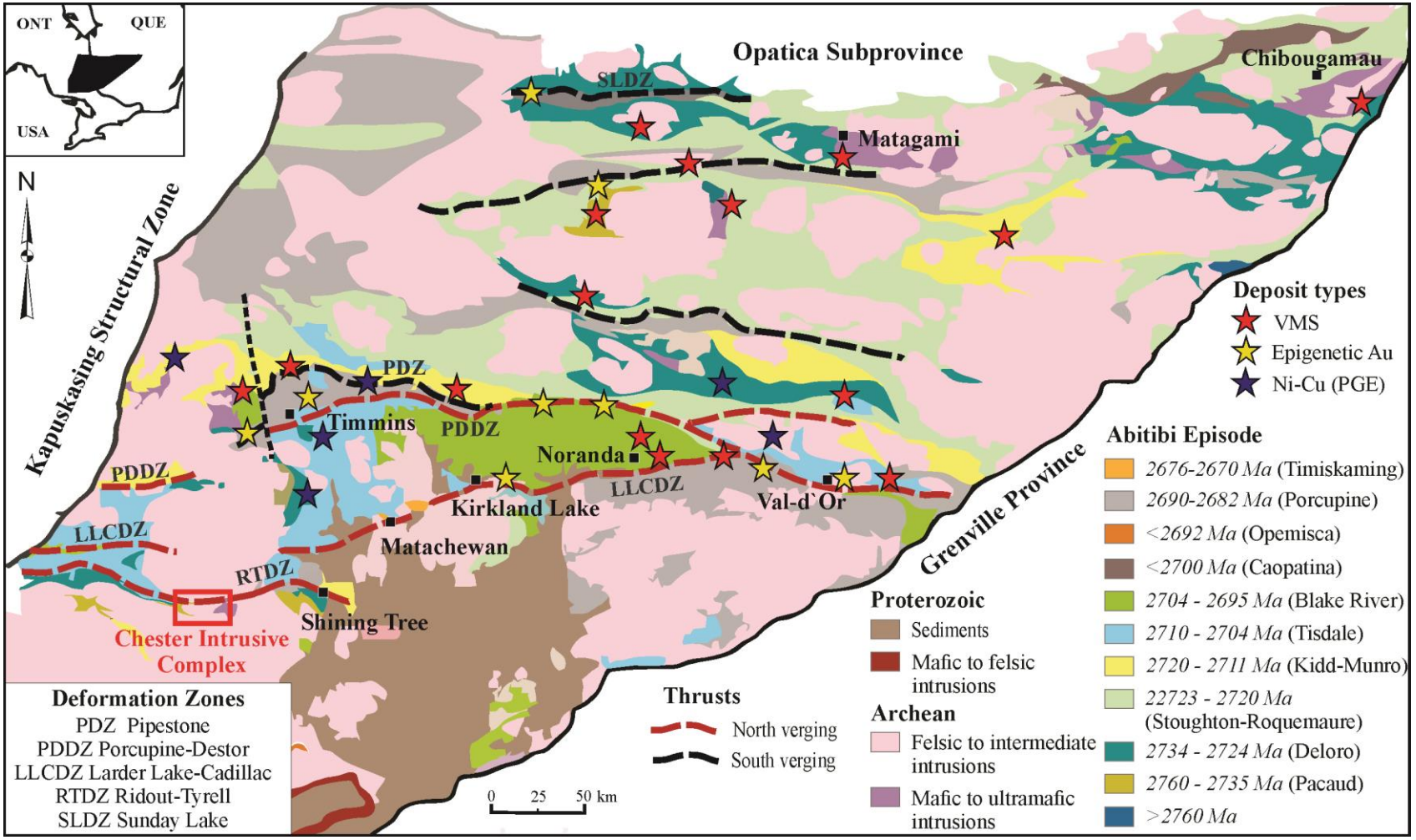

Figure 1: Geological map of the Abitibi Subprovince showing the location of study Chester Intrusive complex and important types of mineral deposits including gold (modified after Ayer 2013).

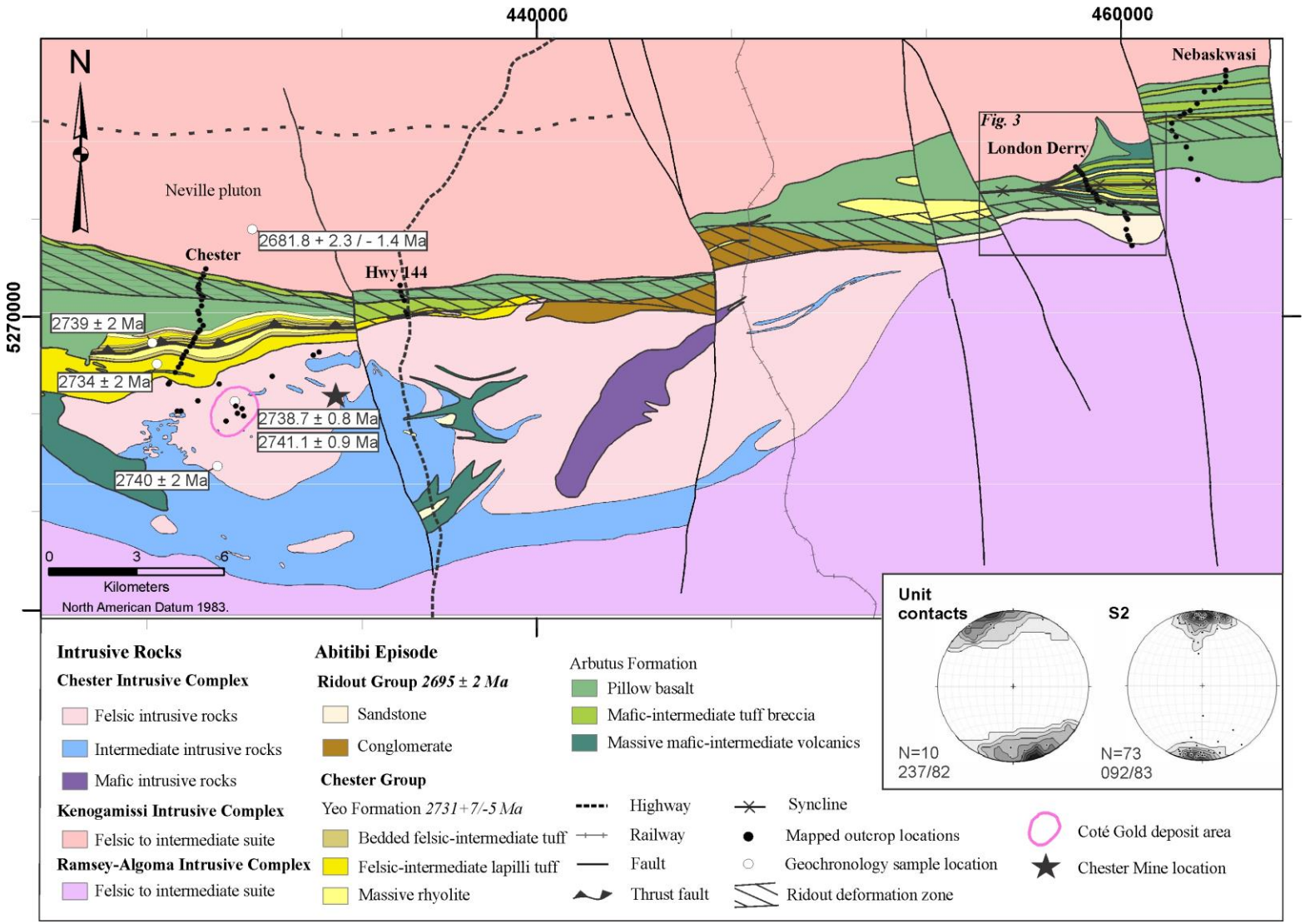
440000
460000
5270000
N
Neville pluton
Chester
Hwy 144
Nebaskwasi
Fig. 3
London Derry
2681.8 + 2.3 / - 1.4 Ma
2739 ± 2 Ma
2734 ± 2 Ma
2738.7 ± 0.8 Ma
2741.1 ± 0.9 Ma
2740 ± 2 Ma
0 3 6
Kilometers
North American Datum 1983.
Unit contacts
N=10
237/82
S2
N=73
092/83
Intrusive Rocks
Chester Intrusive Complex
Felsic intrusive rocks
Intermediate intrusive rocks
Mafic intrusive rocks
Kenogamissi Intrusive Complex
Felsic to intermediate suite
Ramsey-Algoma Intrusive Complex
Felsic to intermediate suite
Abitibi Episode
Ridout Group 2695 ± 2 Ma
Sandstone
Conglomerate
Chester Group
Yeo Formation 2731+7/-5 Ma
Bedded felsic-intermediate tuff
Felsic-intermediate lapilli tuff
Massive rhyolite
Arbutus Formation
Pillow basalt
Mafic-intermediate tuff breccia
Massive mafic-intermediate volcanics
Highway
Railway
Fault
Thrust fault
Syncline
Mapped outcrop locations
Geochronology sample location
Ridout deformation zone
Coté Gold deposit area
Chester Mine location

Figure 2: Simplified bedrock and structural geology map of the study area within the southeastern Swayze greenstone belt (modified after Ayer and Chartrand (2011) and Berger (2011)). The four completed mapping transects discussed in the text are labelled by road from west to east (a) Chester, (b) 144, (c) London Derry, and (d) Nebaskwasi. Geochronology results by van Breeman et al. (2006) are shown. Also included are equal area, lower hemisphere projections of the unit contacts and dominant foliation, S_2, occuring throughout each transect (composite foliation S_{2-3} used for the Chester transect). Number of measurements (N) and contours in multiples of 8.

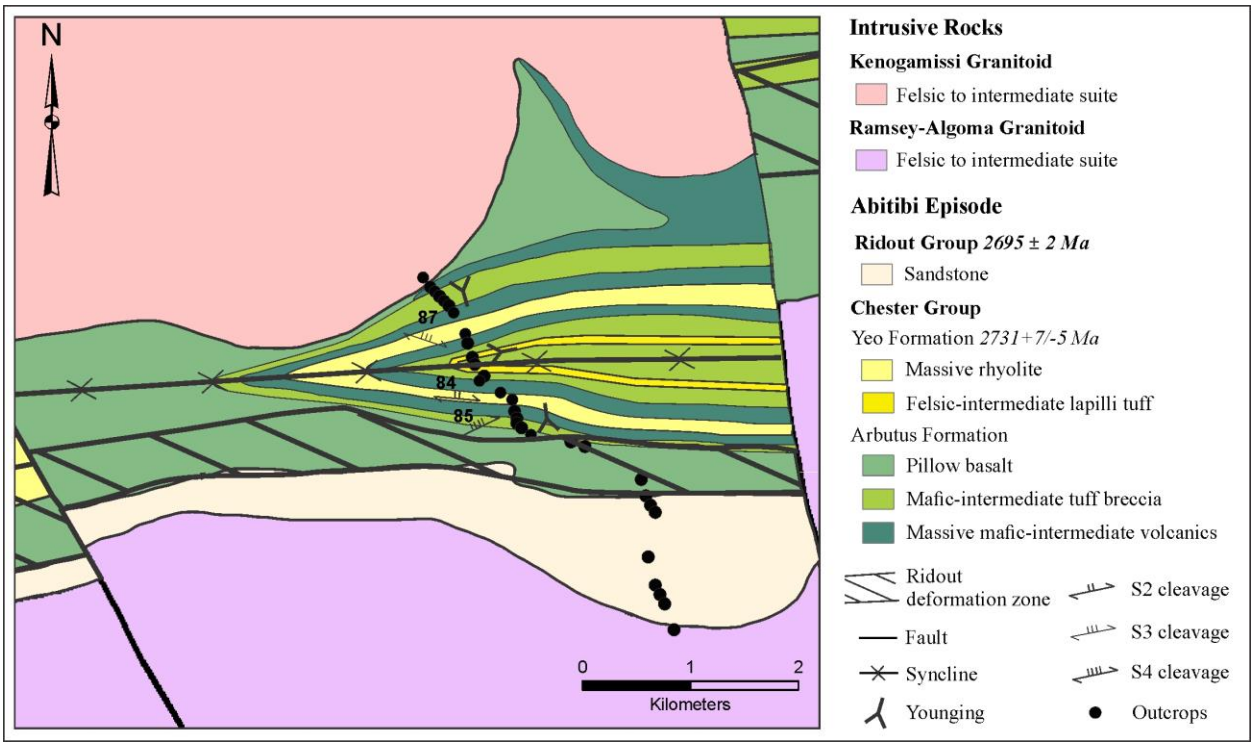

Figure 3: Simplified geological map of the London Derry transect; see Figure 2 for its location. Note that dike rocks have been omitted for clarity. The location of the regional F_2 axial plane shown reflects the changes in younging direction as indicated by the symbols.

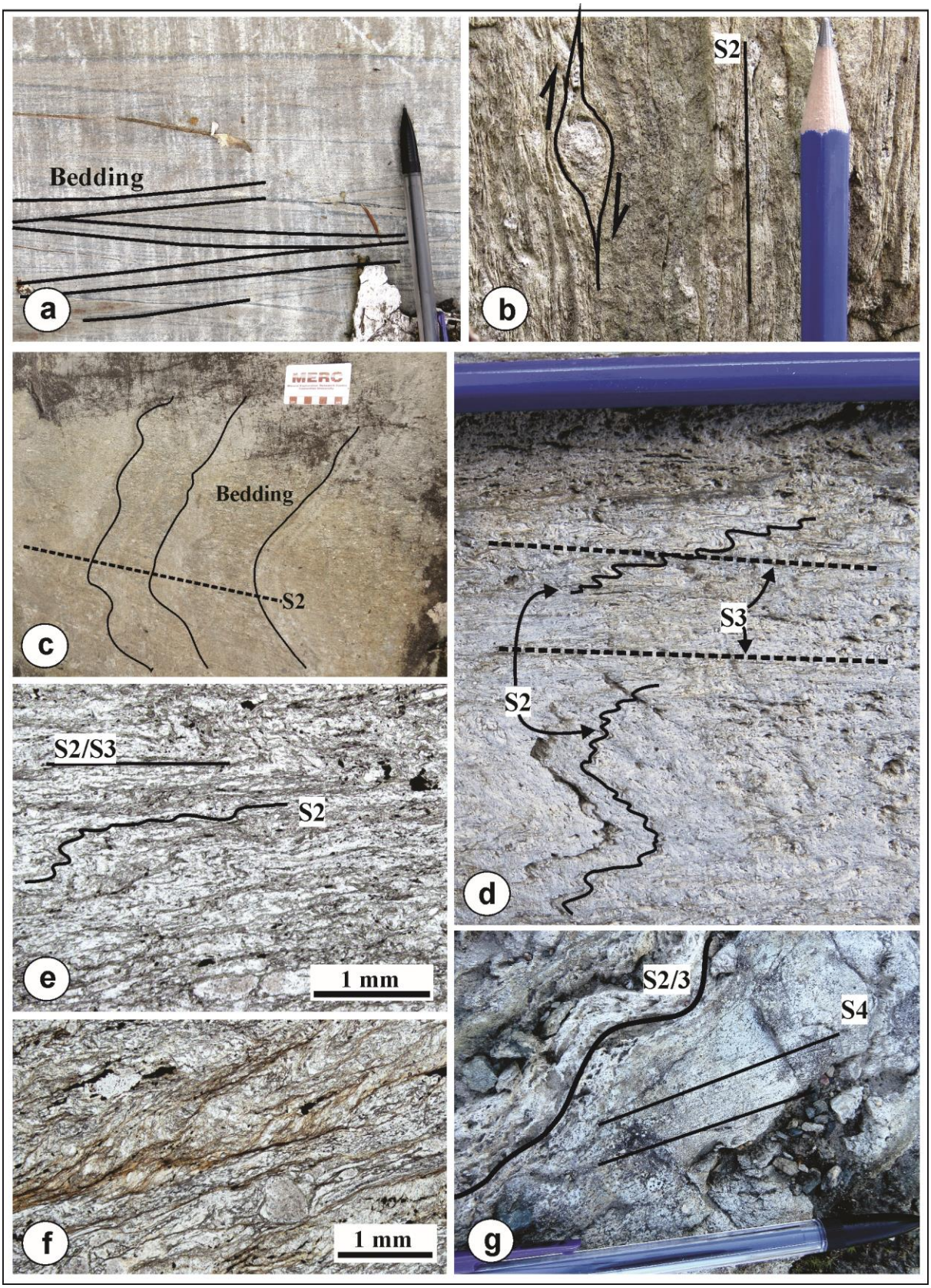
Bedding
a
S2
b
Bedding
S2
c
S3
S2
d
S2/S3
S2
e
1 mm
f
1 mm
S2/3
S4
g

Figure 4: Outcrop and thin section photographs which summarize the structural features of the Chester transect. Note that in all images the north direction is to the top of the page unless otherwise noted. (a) Truncation of bedding in a bedded tuff which indicates a north-younging direction of the stratigraphy. (b) Vertical face in an outcrop of a feldspar porphyry unit showing a strain shadow around feldspar gain which indicates north-side up movement. North direction is to the left. (c) Outcrop of a mafic bedded tuff showing the regional nose of F_a folding bedding with an axial planar cleavage, S_a. Lighter areas are coarser grained, darker are finer. Note that the S_2 fabric is perpendicular to bedding. (d) Outcrop of a mafic tuff breccia showing that S_2 is tightly crenulated and S-folded which results in the formation of an axial planar cleavage, S_3. (e) Petrographic image in plane light of an oriented sample showing an initial fabric, S_2, being tightly crenulated and transposed into a secondary composite fabric, S_{2-3}. (f) Petrographic image in plane polarized light of an oriented sample of volcanic tuff showing spaced S_{2-3} cleavage domains defined by sericite anastomosing around phenocrysts. (g) The limb of an F4 fold which is outlined by the folding of S_{2-3} fabrics with an axial planar cleavage S_4, as seen in pillow basalt.

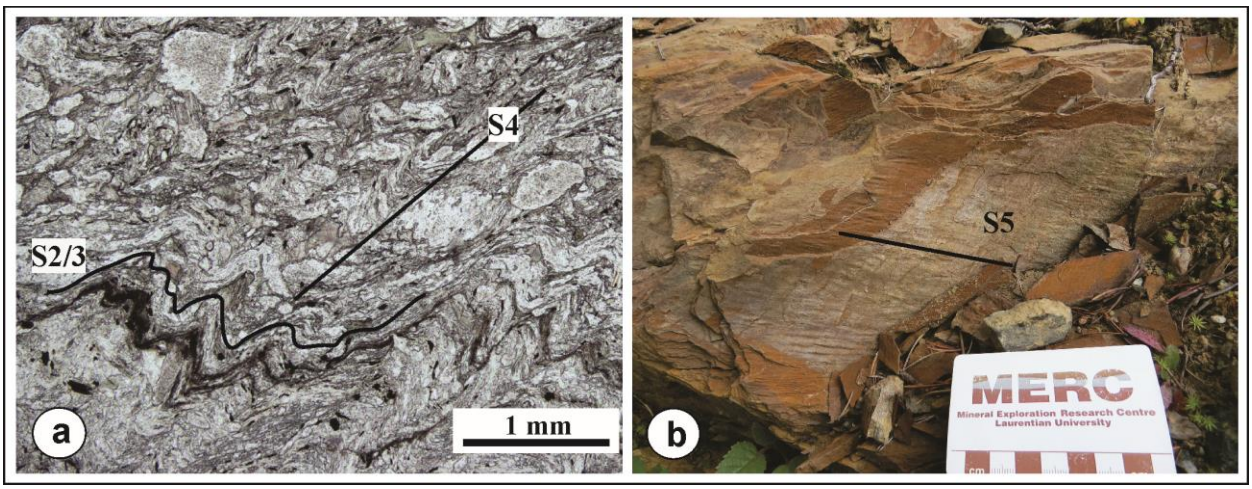

Figure 5: Structural features of the London Derry transect. Note that the north direction is to the top of the page. (a) Petrographic image in plane polarized light of tuff breccia showing the S_{2-3} fabrics being strongly Z-folded and the development of an axial planar cleavage S_3. (b) Outcrop of an intensley deformed mafic volcanic unit showing the development of a shallow-dipping crinkle lineation along S_2 cleavage

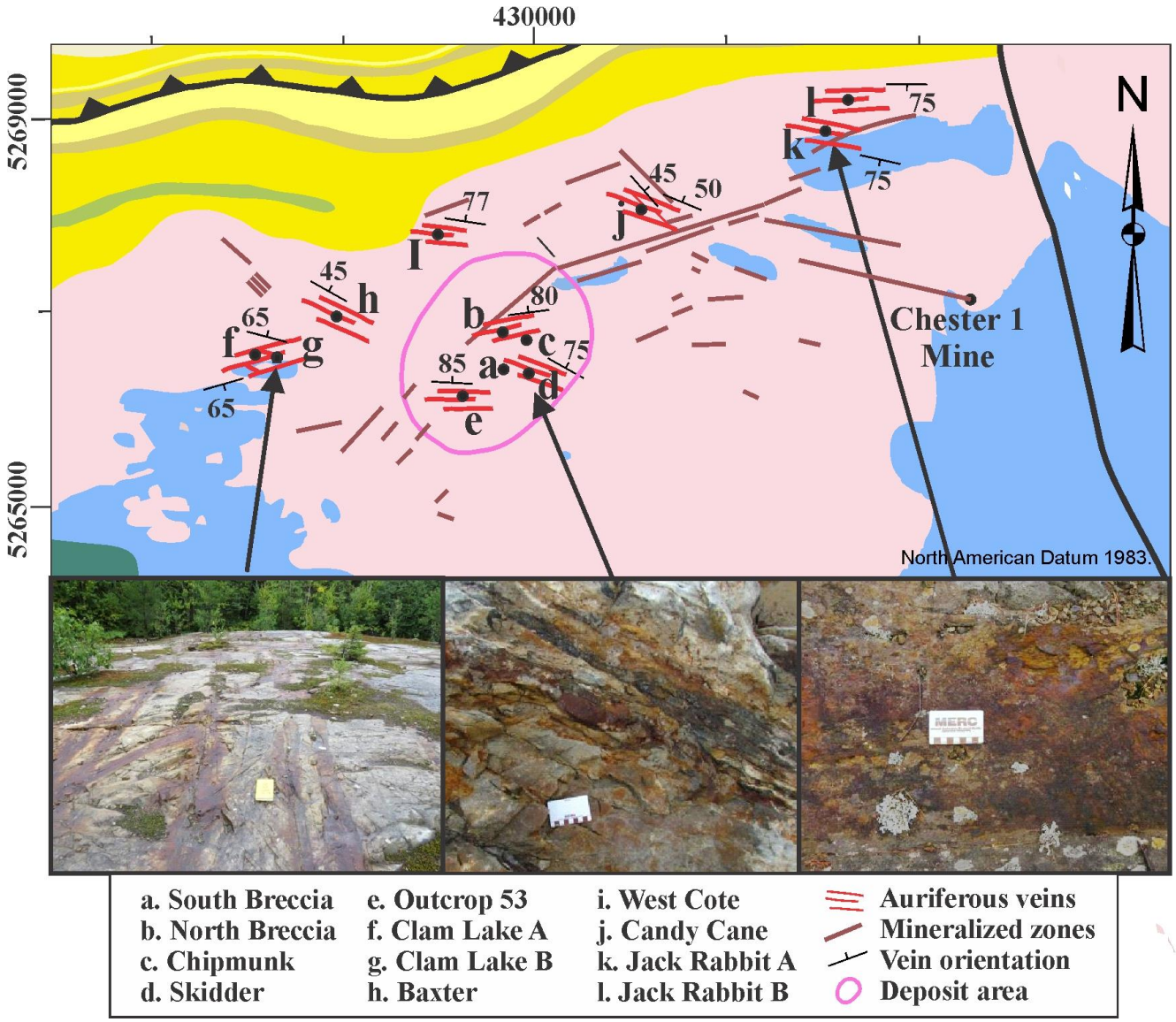

Figure 6: Geological map of the area around the Côté Gold deposit (ore envelope in dark pink) showing the locations of outcrops mapped in detail and also where the former Chester 1 mine is located. The general orientations of mineralized veins mapped in this study are shown in red. In the lower part are outcrop photographs of quartz-sulfide veins (from left to right: Clam Lake B, Skidder, Jack Rabbit A) which are shown in order to demonstrate the simiarity in their appearance and the presence of a sericite-pyirte alteration halo. In photos north is to the top of the page, except for Clam Lake B, which was taken looking east.

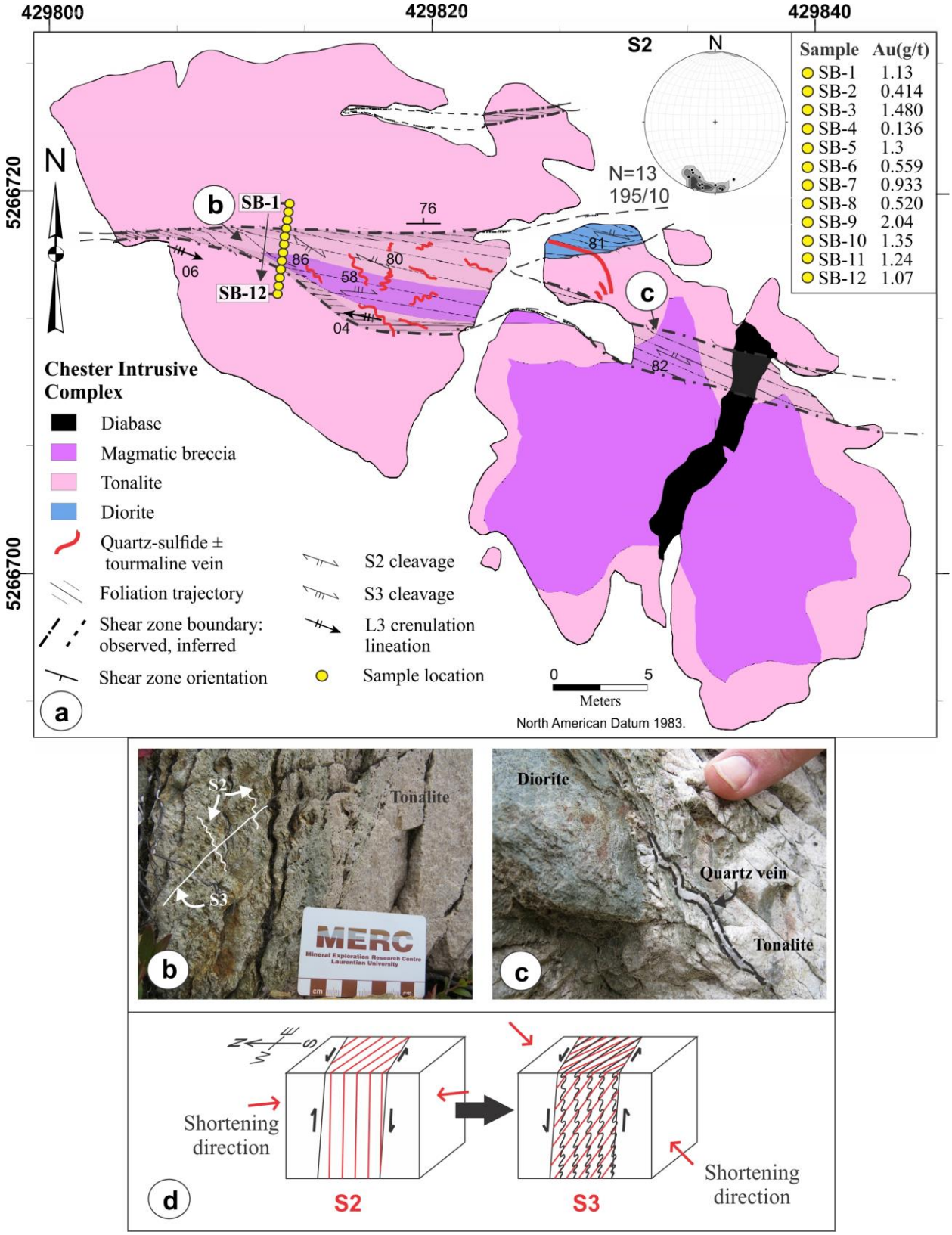
429800
429820
429840
5266720
5266700
N
S2
N
N=13
195/10
Sample Au(g/t)
SB-1 1.13
SB-2 0.414
SB-3 1.480
SB-4 0.136
SB-5 1.3
SB-6 0.559
SB-7 0.933
SB-8 0.520
SB-9 2.04
SB-10 1.35
SB-11 1.24
SB-12 1.07
b
SB-1
SB-12
76
06
86
80
58
04
81
c
82
Chester Intrusive Complex
Diabase
Magmatic breccia
Tonalite
Diorite
Quartz-sulfide ± tourmaline vein
Foliation trajectory
Shear zone boundary: observed, inferred
Shear zone orientation
S2 cleavage
S3 cleavage
L3 crenulation lineation
Sample location
a
0
5
Meters
North American Datum 1983.
S2
S3
Tonalite
b
MERC
Mineral Exploration Research Centre
Laurentian University
Diorite
Quartz vein
Tonalite
c
Shortening direction
S2
S3
Shortening direction
d

Figure 7: (a) Simplified geological map of South Breccia outcrop showing structural features and Au assay results. An equal area, lower hemisphere projection of the data for the S_2 fabric is shown as an inset with the number of measurements (N) and contours in multiples of 6. The accompanying outcrrop photographs show important structural features; note that north direction is to the top of the page unless otherwise noted. (b) Vertical cross section of the shear zone looking east showing tightly crenulated S_2 with S_3 crenulation cleavage indicating reversal of slip within the shear zone. (c) Quartz vein in tonalite which shows an increasing amount of shear as one approaches the shear zone which is localized to the contact between the tonalite and diorite. (d)A block diagram showing the formation of S_2 and S_3 fabrics at the South Breccia outcrop. The red arrows indicate the necessary shortening direction required to form these fabrics. The direction of shear is shown for each generation (D_2 and D_3).

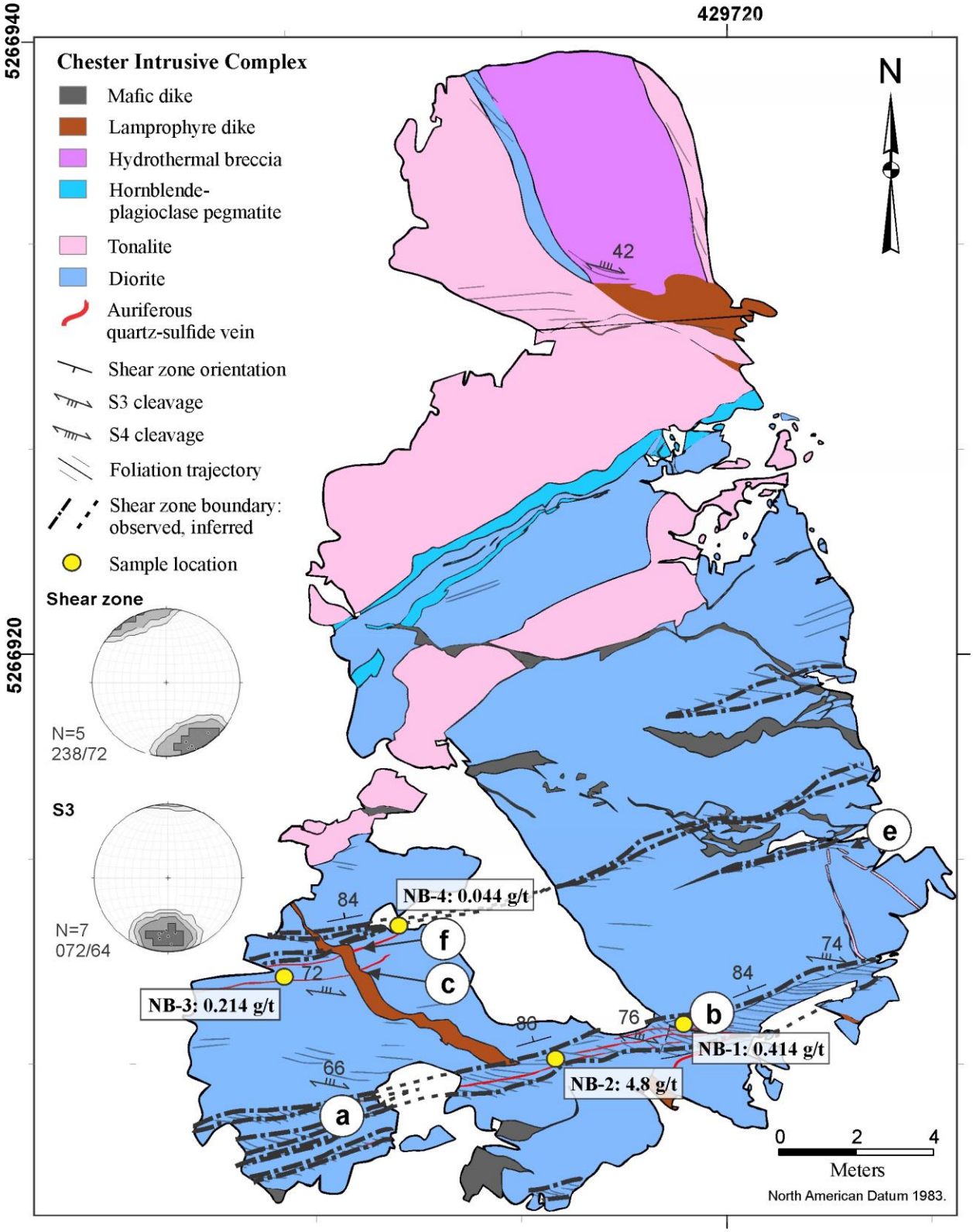
Chester Intrusive Complex
Mafic dike
Lamprophyre dike
Hydrothermal breccia
Hornblende-plagioclase pegmatite
Tonalite
Diorite
Auriferous quartz-sulfide vein
Shear zone orientation
S3 cleavage
S4 cleavage
Foliation trajectory
Shear zone boundary: observed, inferred
Sample location
Shear zone
N=5
238/72
S3
N=7
072/64
N
429720
5266940
5266920
42
84
72
66
86
76
84
74
NB-4: 0.044 g/t
NB-3: 0.214 g/t
NB-2: 4.8 g/t
NB-1: 0.414 g/t
a
b
c
e
f
0 2 4
Meters
North American Datum 1983.

Figure 8: Simplified geology map of the North Breccia outcrop (modified after Katz 2016). The results of Au assay results for four distinct mineralized veins are shown with two of these from within the main shear zone and two outside. Locations of photographs a-f are shown (refer to Fig. 9). Two equal area, lower hemisphere projection stereonets are shown as insets to demonstrate the orientation of the shear zone and the S_3 fabric with the number of measurements (N) and contours in multiples of 5.

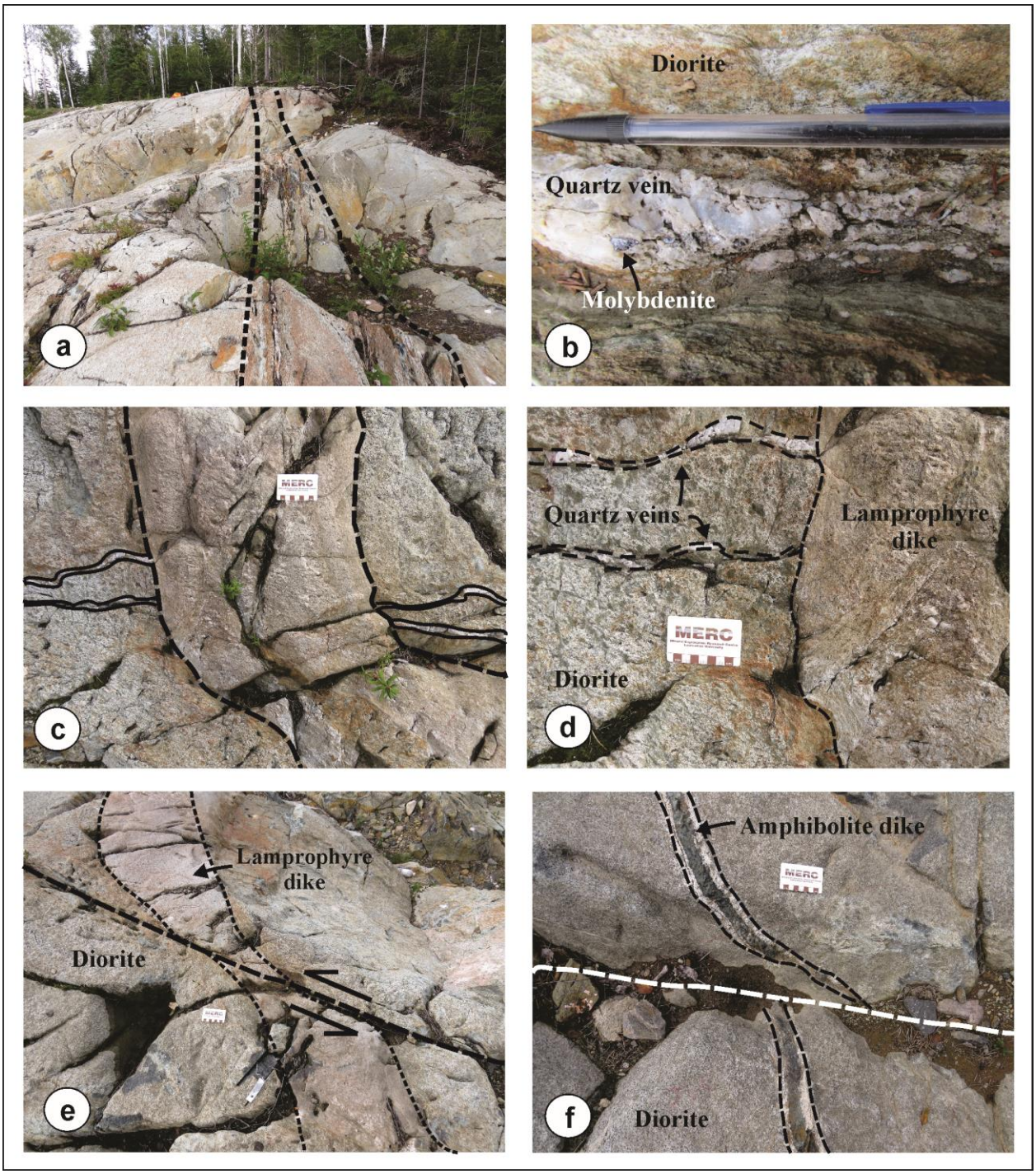

Figure 9: Photographs of structural and cross-cutting features observed at the North Breccia outcrop; note that the features are outlined in black. The north direction is to the top of the page unless otherwise noted. (a) The major east-west trending shear zone located at the south of the outcrop which is host to visible auriferous quartz veins (looking east). (b)

Close up of an auriferous quartz vein within the shear zone, as seen in the previous image, with molybdenite present at the surface. (c) Lamprophyre dike that cross cuts a pair of east-west trending auriferous quartz veins. (d) Close-up of the previous image showing the truncation of auriferous quartz veins at the margin of the lamprophyre dike. (e) Lamprophyre dike showing a sinistral offset and drag folding in the shear zone. (f) Amphibolite veins with plagioclase alteration haloes showing evidence of early sinistral drag folding along the shear zone with a later brittle reactivation having dextral offset.

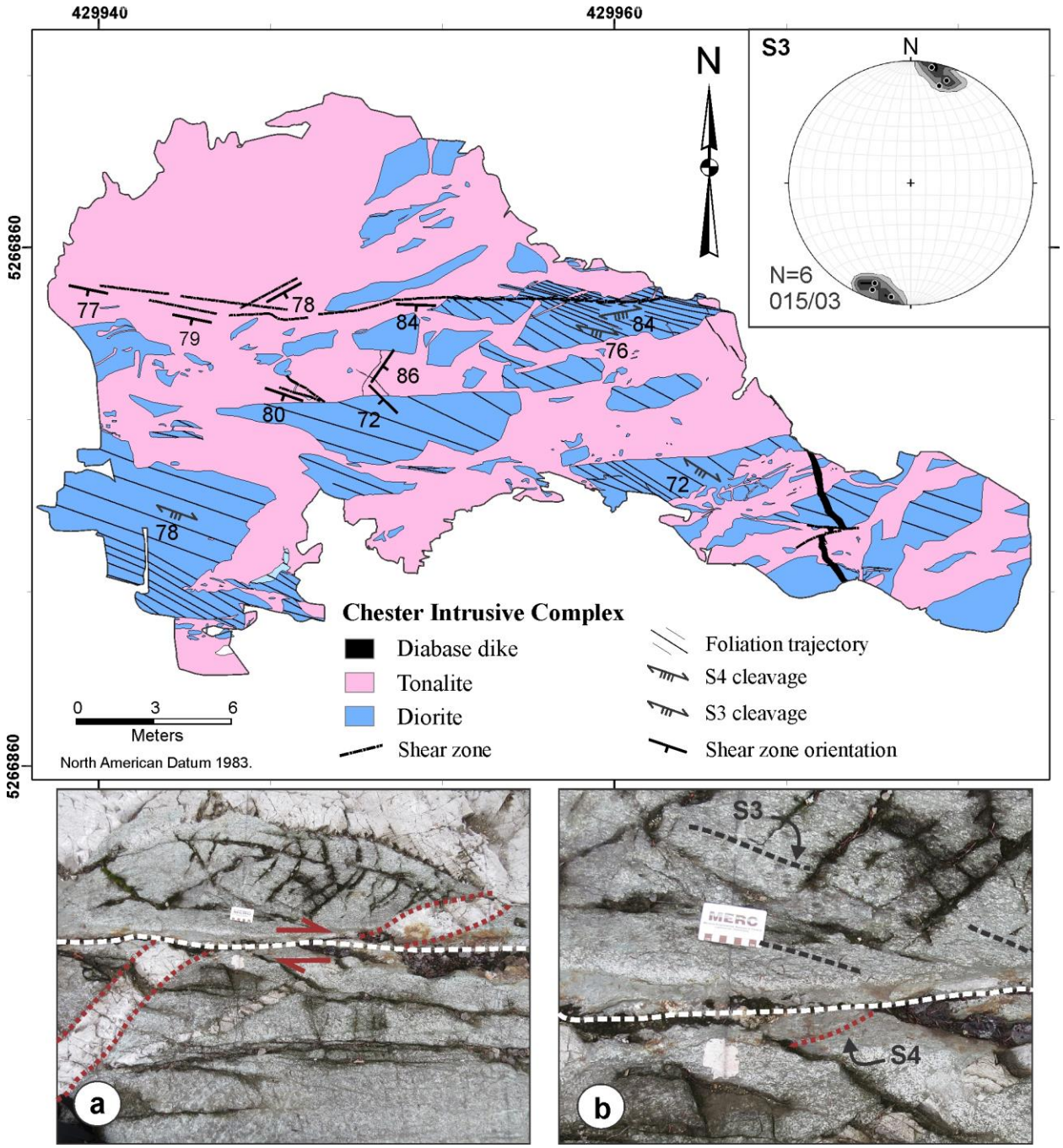

Figure 10: (a) Simplified geology map of the Chipmunk outcrop along with images showing structural features. North direction is to the top of the page. Inset shows an equal area, lower hemisphere projection of data for S_3 fabric with number of measurements (N) and contours in multiples of 3. (b) Photograph showing the dextral displacement of a tonalite dike along an east-west oriented shear zone (dashed white line) in a diorite. (c) Photograph showing the S_3 foliation which is pervassively developed within the diorite unit of the outcrop. Note tha the S3 fabric is overprinted by a localized S_4 cleavage that is oriented anticlockwise to the shear zone.

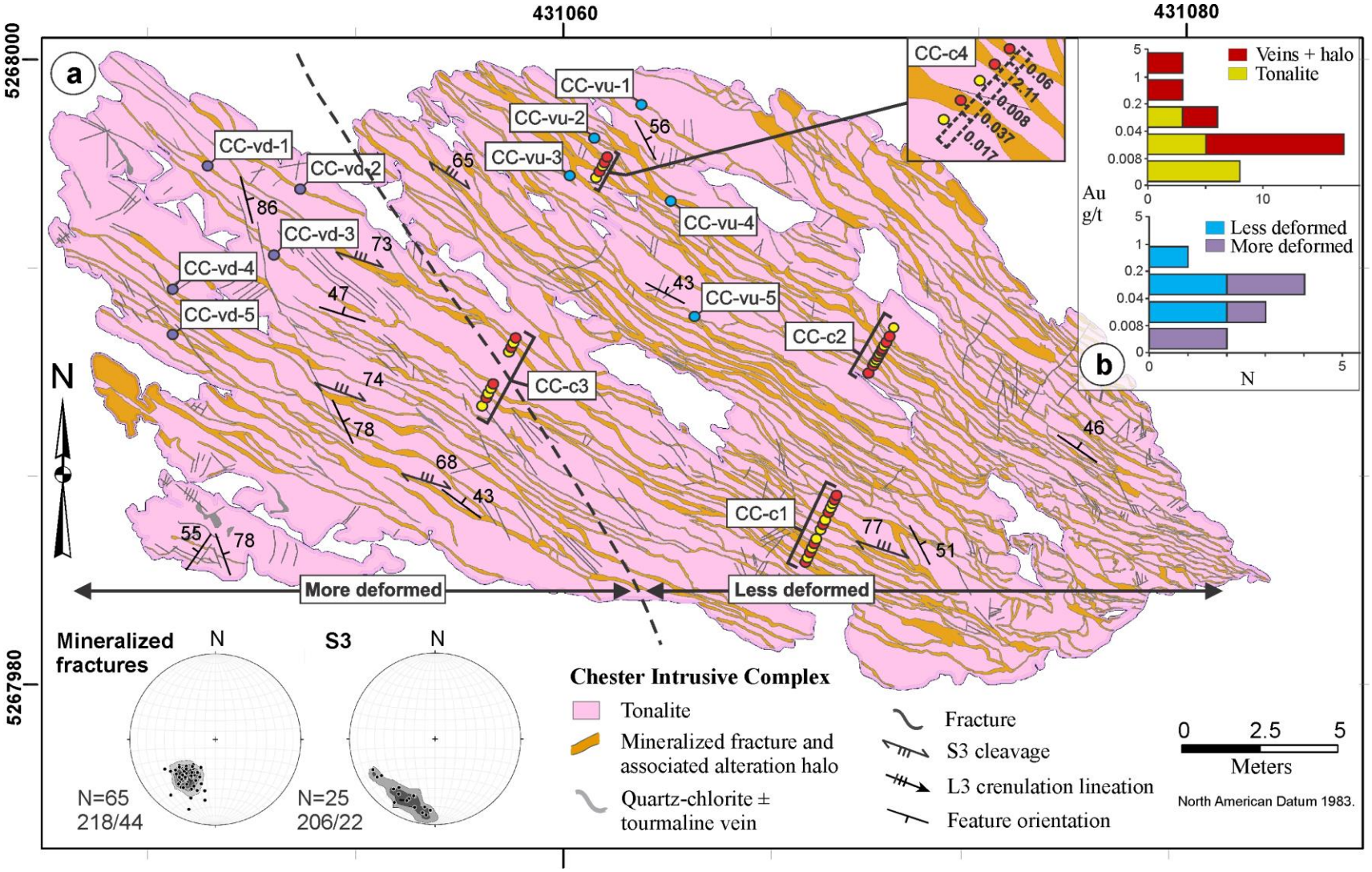
431060
431080
5268000
5267980
a
b
CC-vd-1
CC-vd-2
CC-vd-3
CC-vd-4
CC-vd-5
CC-vu-1
CC-vu-2
CC-vu-3
CC-vu-4
CC-vu-5
CC-c1
CC-c2
CC-c3
CC-c4
86
65
56
73
47
43
74
78
68
43
55
78
77
51
46
10.06
12.11
10.008
10.037
10.017
N
More deformed
Less deformed
Au g/t
Veins + halo
Tonalite
Less deformed
More deformed
Mineralized fractures
S3
N=65
218/44
N=25
206/22
Chester Intrusive Complex
Tonalite
Mineralized fracture and associated alteration halo
Quartz-chlorite ± tourmaline vein
Fracture
S3 cleavage
L3 crenulation lineation
Feature orientation
0 2.5 5
Meters
North American Datum 1983.

Figure 11: (a) Simplified geology map of the Candy Cane outcrop. Insets are equal area, lower hemisphere projections for the sheeted mineralized fractures and overprinting S3 fabric with the number of measurements (N) and contours in multiples of 8 indicated. The locations of samples coded for Au assay are also shown on the map along with an inset histogram (b) summarizing the results. The data are also provided in Table 1.

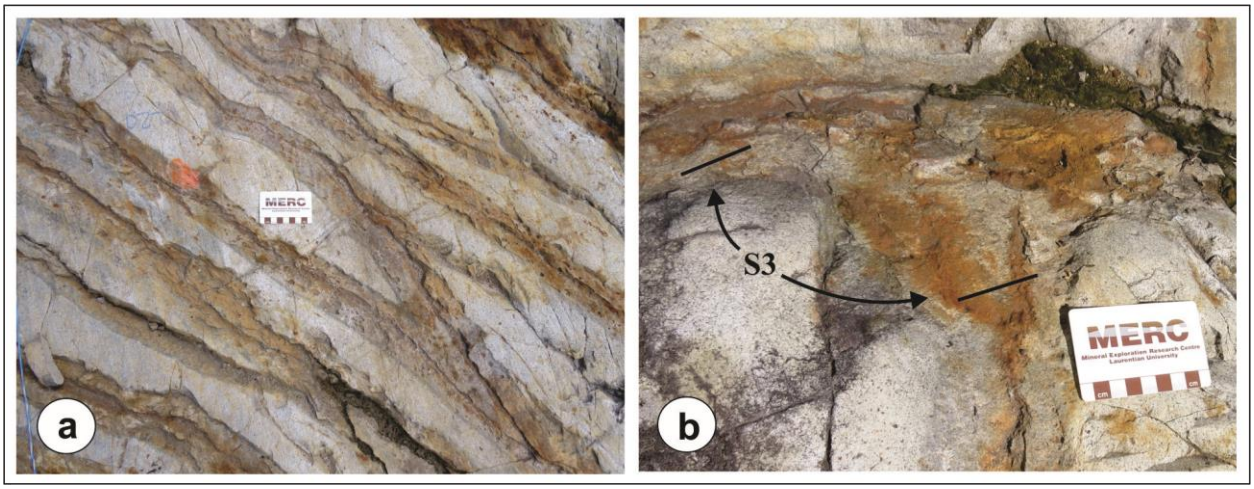

Figure 12: Outcrop photographs showing the important features at the Candy Cane outcrop. North direction is to the top of the page. (a) Sheeted mineralized fractures with a strong sericite-pyrite alteration halo that have a main orientation of 300/55° and a secondary orientation of 325/45° (b) Photograph showing the S_3 foliation developed in the alteration halo. Note that the orientation of the S3 fabric remains consistent regardless of the change in direction of the mineralized fracture.

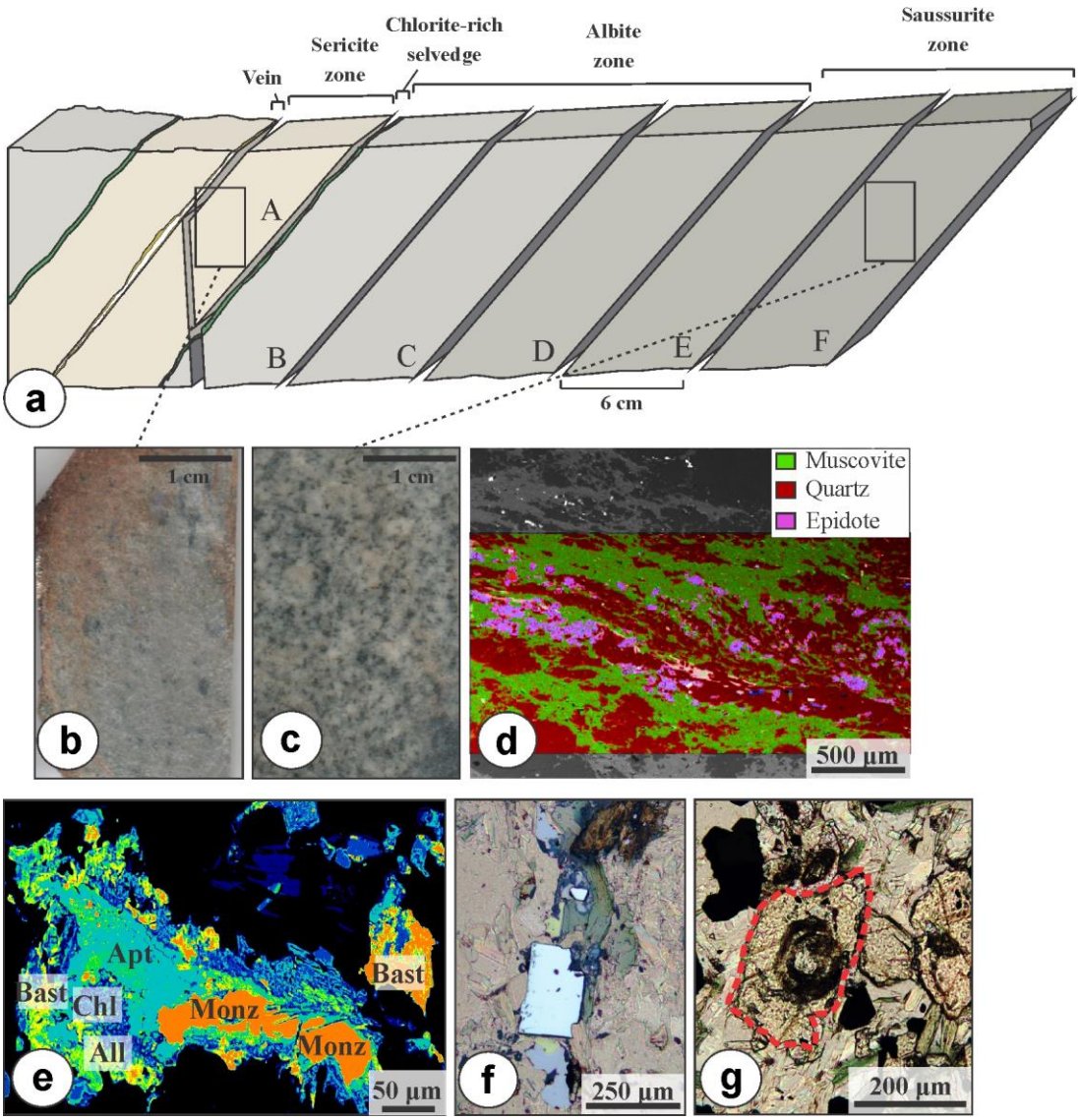

Figure 13: (a) A summary diagram of the auriferous sample with the zoned alteration profile that was collected from the Candy Cane outcrop for geochemical study. Also shown in the diagram are locations of samples (CC-A to CC-F) analyzed for geochemistry. (b, c) Photographs of cut slabs of domains A (b) and F (c). The samples show the strong sericitic alteration which modified the tonalite texturally and mineralogically which created a bleached appearance in domain A compared to the least altered tonalite in domain F which is furthest from the vein. (d) A false-colour X-ray map produced from the SEM-EDS which shows coarse-grained epidote, muscovite and quartz at the center of a mineralized fracture at the core of the alteration profile. (e) A false-colored BSE image from the SEM-EDS showing intergrowth of apatite (Apt) and monazite (Monz) altered and overgrown by chlorite (Chl) and the LREE rich phases allanite (All) and bastnaesite (Bast) within domain A. (f) A photomicrograph of a sample from the core of the alteration profile in combined plane polarized and reflected light which shows pyrite (Py) pyrrhotite (Po) and chalcopyrite (Cpy) associated with chlorite (Chl) and ilmenite (Ilm). (g) Photomicrograph showing an area in the core of the alteration profile with LREE-rich allanite (outlined in red) overgrown by epidote.

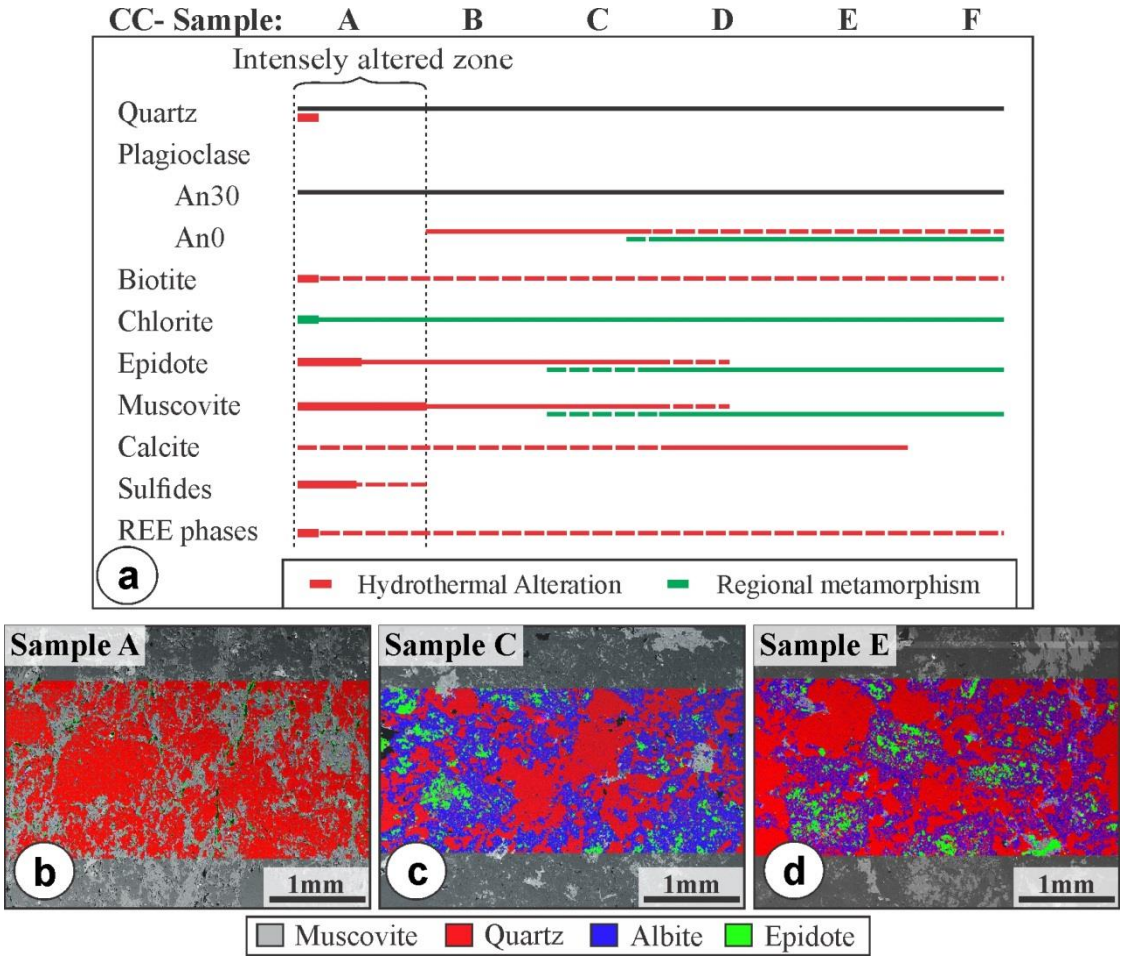

Figure 14: (a) A summary of the mineral phases present and their distribution in the slabbed samples (domains A to F) shown in Figure 13, as based on petrographic study and SEM-EDS observations. The relative timing of phases are indicated by the lines: original mineralogy (black), hydrothermal alteration minerals (red), and regional metamorphic minerals (green). (b, c, d) False-colored X-ray maps showing the change in textures and mineralogy across the profile: (b) Sample CC-A showing complete loss in texture due to albite being altered to sericite plus generation of fine-grained quartz; (c) Sample CC-C showing partial loss of texture with some dissolution recrystallization of quartz, albitization of plagioclase and some coarse-grained hydrothermal epidote; (d) Least altered sample having preserved primary textures with saussuritization of plagioclase resulting in fine-grained muscovite and epidote in its core areas.

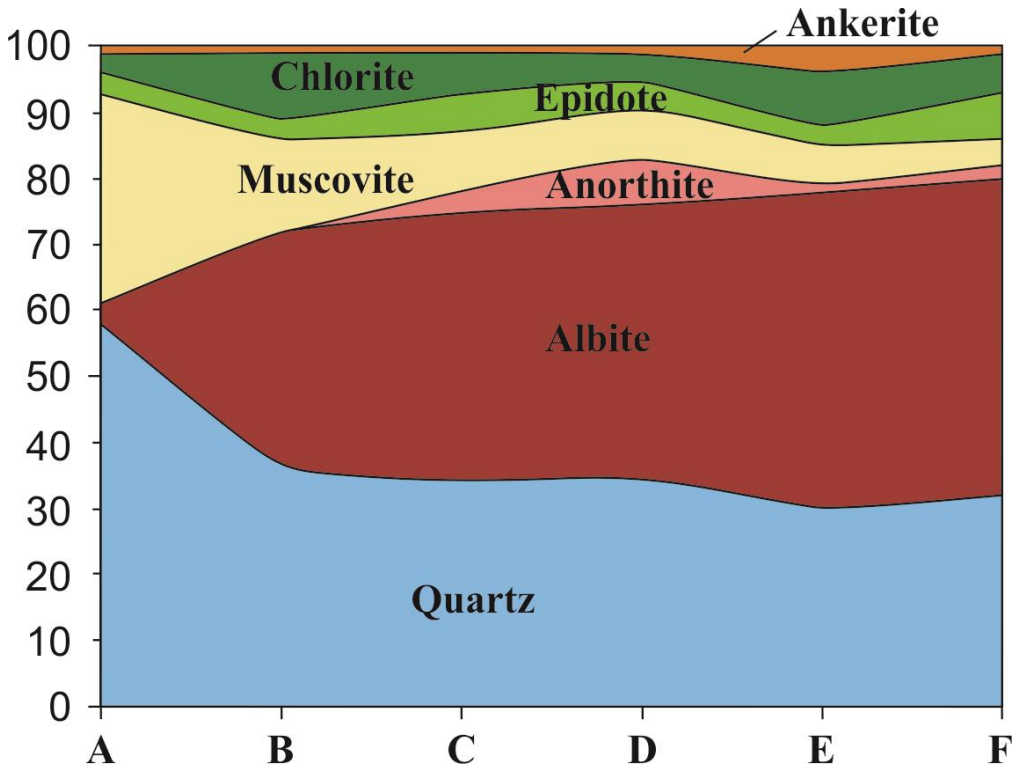

Figure 15: A summary of the change in the modal mineralogy across the alteration profile sampled at the Candy Cane outcrop (samples CC-F to CC-A) as determined using Rietveld analysis. Note that the anorthite refers to the calcic plagioclase (An_{30}) present in the samples.

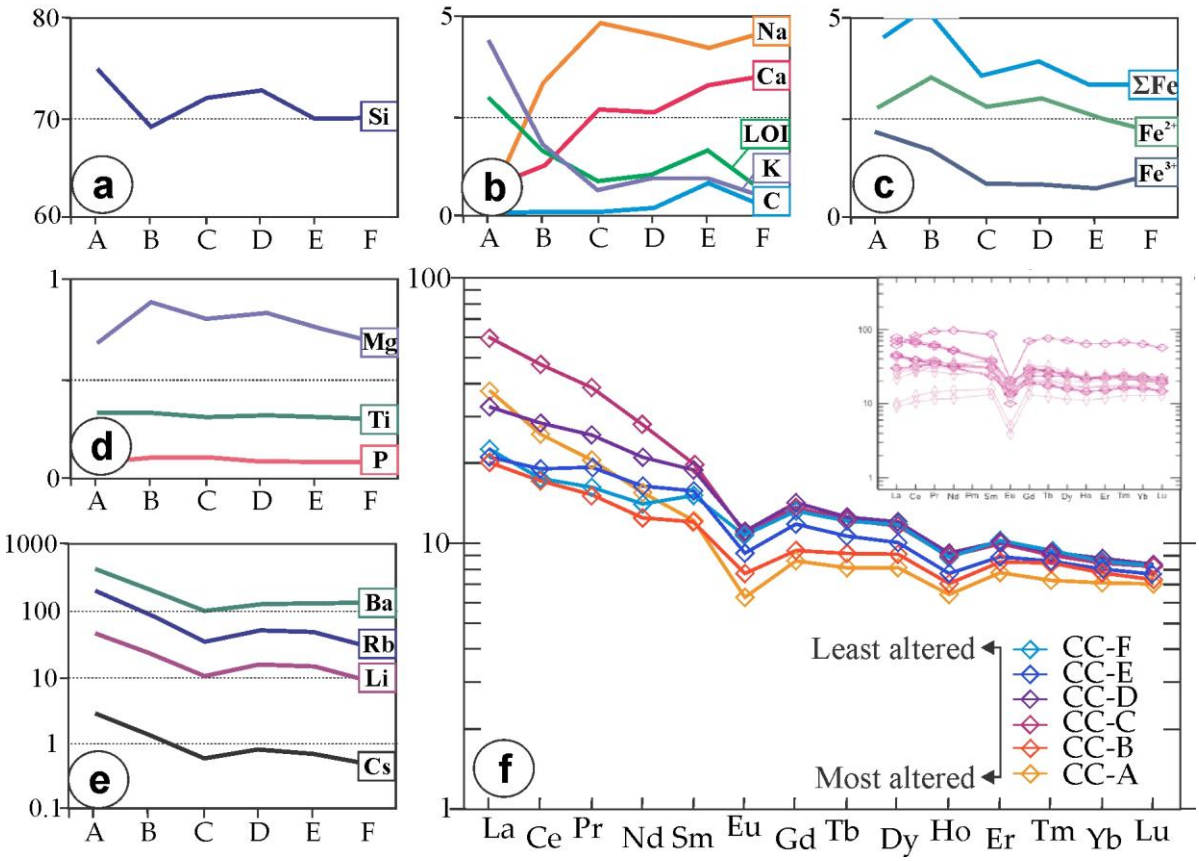

Figure 16: Graphical representations of the changes in weight percent (y axis) of major (as oxides; Fig. 16a, b, c, d) and trace (labelled by cation; Fig. 16e) elements across the alteration profile from CC-A (vein margin) to CC-F (least altered). Note that for the trace elements a log scale is used. The rare earth elements (REE) are shown in a chondrite normalized plot (Fig. 16f) using normalizing values provided by Laul (1979); the inset shows REE data for tonalites from the deposit area (from Katz et al., 2016). Note that in Figure 16b C=CO_2.

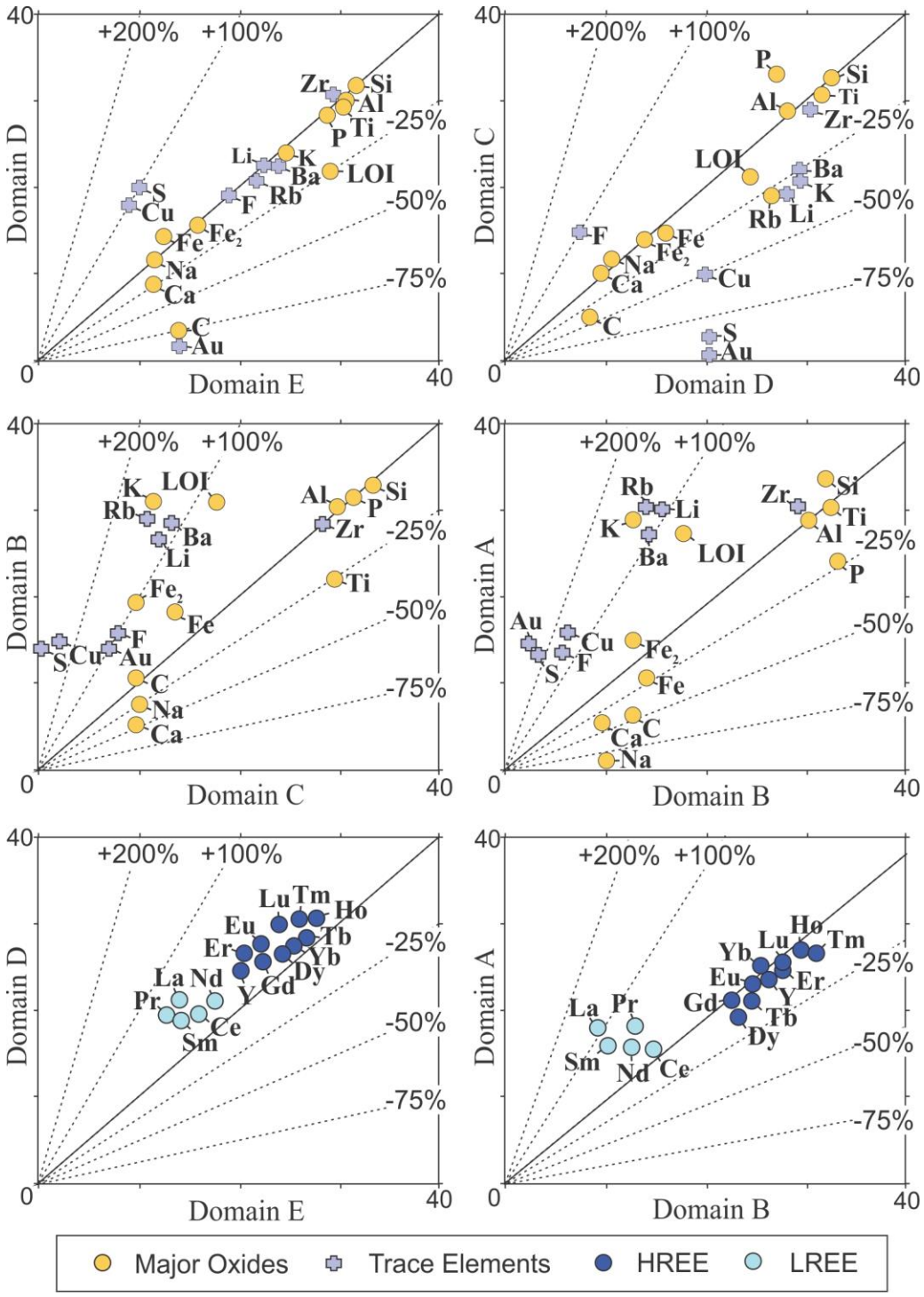

Figure 17: Grant-type isocon plots showing sequential comparisons of elemental changes across the alteration profile for samples from the Candy Cane outcrop (domain E (least altered) to domain A (most altered)). Although Al was used as the immobile element in these plots to define the isocon, note that in most cases Ti, Zr and Si also fall on this line. In these plots the elements falling on or near the isocon line (solid black) represent conserved

concentrations (i.e., no net change), whereas dashed lines show elemental gains/losses as indicated by the numbers. Note that the oxides are labeled by their cation.

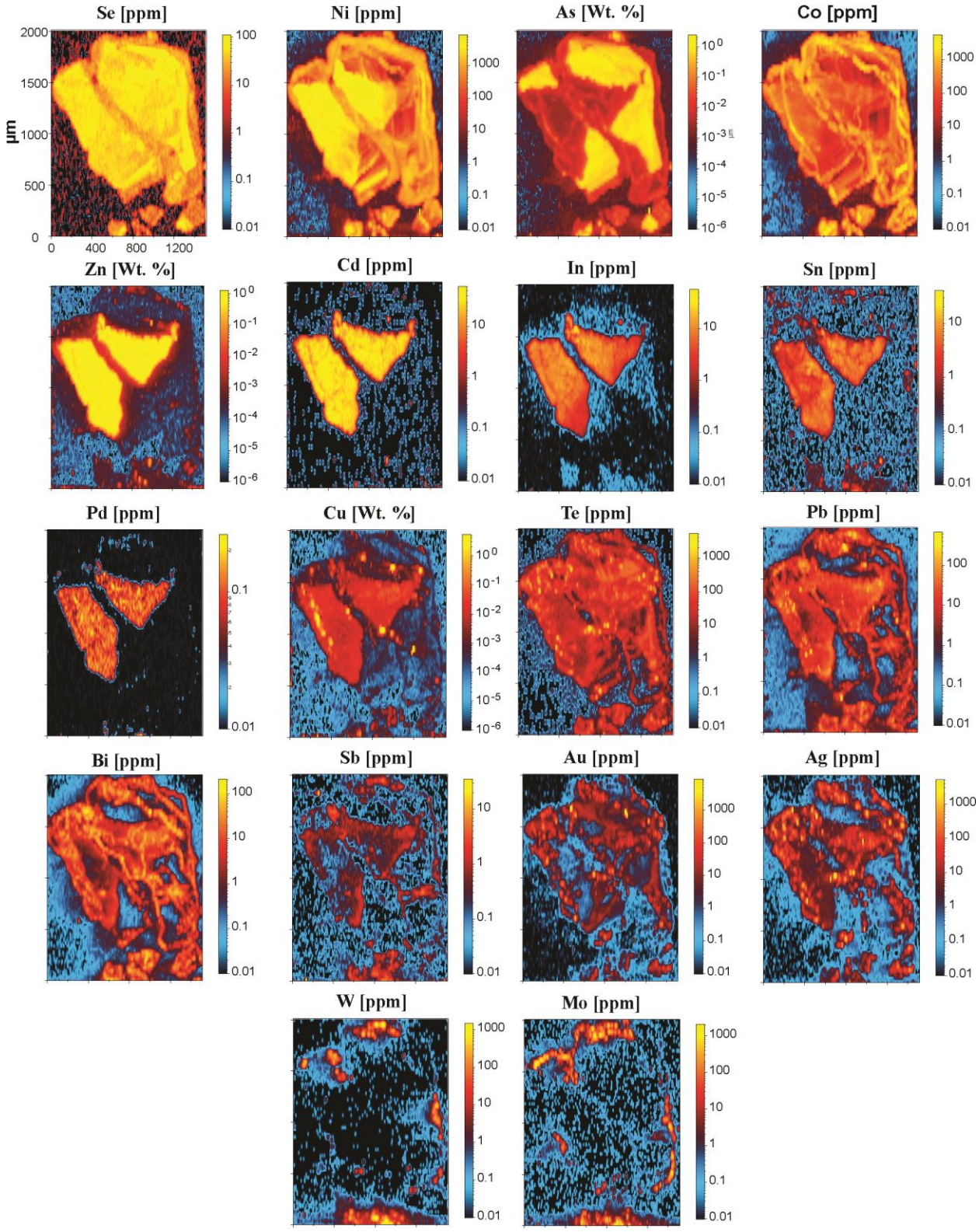
Se [ppm]
Ni [ppm]
As [Wt. %]
Co [ppm]
Zn [Wt. %]
Cd [ppm]
In [ppm]
Sn [ppm]
Pd [ppm]
Cu [Wt. %]
Te [ppm]
Pb [ppm]
Bi [ppm]
Sb [ppm]
Au [ppm]
Ag [ppm]
W [ppm]
Mo [ppm]
µm
0
500
1000
1500
2000
0
400
800
1200

Figure 18: False colour elemental maps for pyrite grain 1 in a mineralized vein (sample JS13- 46A) from the Candy Cane outcrop. Concentrations are plotted using a logarithmic scale. Grain dimensions are in µm and shown in the first image (upper left) only.

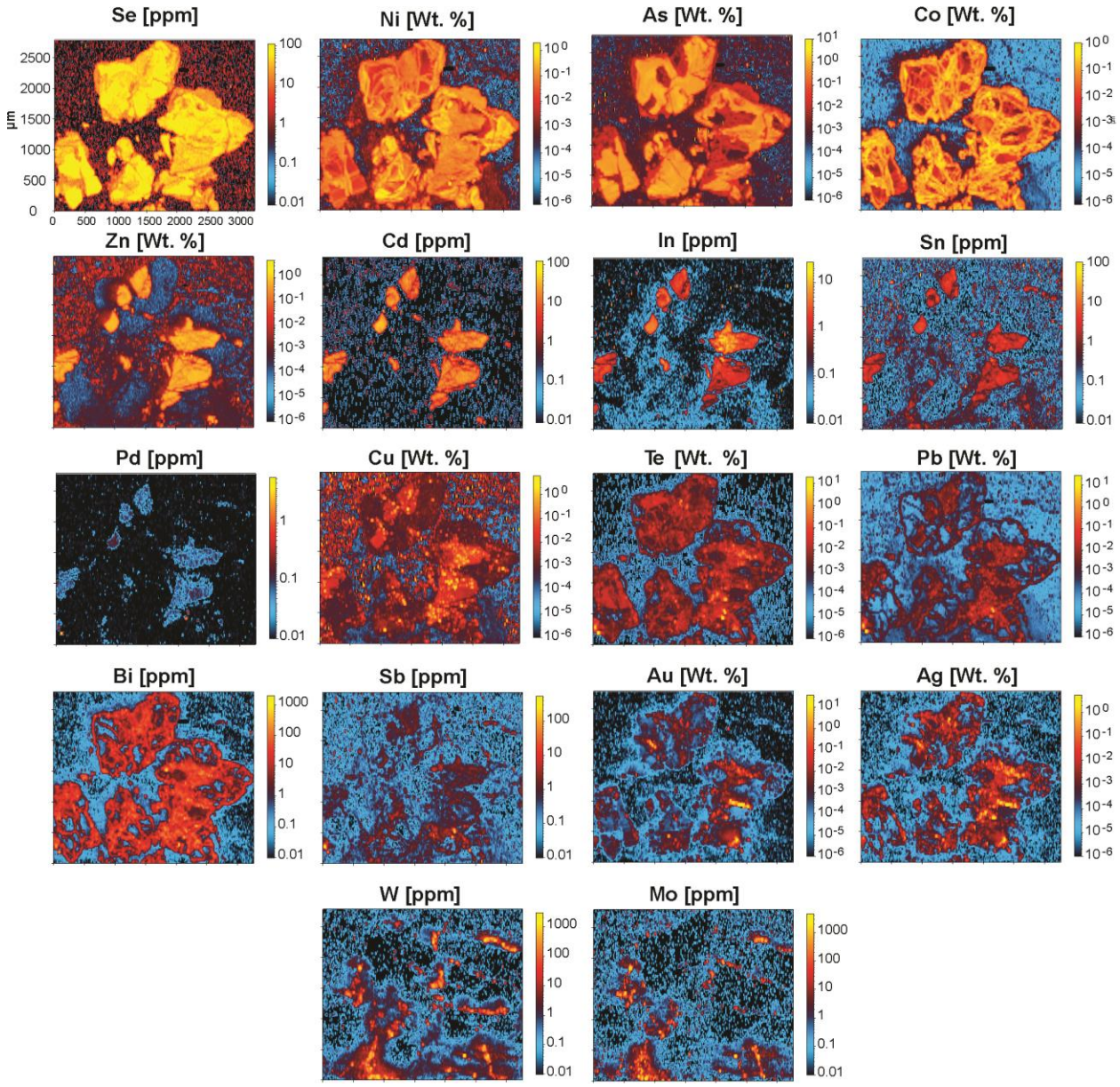

Figure 19: False colour elemental maps for pyrite grain 2 in a mineralized vein (sample JS13- 46A) from the Candy Cane outcrop. Concentrations are plotted using a logarithmic scale. Grain dimensions are in µm and shown in the first image (upper left) only.

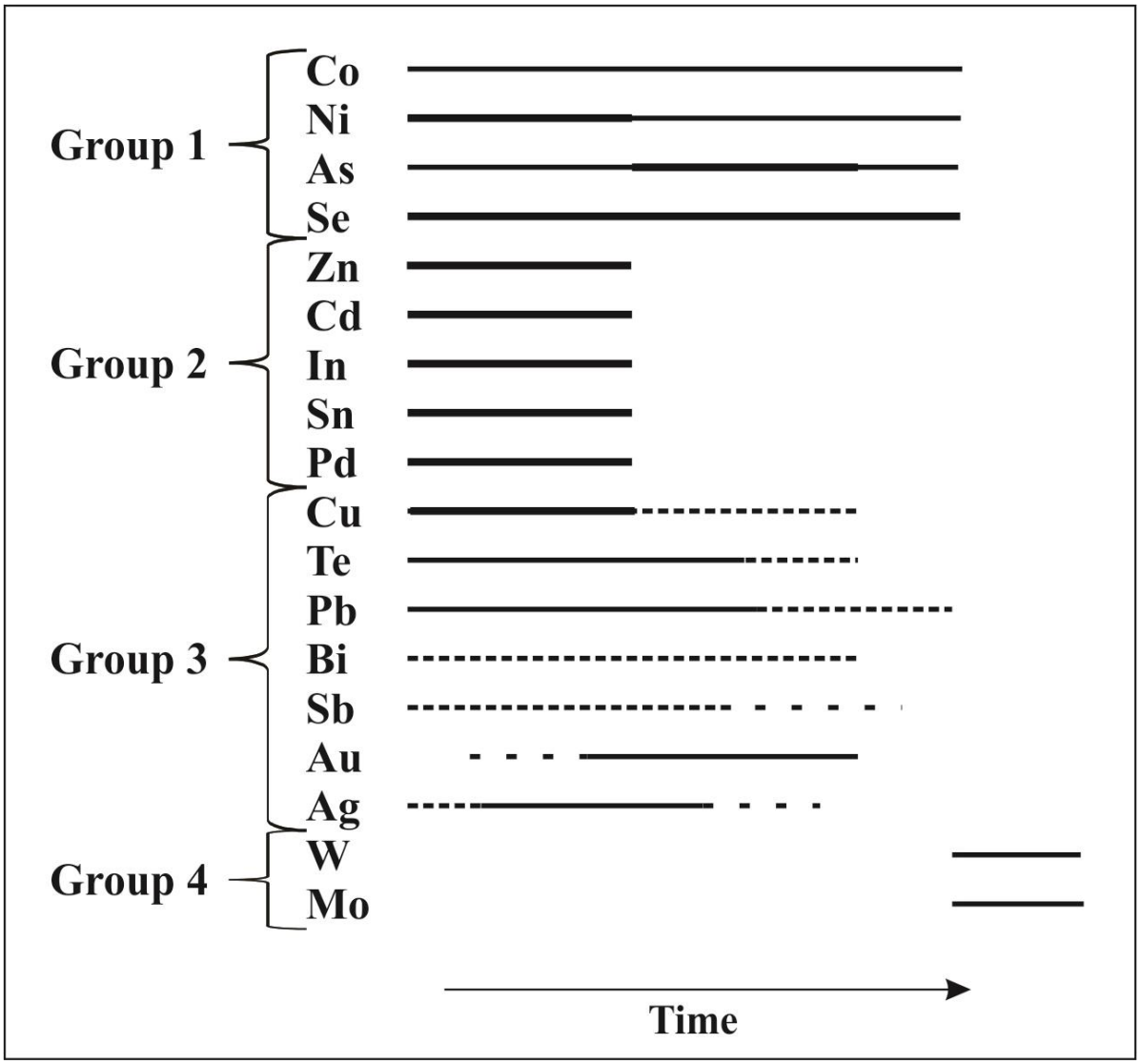

Figure 20: Schematic representation of the inferred elemental paragenesis in pyrite grains 1 and 2 based on LA ICP-MS data and element maps (Figs. 18 and 19).Elements are grouped by relative distribution within the pyrite grains. See text for discussion.

Group 1:

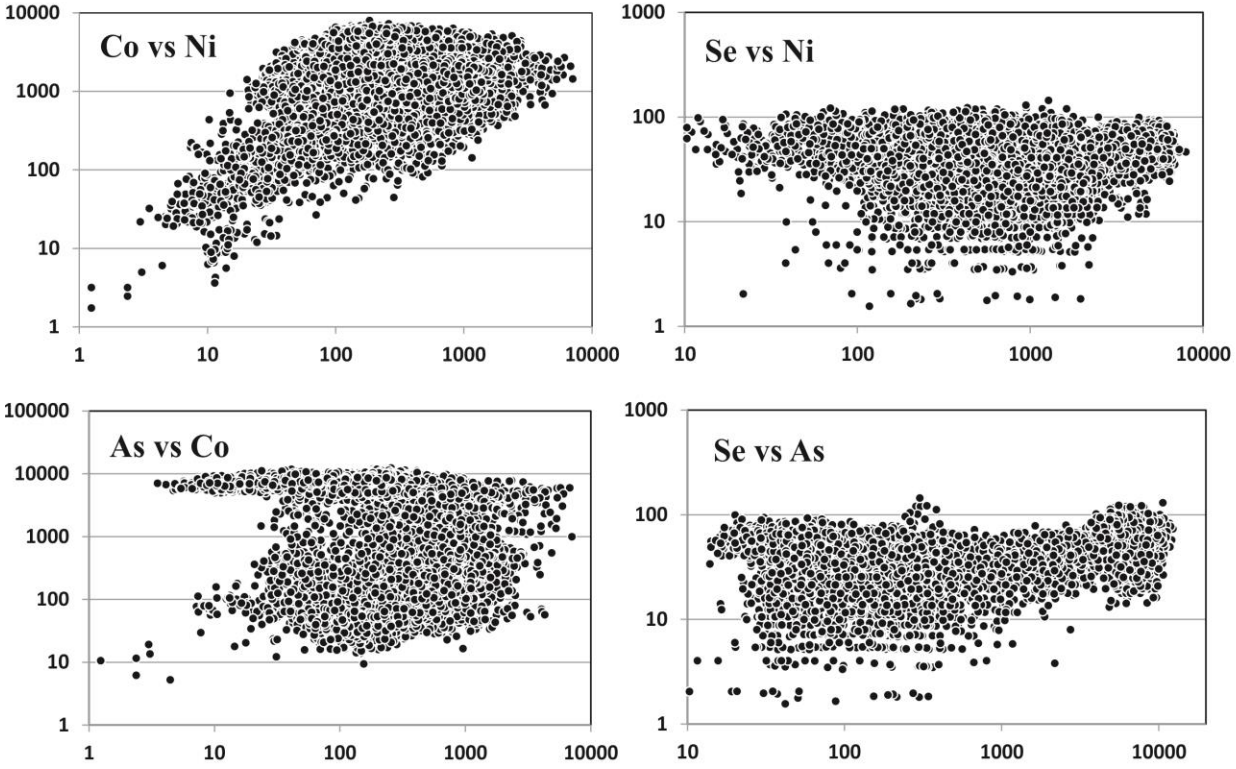

Group 2:

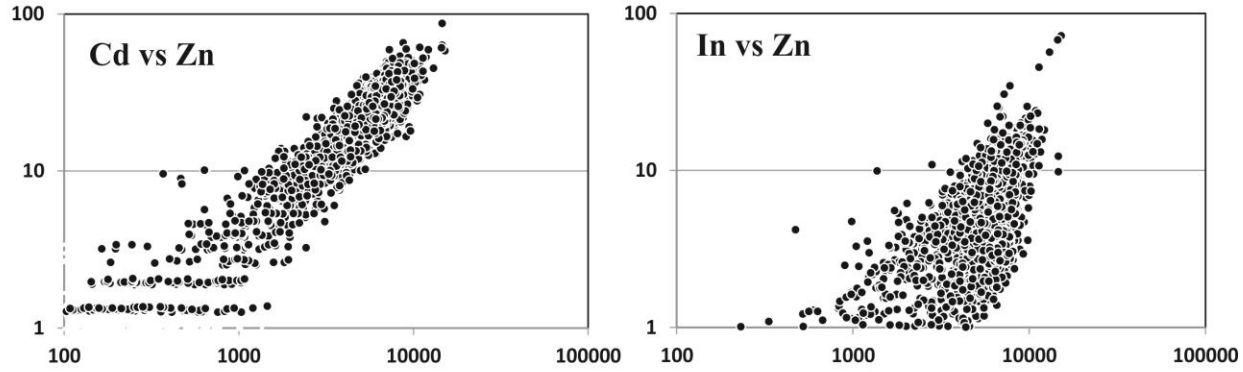

Group 3:

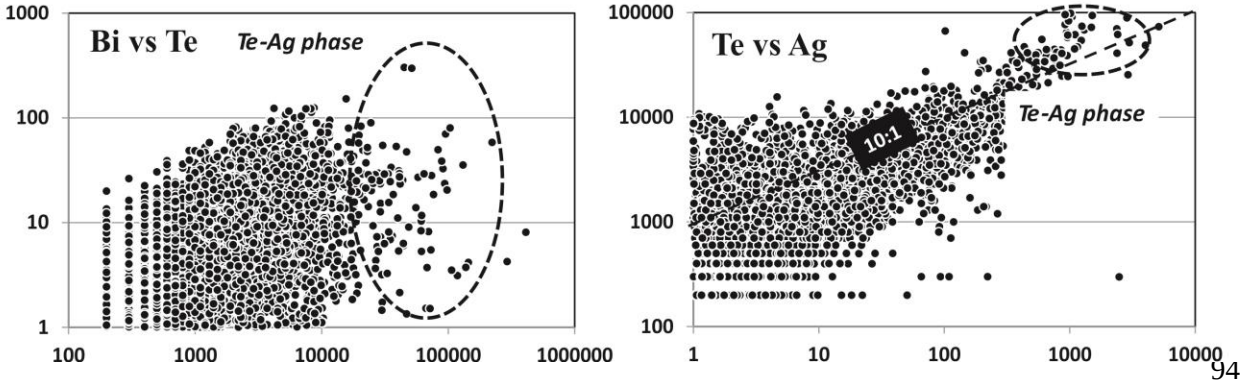

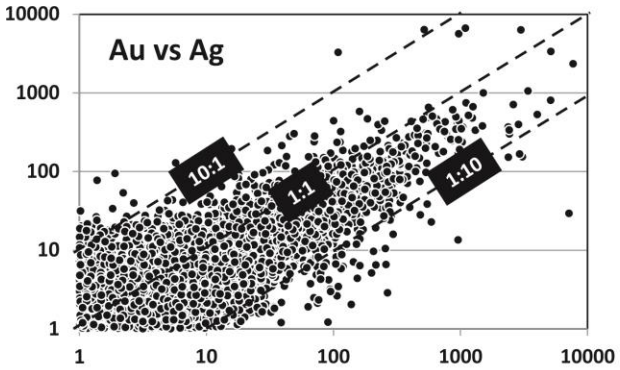
Au vs Ag
10:1
1:1
1:10
10000
1000
100
10
1
1
10
100
1000
10000

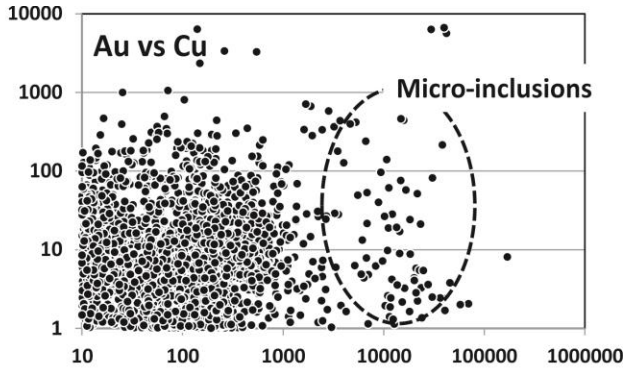
Au vs Cu
Micro-inclusions
10000
1000
100
10
1
10
100
1000
10000
100000
1000000

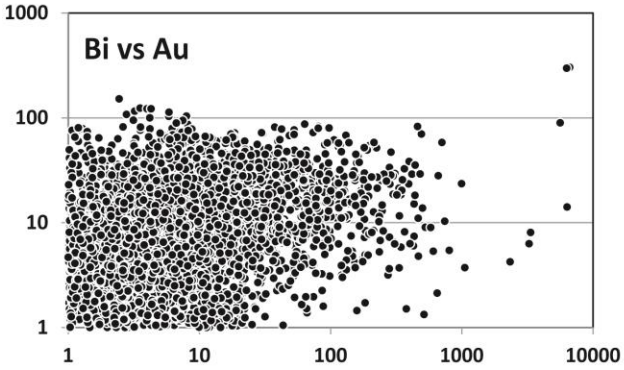
Bi vs Au
1000
100
10
1
1
10
100
1000
10000

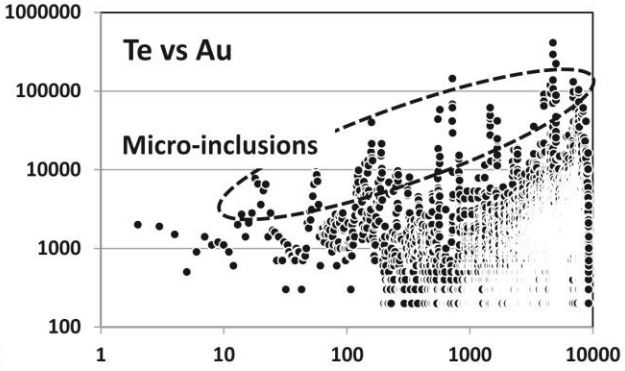
Te vs Au
Micro-inclusions
1000000
100000
10000
1000
100
1
10
100
1000
10000

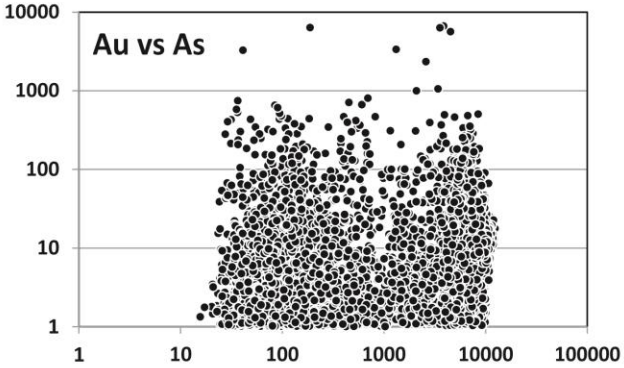
Au vs As
10000
1000
100
10
1
1
10
100
1000
10000
100000

Group 4:

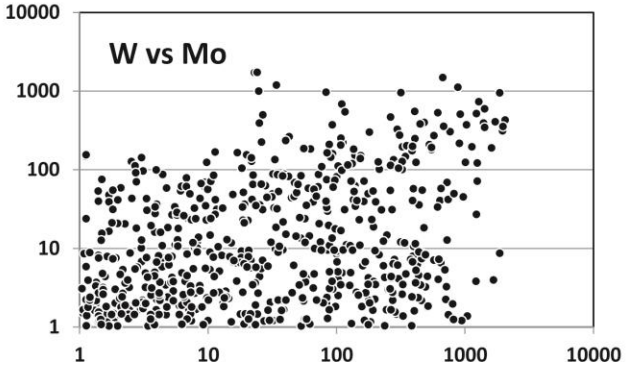
W vs Mo
10000
1000
100
10
1
1
10
100
1000
10000

Figure 21: Summary of binary element log-log plots for time series geochemical data produced using data from the elemental maps generated from LA ICP-MS analysis, as discussed in the text. Note that the data are presented in the same elemental associations and sequence as discussed in the text, thus groups 1 through 4. For the Au versus As plot the dashed line represents the saturation surface of gold in pyrite as a function of As content (from Reich et al. 2005).

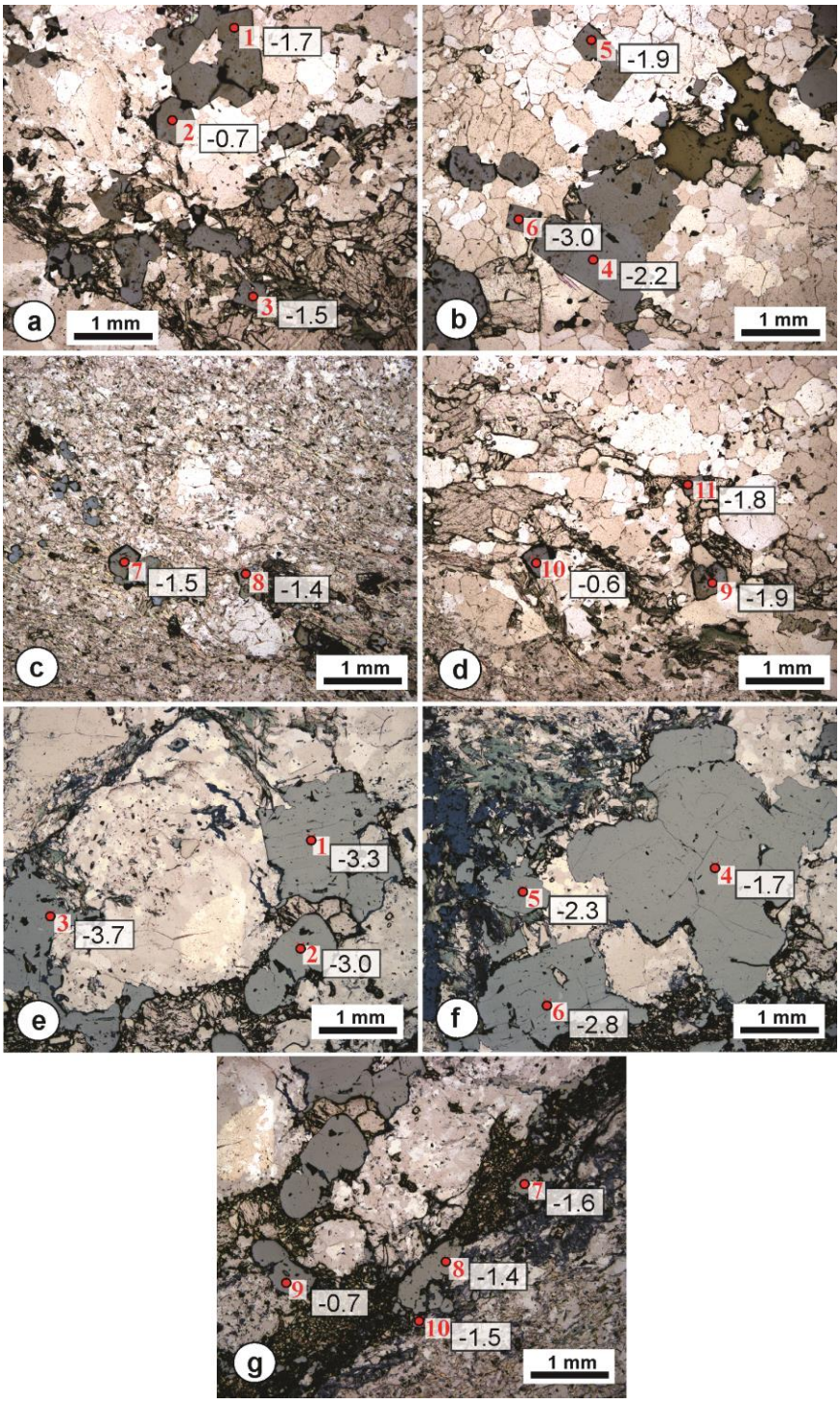

Figure 22: Spatial distribution of $\delta^{34}S$ values in pyrite grains hosted by an auriferous vein (JS13-29; a to d) and altered tonalite (JS13-20A; e to g) from the Candy Cane outcrop (combined transmitted and reflected light). Note the similarity of $\delta^{34}S$ values regardless of the host. Results are summarized in Table 3.

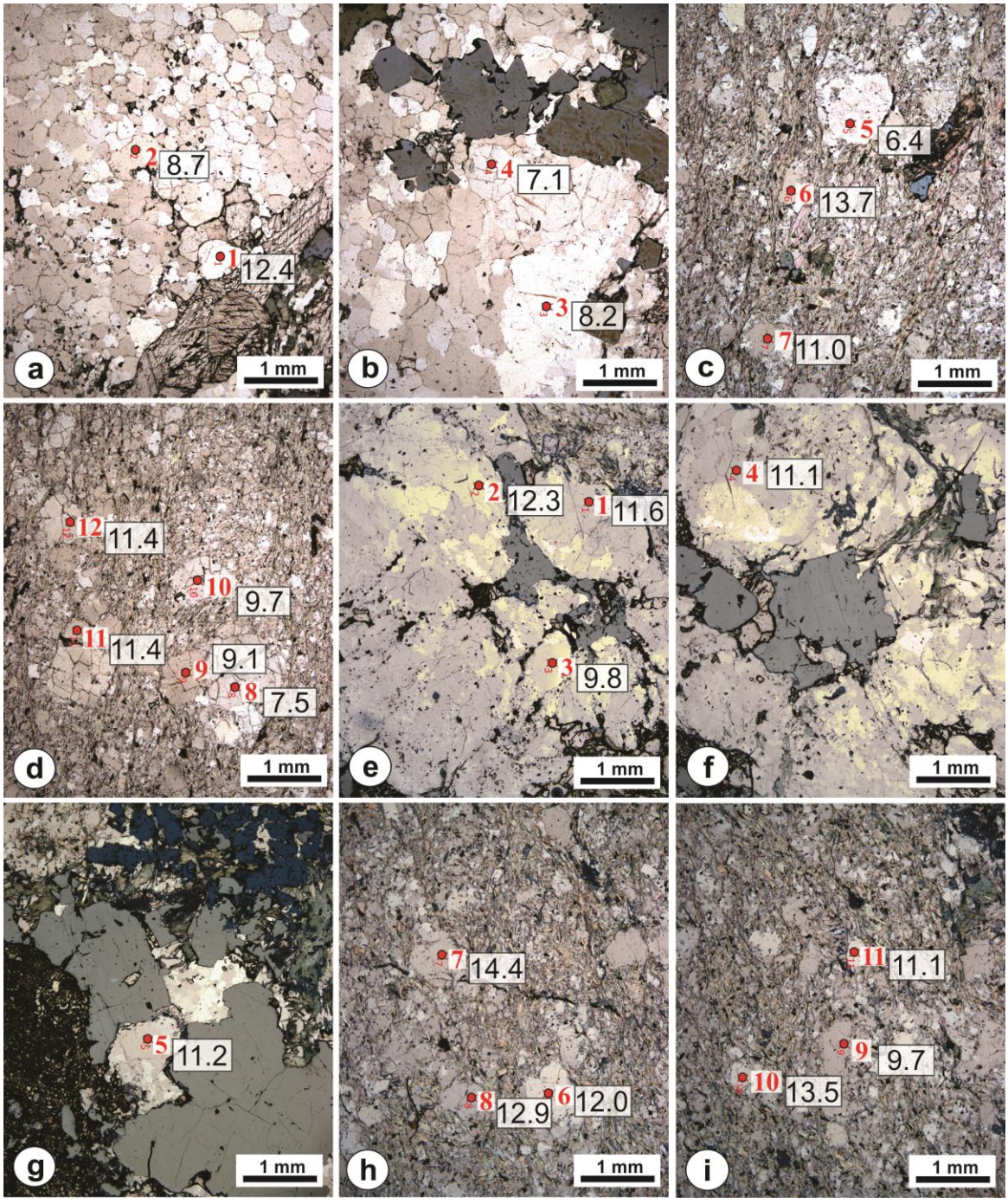

Figure 23: Spatial distribution of $\delta^{18}O$ values in quartz grains hosted by an auriferous vein (a, b, e, f, g) and its alteration halo in tonalite (c, d, h, i) from the Candy Cane outcrop (combined transmitted and reflected light). Analyzed samples are JS13-29 (a to d) and JS13-20A (e to i). Note the large range of data for rock-forming quartz within the alteration halo. Results of points 1-11 (JS13-29) and 1-10 (JS13-20A) are summarized in Table 3.

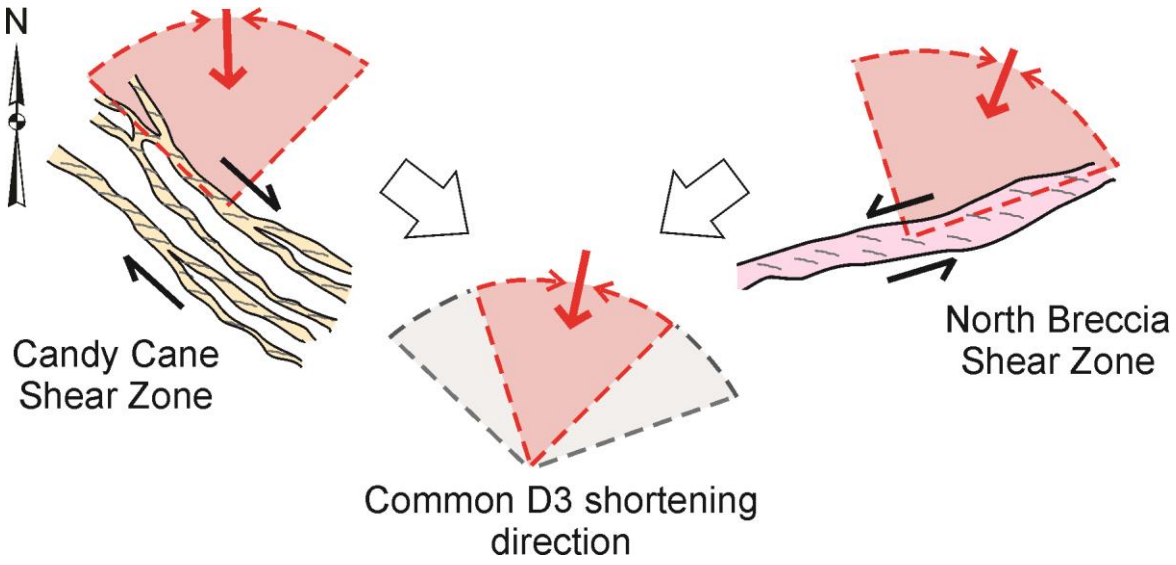

Figure 24: A diagram illustrating the similar shortening direction responsible for the movements at the Candy Cane (yellow) and North Breccia (pink) outcrops to form the observed shear zones. Associated foliations are shown with both dextral and sinistral shear as indicated. The red quadrants for each area represent the possible shortening directions necessary to facilitate the shear direction at each location. An overlap of both of these quadrants reveals a common D_3 shortening direction which is indicated by the pink area in the resolved diagram in the middle that would facilitate both movement directions (i.e., dextral and sinistral).

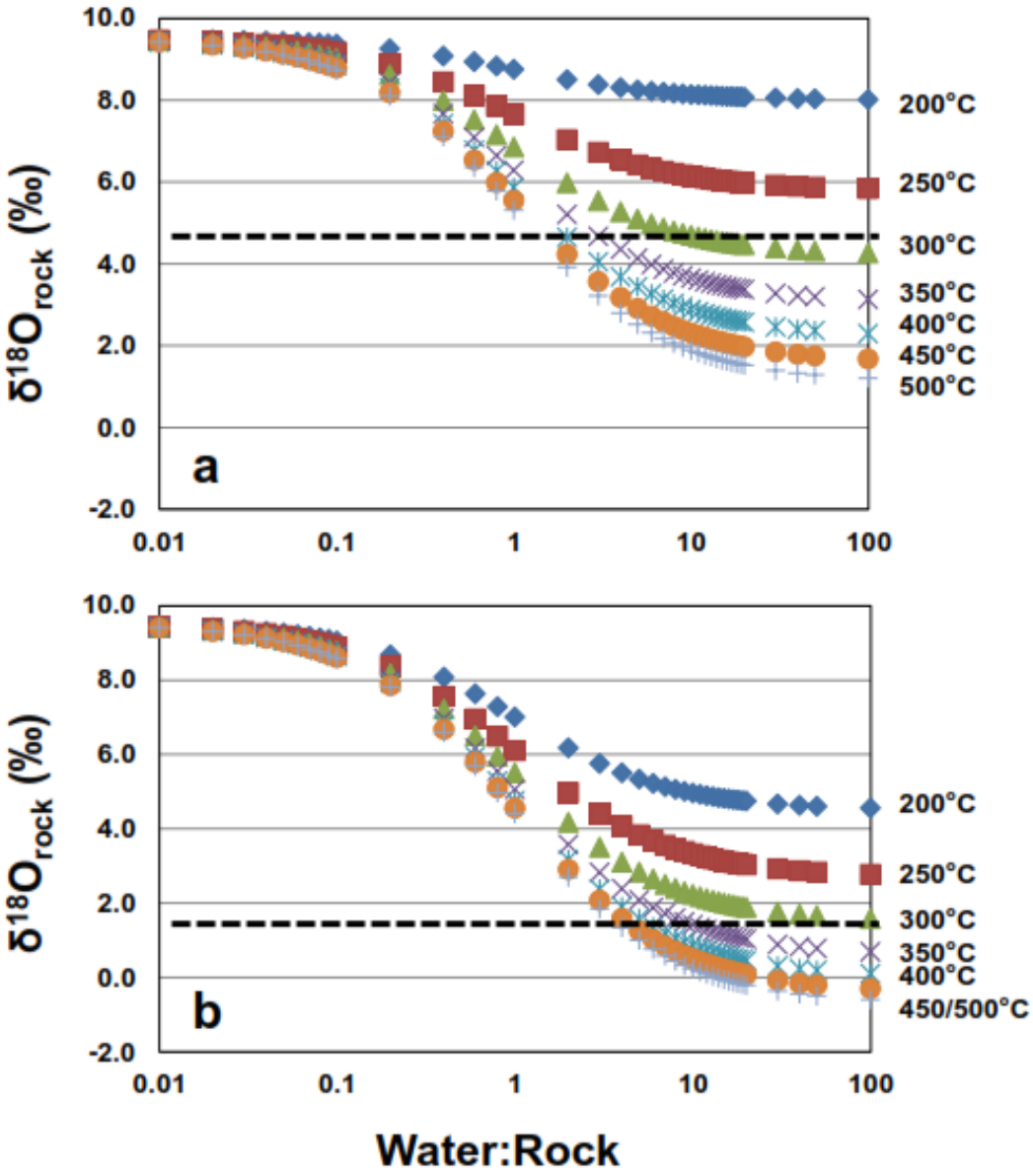

Figure 25: Results of water:rock ratio (W:R) calculations (see Taylor (1977) for details) for altered tonalite samples having an initial whole rock (using feldspar as a proxy) $\delta^{18}O$ value of+9.5‰ (see text for discussion) that interacts with a reacting fluid having $\delta^{18}O$= 0‰ (i.e., down-welling seawater) for temperatures ranging from 200° to 500°C. Note that the black dashed line in each plot represents the inferred $\delta^{18}O$ value for the altered rock. (a) Calculations done for a sample having quartz and plagioclase using feldspar-H_2O fractionation equation of Zheng (1993). (b) Calculations done for sample from the phllyic alteration, thus using muscovite as a proxy for the altered rock, with muscovite-H_2O fractionation equation of Zheng (1993). See text for further discussion and interpretation of the diagrams.

Table 1: A summary of the deformation events and related structures which have been recognized in the study area based on mapping.

Event	Structure	Description	Age
D_5	L_5	Late shallow crinkle lineation along S_2; defined by the grooves along the pre-existing foliation planes	
D_4	Shear zone	Transcurrent dextral reactivation of shear zones	
	S_4	Steeply-dipping, NE- striking cleavage	
	F_4	Z-shaped folds plunging ~80°E; millimeters to meters in amplitude	
D_3	Shear zone	Formation of new shear zones and reactivation of D2 shear zones during sinistral, south-side up shearing	
	L_3	Steeply-plunging mineral lineation along S3 defined by biotite and amphibole	
	S_3	Steeply-dipping, E-striking crenulation cleavage transposing S_2 along the Ridout deformation zone	
	F_3	Outcrop-scale, S-shaped folds striking 115° and plunging ~45°E	
D_2	Ridout deformation zone	Intensification of the foliation along the Ridout deformation zone and formation of shear zones with sinistral north-side up movement in the Chester intrusive complex	
	L_2	Steeply plunging stretching lineation defined by clasts 50°-76°N-NE	
	S_2	Steeply-dipping E-W oriented penetrative regional cleavage	
	F_2	Tight regional folds with kilometer–scale amplitudes	
D_1	S_1	Regional flattening foliation reported by Heather (2001)	<2680 Ma

Table 2: Summary of the Au assay results at the Candy Cane outcrop. Samples are grouped to examine the relationship between vein/alteration halo, host tonalite and deformation.

Sample Type	Au Range (g/t)	Average (g/t)	Standard Deviation
Channel sample - vein + halo	0.009 – 2.11	0.332	0.65
Channel sample - least altered tonalite	<0.001 – 0.049	0.019	0.021
Least deformed vein + halo	0.018 – 0.276	0.219	0.277
More deformed vein + halo	<0.005 – 0.063	0.029	0.027

Table 3:

Samples:	**CC-A**	**CC-B**	**CC-C**	**CC-D**	**CC-E**	**CC-F**
SiO_2	69.99	67.75	69.3	69.31	69.13	69.99
Al_2O_3	14.4	15.19	14.89	14.79	15.29	15.45
FeO	2.6	3.5	2.7	2.9	2.5	2.2
Fe_2O_3	2.02	1.69	0.86	0.83	0.76	1.08
MnO	0.015	0.024	0.023	0.026	0.03	0.022
MgO	0.64	0.87	0.77	0.81	0.76	0.69
CaO	0.68	1.28	2.57	2.46	3.26	3.53
Na_2O	0.39	3.31	4.64	4.34	4.18	4.61
K_2O	4.12	1.81	0.66	0.94	0.98	0.58
TiO_2	0.311	0.332	0.304	0.311	0.309	0.308
P_2O_5	0.08	0.11	0.11	0.09	0.09	0.09
CO_2	0.07	0.14	0.13	0.22	0.85	0.26
LOI	2.85	1.77	1.01	1.24	1.78	1.09
SO_2	1.379	0.32	<0.01	0.08	0.04	<0.01
F	0.1	0.04	0.02	0.01	0.01	<0.01
Total	98.39	98.04	98.14	98.35	99.36	99.9
Au	12	2	1	41	348	21

Co	6.2	2.2	3.6	2.9	2.2	4.9
Ni	5	6	9	9	8	7
Cu	220	88.2	13.6	36.5	13.2	7.3
Sn	14	8	6	7	4	6
Li	42	22	10	15	15	9
Sc	5	5	5	5	5	4
Be	<1	1	1	1	1	1
V	36	33	32	31	27	23
Rb	189	88	33	48	49	31
Ga	21	18	18	18	18	19
Ge	1	1.3	1.1	1.2	1.1	1.1
As	<5	<5	<5	<5	<5	<5
Y	15.2	16.2	19.7	20.5	16.8	20.3
Zr	145	140	140	147	141	143
Nb	5.6	6.2	5.3	6.2	4.9	5.9
Mo	<1	<1	1	1	1	2
Cs	2.7	1.3	0.6	0.8	0.7	0.5
Ba	403	206	97	124	132	135
Sr	51	105	178	165	183	215
La	12.8	6.85	20.4	11.1	7.19	7.69
Ce	21.9	14.3	40.1	24.1	16.2	14.9
Pr	2.47	1.83	4.63	3.07	2.32	1.95

Nd	9.93	7.97	18.1	13.5	10.5	9
Sm	2.37	2.35	3.84	3.68	3.07	2.95
Eu	0.454	0.557	0.806	0.81	0.67	0.775
Gd	2.23	2.44	3.55	3.7	3.07	3.44
Tb	0.38	0.43	0.58	0.59	0.5	0.57
Dy	2.43	2.73	3.49	3.6	3.02	3.52
Ho	0.5	0.55	0.7	0.71	0.6	0.69
Er	1.55	1.7	2.01	2.05	1.78	2.05
Tm	0.232	0.27	0.291	0.296	0.274	0.302
Yb	1.56	1.7	1.87	1.93	1.76	1.88
Lu	0.239	0.248	0.278	0.283	0.26	0.278
Hf	4.4	4.3	4.4	4.7	4.3	4.2
Ta	0.43	0.42	0.45	0.33	0.38	0.39
W	5.6	2.3	3.1	12.6	2.5	1
Tl	0.3	0.14	<0.05	<0.05	<0.05	<0.05
Pb	<5	<5	<5	<5	<5	<5
Th	1.8	2.13	2.54	1.99	2.35	1.95
U	0.63	0.8	0.71	0.71	0.83	0.82
As	3.7	1.9	2.1	1.8	1.8	2.9
Bi	0.37	0.21	0.21	0.22	0.17	0.12
Sb	0.15	0.13	0.19	0.18	0.2	0.24
Se	1	0.4	0.3	0.7	0.5	0.6
Te	<0.02	<0.02	<0.02	<0.02	0.18	0.05
Ag	<1	<1	<1	<1	<1	<1

Cd	<0.2	<0.2	<0.2	<0.2	<0.2	<0.2
Cr	17	17	19	29	19	24
In	<0.2	<0.2	<0.2	<0.2	<0.2	<0.2
Ni	5	6	9	9	8	7
Mn	120	188	218	257	240	172
Pb	<2	<2	2	3	2	3
Zn	7.6	18	18.4	21.8	18	16.8

*clustered data points are demonstrated visually by spaces within the table

All major oxides and volatiles (LOI, SO_2, F) are in weight %. Trace elements are in ppm.

Elements below the detection limit were retested through total digestion ICP-MS to limits in ppm of 0.02 for Bi, 0.1 for As, 0.2 for In, 0.5 for Co and Cu, 1 for Ag, Cr, Ni and Mo, and 2 for Pb.

Table 4:

Sample	Location Type	Point	$\delta^{34}S$	1σ(‰)
CL11-JS13-29	Vein	1	-0.7	0.3
	Vein	2	-1.7	0.3
	Vein	3	-1.5	0.3
	Vein	4	-2.2	0.3
	Vein	5	-1.9	0.3
	Vein	6	-3.0	0.3
	Tonalite	7	-1.5	0.3
	Tonalite	8	-1.4	0.3
	Vein	9	-1.9	0.3
	Vein	10	-0.6	0.3
	Vein	11	-1.8	0.3
CL11-JS13-20A	Vein	1	-3.3	0.3
	Vein	2	-3.0	0.3
	Vein	3	-3.7	0.3
	Vein	4	-1.7	0.3
	Vein	5	-2.3	0.3
	Vein	6	-2.8	0.3
	Tonalite	7	-1.6	0.3
	Tonalite	8	-1.4	0.3
	Vein	9	-1.5	0.3
	Tonalite	10	-1.5	0.3

Sample	Location Type	Point	$\delta^{18}O$	1σ(‰)	$\delta^{18}O$@300°C	$\delta^{18}O$@400°C
CL11-JS13-29	Vein	1	12.4	1.2	6.4	8.4
	Vein	2	8.7	1.2	2.7	4.7
	Vein	3	8.2	1.2	2.2	4.2
	Vein	4	7.1	1.2	1.1	3.1
	Tonalite	5	6.4	1.2	0.4	2.4
	Tonalite	6	13.7	1.2	7.7	9.7
	Tonalite	7	11.0	1.2	6.0	7.0

	Tonalite	8	7.5	1.2	1.5	3.5
	Tonalite	9	9.1	1.2	3.1	5.1
	Tonalite	10	9.9	1.2	3.9	5.9
	Tonalite	11	11.4	1.2	5.4	7.4
	Tonalite	12	11.4	1.2	5.4	7.4
	Vein	1	11.6	1.2	5.6	7.6
CL11-JS13-20A	Vein	2	12.3	1.2	6.3	8.3
	Vein	3	9.8	1.2	3.8	5.8
	Vein	4	11.1	1.2	5.1	7.1
	Vein	5	11.2	1.2	5.2	7.2
	Tonalite	6	12.0	1.2	6.0	8.0
	Tonalite	7	14.4	1.2	8.4	10.4
	Tonalite	8	12.9	1.2	6.9	8.9
	Tonalite	9	9.7	1.2	3.7	5.7
	Tonalite	10	13.5	1.2	7.5	9.5
	Tonalite	11	11.1	1.2	5.1	7.1

Locations of point analysis for $\delta^{34}S$ and $\delta^{18}O$ are shown in Figures 21 and 22. Calculations were made using fractionation curves from Taylor (1979).

Appendices

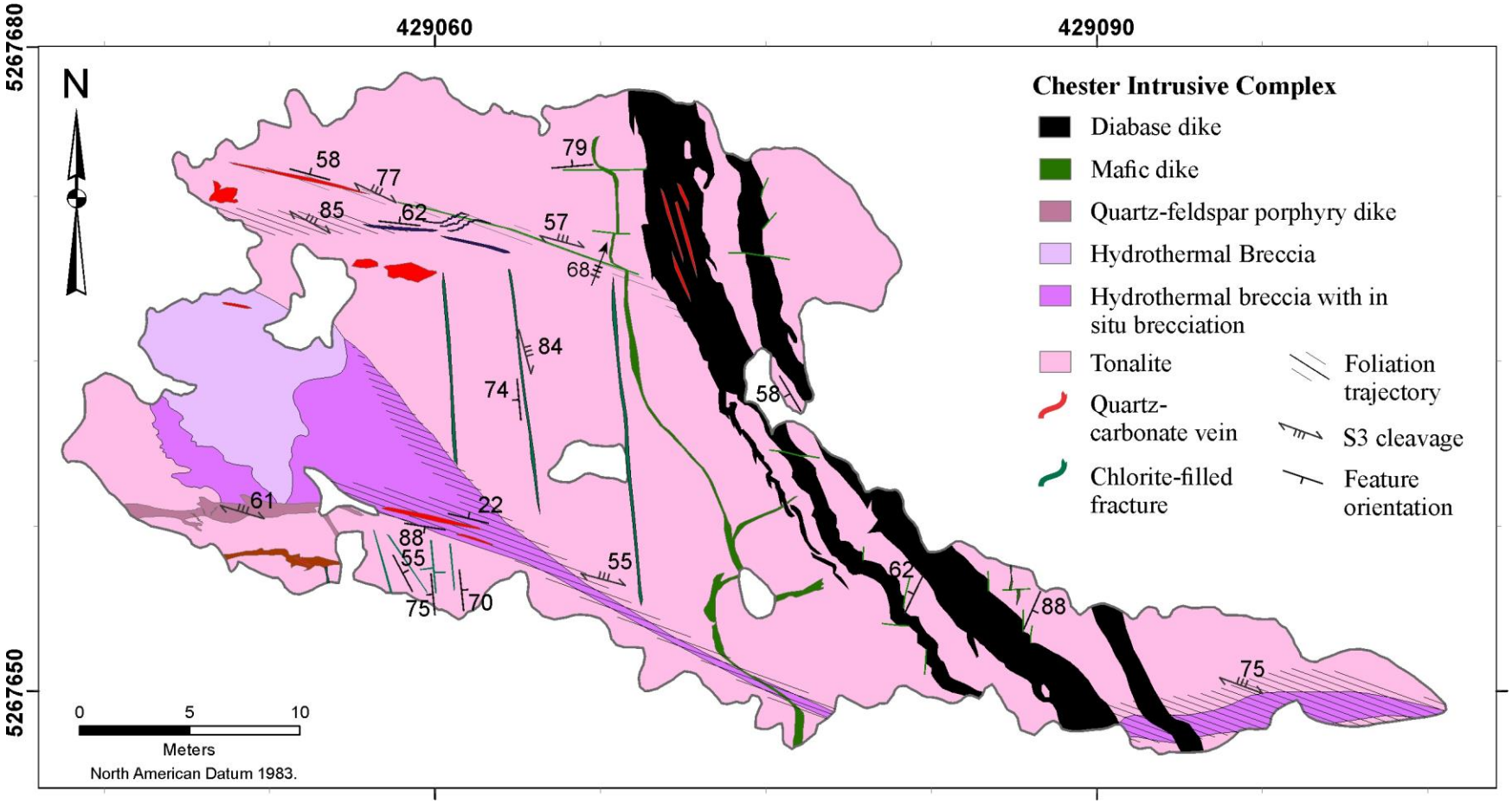

Appendix A. 1: Simplified geology map of the Whale outcrop.

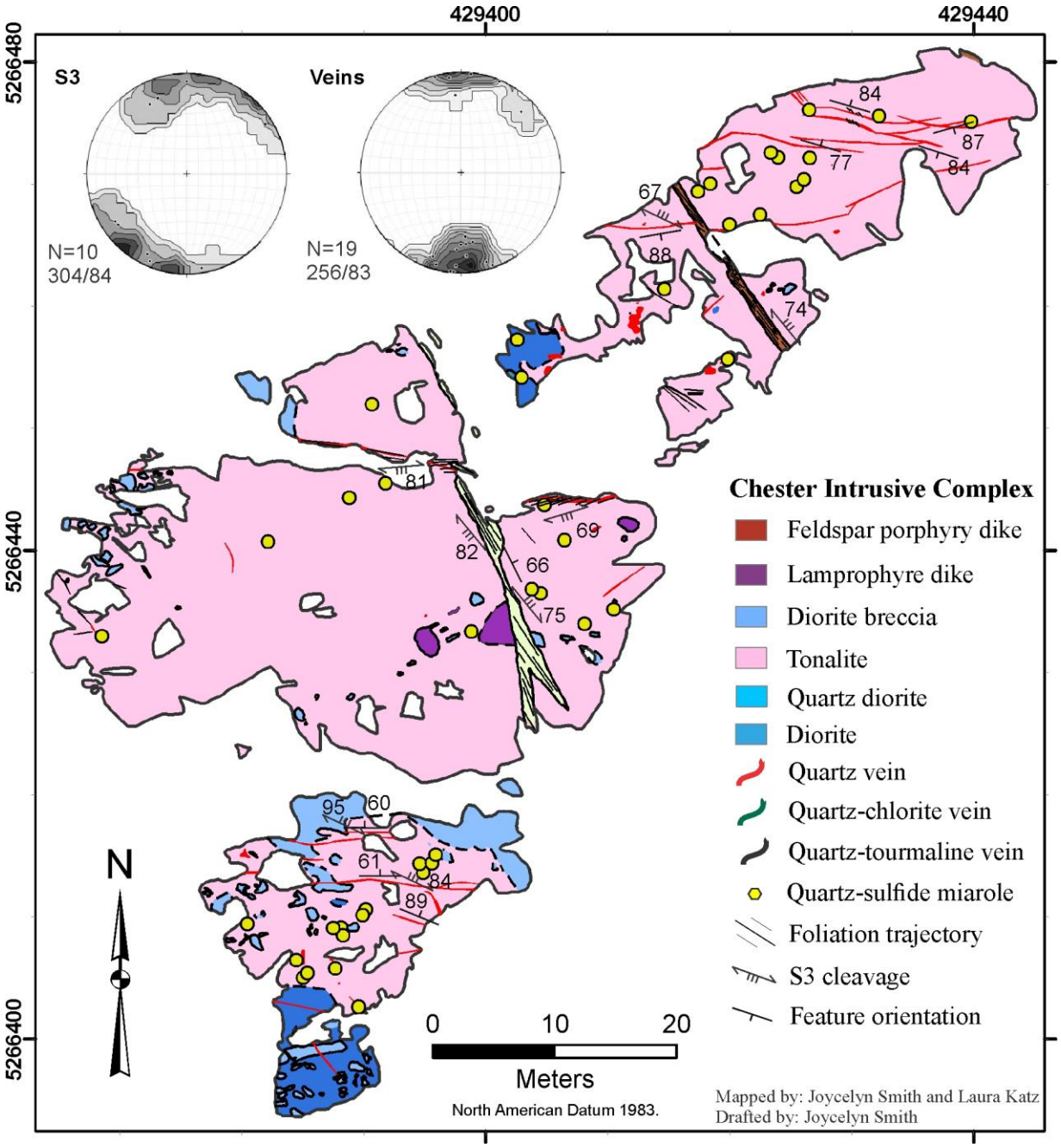

Appendix A. 2: Simplified geology map of the outcrop 53. Equal area, lower hemisphere projections show the orientaions of S_2 and the mineralized E-W trending veins present (shown in red) with number of measurements (N) and contours in multiples of 2.

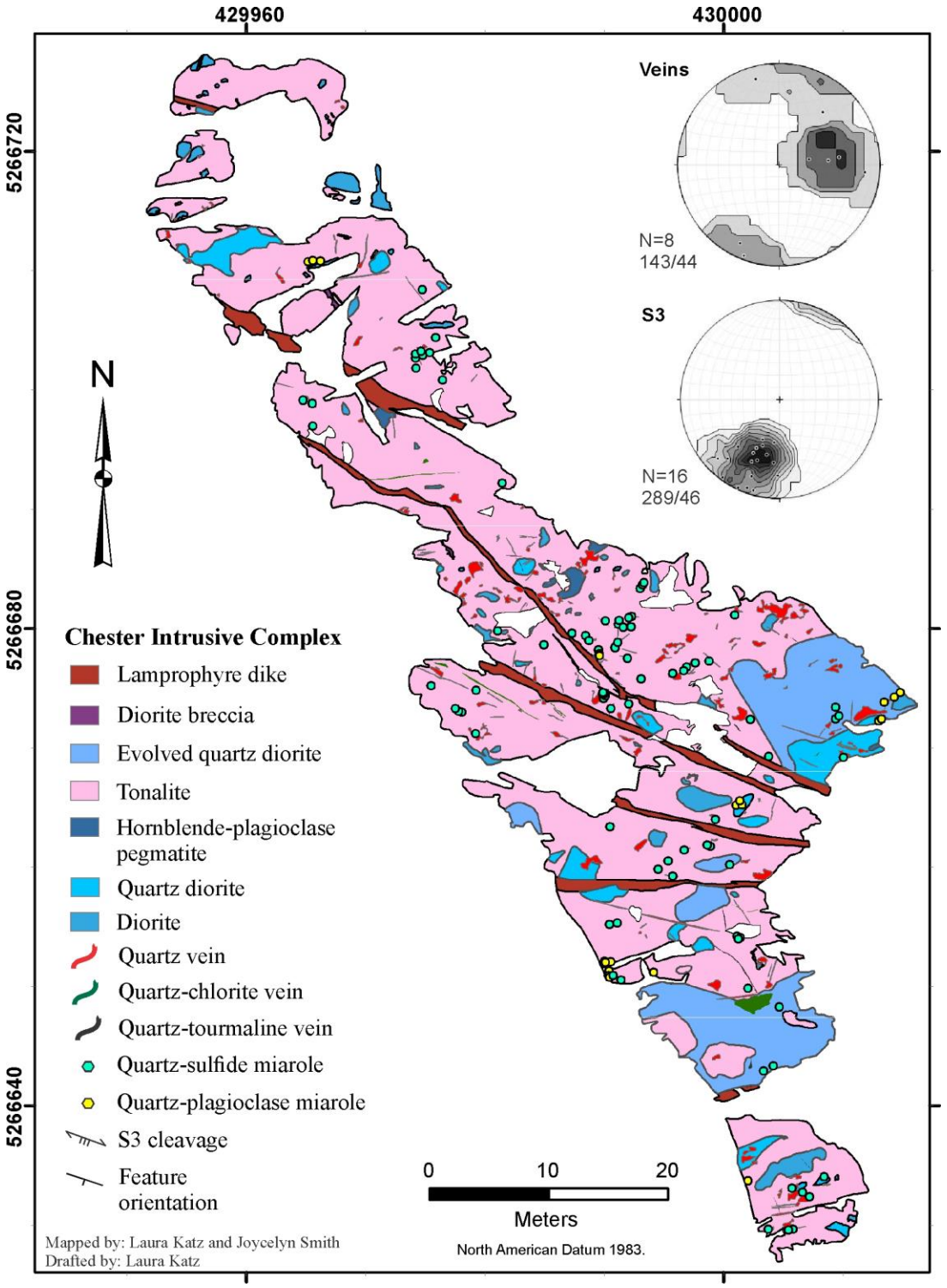

Appendix A. 3: Simplified geology map of the Skidder outcrop. Equal area, lower hemisphere projections show the orientaions of S_3 and the mineralized E-W trending veins present with number of measurements (N) and contours in multiples of 2.

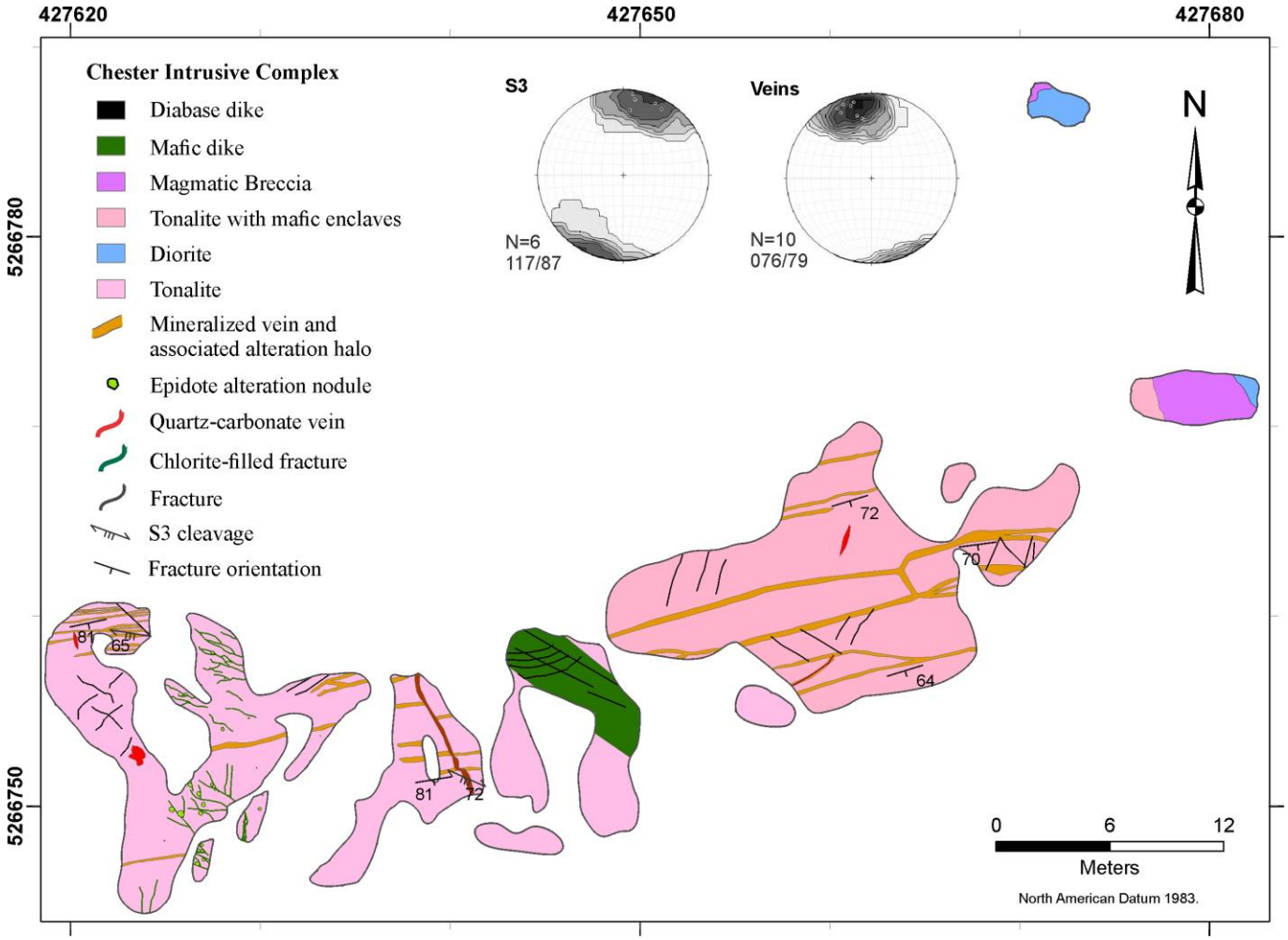

Appendix A. 4: Simplified geology map of the Clam A outcrop. Equal area, lower hemisphere projections show the orientaions of S_3 and the mineralized E-W trending veins present with number of measurements (N) and contours in multiples of 2.

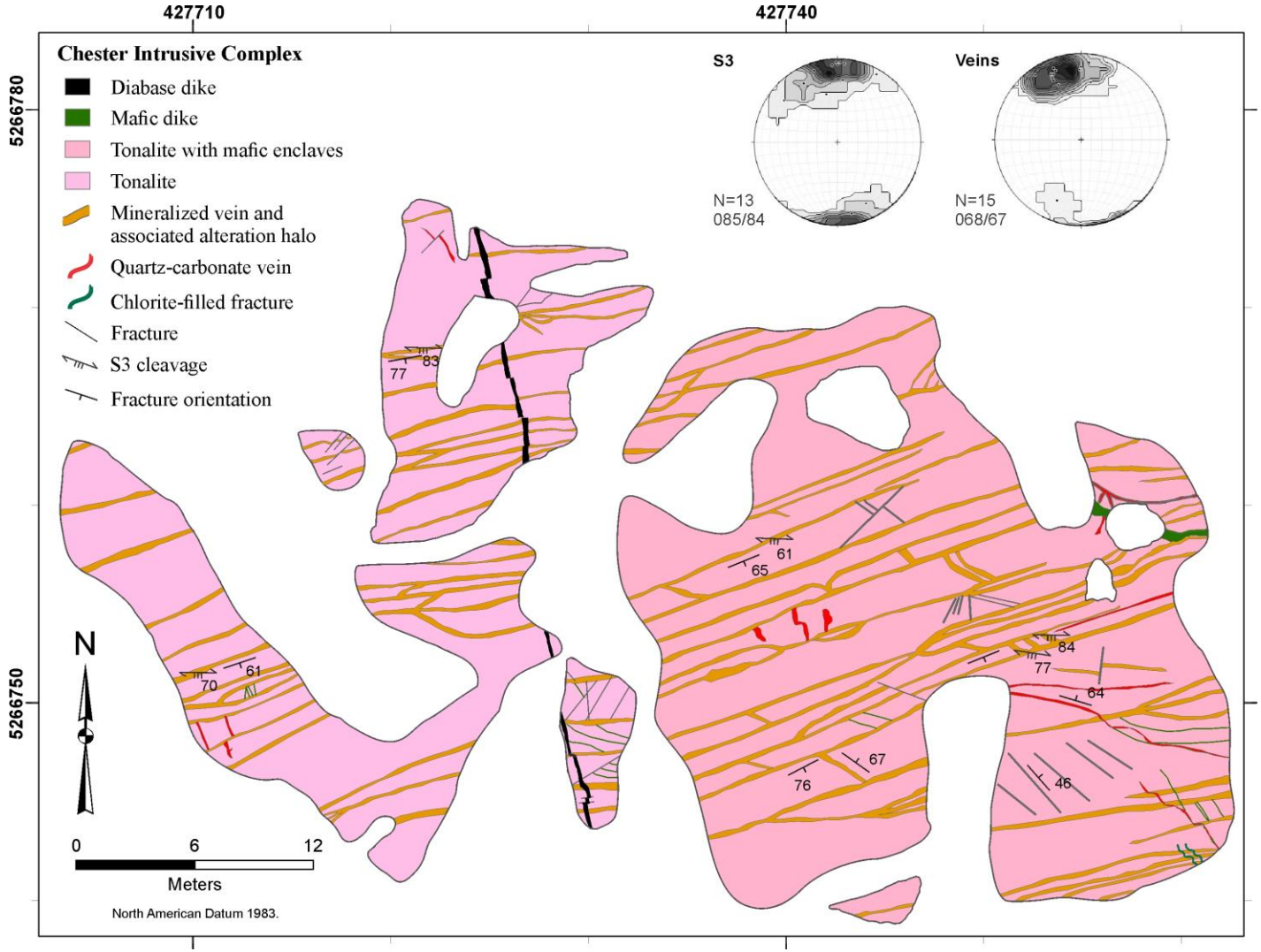

Appendix A. 5: Simplified geology map of the Clam B outcrop. Equal area, lower hemisphere projections show the orientaions of S_3 and the mineralized E-W trending veins present with number of measurements (N) and contours in multiples of 2.

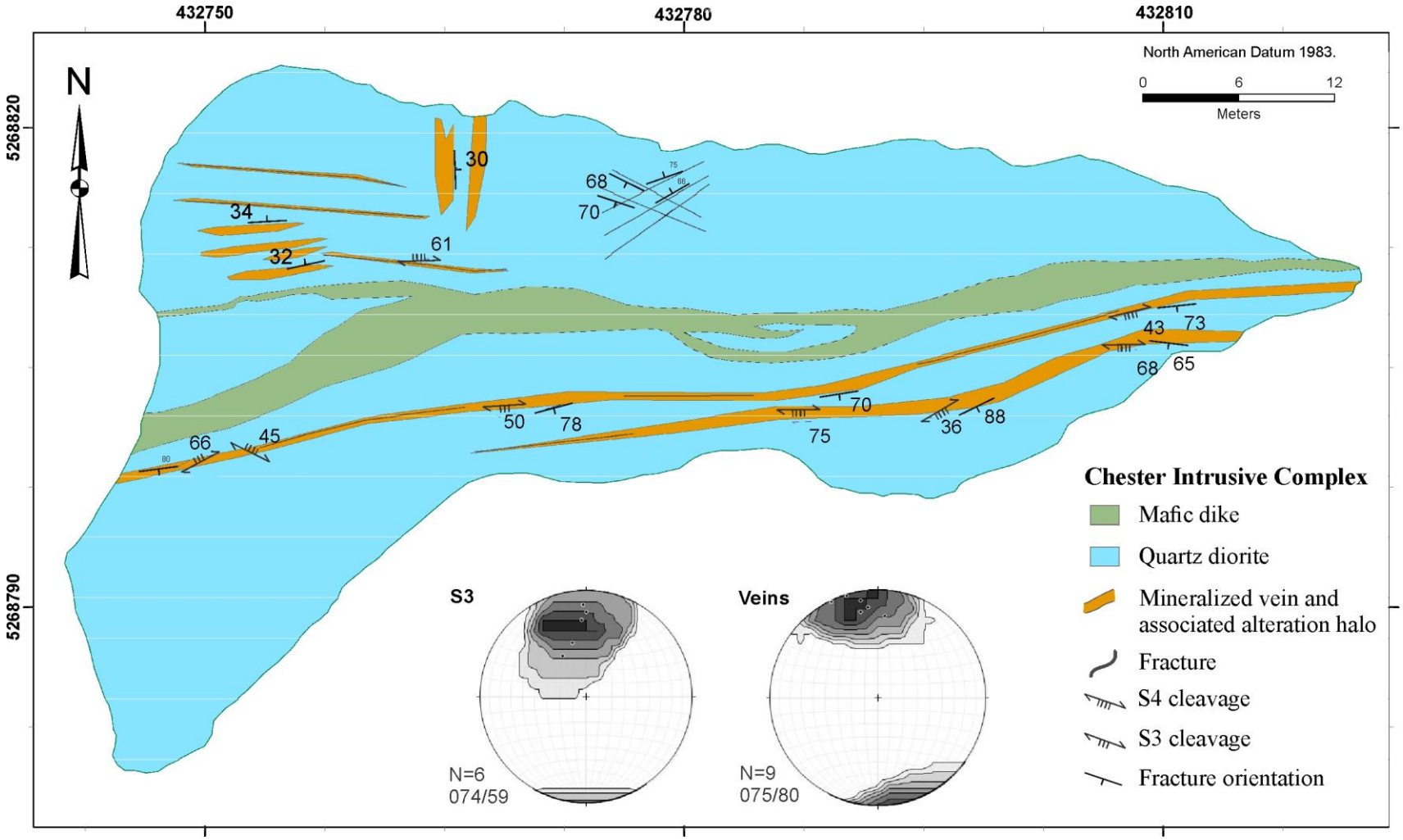

Appendix A. 6: Simplified geology map of the Jack Rabbit A outcrop. Equal area, lower hemisphere projections show the orientaions of S_3 and the mineralized E-W trending veins present with number of measurements (N) and contours in multiples of 2.

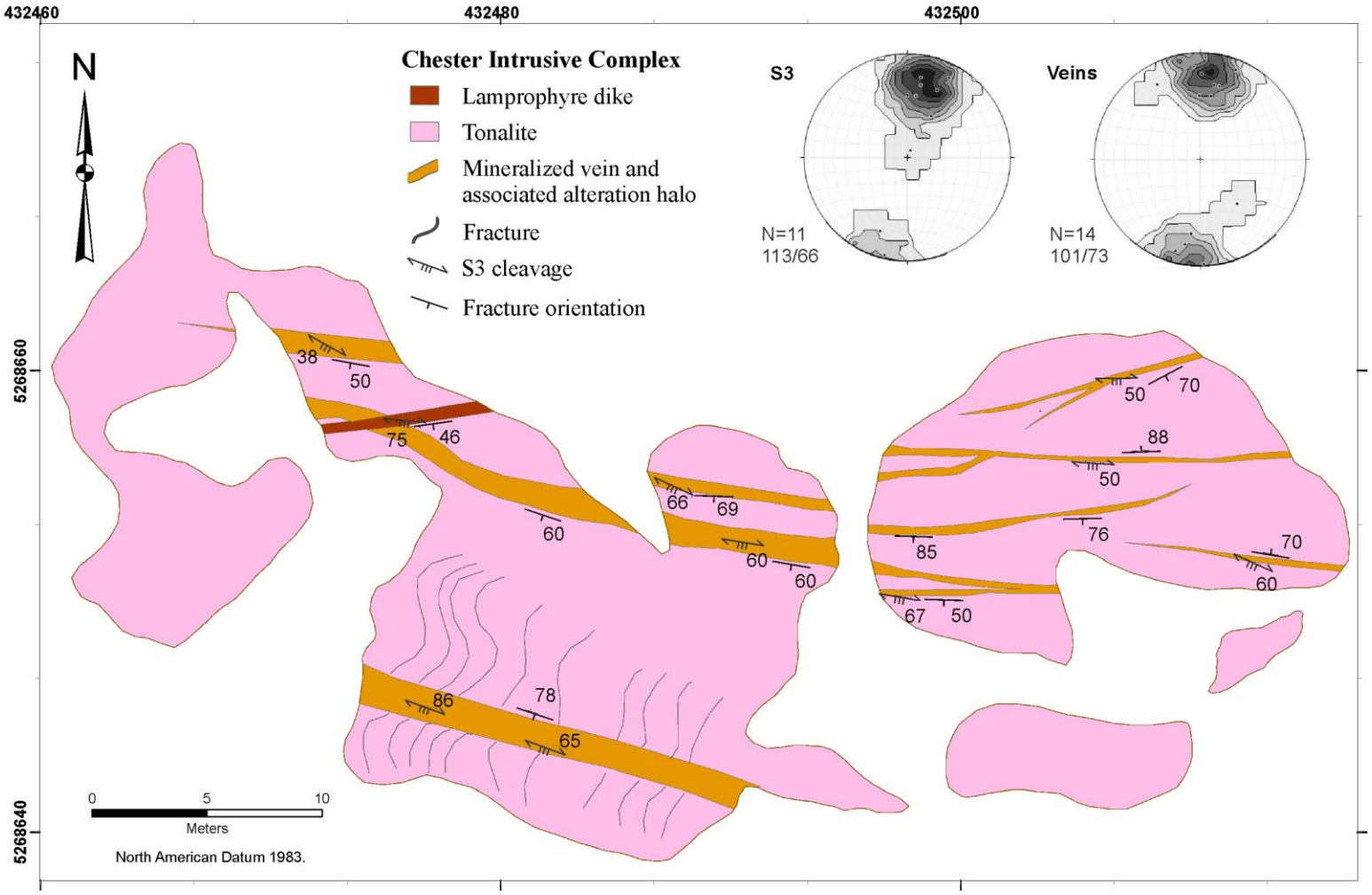

Appendix A. 7: Simplified geology map of the Jack Rabbit B outcrop. Equal area, lower hemisphere projections show the orientaions of S_3 and the mineralized E-W trending veins present with number of measurements (N) and contours in multiples of 2.